Synthesis of Amine Modified Metal Organic Frameworks for Carbon Dioxide Capture

By

Muhammad Munib Ul Hassan

(Registration No: 00000362045)

School of Chemical and Materials Engineering

National University of Sciences & Technology (NUST)

Islamabad, Pakistan

(2024)

Synthesis of Amine Modified Metal Organic Frameworks for Carbon Dioxide Capture

By

Name: Muhammad Munib Ul Hassan

(Registration No: 00000362045)

A thesis submitted to the National University of Sciences and Technology, Islamabad,

in partial fulfillment of the requirements for the degree of

Master of Science in Chemical Engineering

Supervisor Name: Dr. Tayyaba Noor

School of Chemical and Materials Engineering

National University of Sciences and Technology (NUST)

Islamabad, Pakistan

(2024)

THESIS ACCEPTANCE CERTIFICATE

Certified that final copy of MS Thesis written by Mr **Muhammad Munib Ul Hassan** (Registration No 00000362045), of School of Chemical & Materials Engineering (SCME) has been vetted by undersigned, found complete in all respects as per NUST Statues/Regulations, is free of plagiarism, errors, and mistakes and is accepted as partial fulfillment for award of MS degree. It is further certified that necessary amendments as pointed out by GEC members of the scholar have also been incorporated in the said Thesis.

Signature: _____

Name of Supervisor: **Dr Tayyaba Noor**

Date: _____ 03/07/2024

Signature (HOD): _____

Date: _____ 3/7/24

Dr Erum Pervaiz
Professor
SCME, NUST, H-12. Islamabad

Signature (Dean/Principal): _____

Date: _____ 4/7/24

National University of Sciences &Technology (NUST)

MASTER'S THESIS WORK

We hereby recommend that the dissertation prepared under our supervision by

Regn No & Name: 00000362045 Muhammad Munib Ul Hassan

Title: Synthesis of Amine Modified Metal Organic Frameworks for Carbon Dioxide Capture.

Presented on: 27 Jun 2024   at: 1430 hrs in SCME Seminar Hall

Be accepted in partial fulfillment of the requirements for the award of Master of Science degree in **Chemical Engineering**.

Guidance & Examination Committee Members

Name: **Dr Ameen Shahid**   Signature: _____

Name: **Dr Erum Pervaiz**   Signature: _____

Supervisor's Name: **Dr Tayyaba Noor**   Signature: _____

                                             Dated: 27/06/2024

Head of Department

Date 27/6/24

Dean/Principal

Date 28/6/24

School of Chemical &Materials Engineering (SCME)

AUTHOR'S DECLARATION

I <u>Muhammad Munib ul Hassan</u> hereby state that my MS thesis titled " **Synthesis of Amine Modified Metal Organic Frameworks for Carbon Dioxide Capture** " is my own work and has not been submitted previously by me for taking any degree from National University of Sciences and Technology, Islamabad or anywhere else in the country/ world.

At any time if my statement is found to be incorrect even after I graduate, the university has the right to withdraw my MS degree.

Name of Student: <u>Muhammad Munib ul Hassan</u>
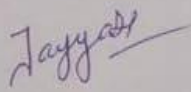
Date: <u>9/7/2024</u>

Certificate for Plagiarism

It is certified that MS Thesis Titled "**Synthesis of Amine Modified Metal Organic Frameworks for Carbon Dioxide Capture**", by Regn No 00000362045 Muhammad Munib Ul Hassan has been examined by us. We undertake the follows:-

a.   Thesis has significant new work/knowledge as compared already published or are under consideration to be published elsewhere. No sentence, equation, diagram, table, paragraph or section has been copied verbatim from previous work unless it is placed under quotation marks and duly referenced.

b.   The work presented is original and own work of the author (i.e. there is no plagiarism). No ideas, processes, results, or words of others have been presented as author own work.

c.   There is no fabrication of data or result which has been compiled/analyzed.

d.   There is no falsification by manipulating research materials, equipment, or processes, or changing or omitting data or result such that the research is not accurately represented in the research record.

e.   The thesis have been checked using TURNITIN (copy of originally report attached) and found within limits as pre HEC Plagiarism Policy and instructions issued from time to time.

MS Thesis Supervisor
(Dr Tayyaba Noor)
02 July 2024

Dr Tayyaba Noor
Associate Professor
SCME NUST H-12 Islamabad

DEDICATION

Dedicated to Almighty Allah, my beloved family, and my supervisor. It could not have been possible without them.

ACKNOWLEDGEMENTS

TABLE OF CONTENTS

LIST OF FIGURES

LIST OF TABLES

LIST OF SYMBOLS, ABBREVIATIONS AND ACRONYMS

GHG	Greenhouse gas
CCS	Carbon capture and storage
CO_2	Carbon dioxide
DI	Deionized Water
SEM	Scanning electron microscopy
XRD	X-ray Diffraction
EDX	Energy Dispersive X-ray
PSA	Particle Size Analyzer
BET	Brunauer-Emmett-Teller
FTIR	Fourier Transform Infrared Spectroscopy
HCM	Hierarchical carbon monoliths
Ads/Des	Adsorption/Desorption
Cu	Copper
Cu-BTC	Copper BTC MOF
DPA	Diphenylamine
Mel	Melamine
HMTA	Hexamethylenetetramine
Wt%	Weight percentage
HKUST-1	Copper MOF
DMF	N, N-dimethylformamide
AC	Activated Carbon
IFMC	Institute of Functional Material Chemistry

ABSTRACT

The major energy needs are met by burning fossil fuels, which are among the most common fuel resources in the world. Global climate change is largely caused by energy resources like these that have high CO_2 emissions. To decrease the amount of CO_2 in the atmosphere, some concrete actions are needed. A method for reducing climate change and global warming is carbon capture and storage, which has shown some encouraging results. The process's most crucial component is carbon capture. Solid adsorbents have found widespread application in gas separation. In carbon capture, nonporous inorganic materials known as metal organic frameworks are used as adsorbents. This thesis focuses on the production, characterization, and adsorption and desorption studies of Copper MOF and its amine modifications using melamine, diphenylamine and hexamethylenetetramine (HMTA). MOFs offer broad surface area, particular pore sizes, affordability, and molecular sieving capability make them suitable for a variety of uses.

A high-pressure sorption analyzer was used to examine the CO_2 adsorption of MOF samples and desorption activities. SEM analysis was also used to examine the samples' surface features and morphology, and X-ray diffraction was used to determine the samples' crystallinity. FTIR spectroscopy was used to confirm the presence of various functional groups. The adsorption and desorption of these materials were examined at 50°C and 0–15 bar of pressure.

The Cu-BTC showed a high adsorption capacity of 1.980 mmol/g. But its amine modification using diphenylamine gave the highest adsorption capacity. The introduction of amines in the MOF introduces a basic site to structure which increases the chemical interaction and selectivity of adsorption of carbon dioxide. The DPA modified copper MOF had an adsorption capacity of 2.518mmol/g at a pressure of 15bar. Although the adsorption capacity of the other two amine modified MOFs was lower. The adsorption on Melamine and HMTA modified MOF was 1.195 and 1.032 mmol/g, respectively.

Keywords. Carbon Dioxide adsorption study, Greenhouse effect, Carbon emissions, Metal-organic framework, Copper metal organic framework, Cu-BTC, amine modified metal organic framework.

CHAPTER 1   INTRODUCTION

1.1   Background

CO_2 is a greenhouse gas that can warm up an area, rising CO_2 levels in the environment pose a serious threat to global climate change [1] . It has long been believed that CO_2 is the primary contributor to global climate change and the most major greenhouse gas (GHG) produced by humans. Consequently, the creation of a sustainable carbon capture and seizure system (CCS) is a significant scientific endeavor [2]. Due in large part to the fast industrialization and extensive use of fossil fuels, the concentration of carbon dioxide reached 415.88 parts per million in February of 2021. Fossil fuel energy facilities are significant contributors to global warming because their CO_2 emissions make up around 30% of overall emissions [3]. From a pre-industrialized level of about 280 parts per million, its atmospheric concentration increased to 384 parts per million in 2007 and is predicted to reach 550 parts per million by 2050, even if CO_2 emissions stay constant for the next forty years [4]. One of the ecological effects of CO_2 buildup in the atmosphere is global warming. In fact, compared to the years 1906–2005, the 50 years from 1956 to 2005 have seen a roughly twofold increase in a linear warming trend. Among the most important issues facing the twenty-first century are those related to the environment and energy. More than 80% of our energy comes from burning fossil fuels, and this will be the main source of energy for many years to come. It is commonly accepted that carbon dioxide, which is produced during burning, is the primary greenhouse gas released by humans that contributes to global warming [5].

1.2   Carbon Dioxide as a Greenhouse Gas

The amount of carbon dioxide and other greenhouse gases in the environment has increased significantly since the industrial revolution. The main contributor of greenhouse gases released into the atmosphere is CO_2. Since 1989, as public awareness of the effects of climate change has grown, researchers have been interested in lowering greenhouse gas emissions from CO_2. Globally, sequestering carbon dioxide is becoming more and more significant. In Kyoto, several nations signed the United Nations Framework Treaty on Climate Change (UNFCCC), pledging to cut

CO_2 emissions by 6% below 1990 levels. Protection of the climate system must be carried out "on an equitable basis and in agreement with Parties' common but differentiated obligations and various capabilities," according to a UNFCCC statement.
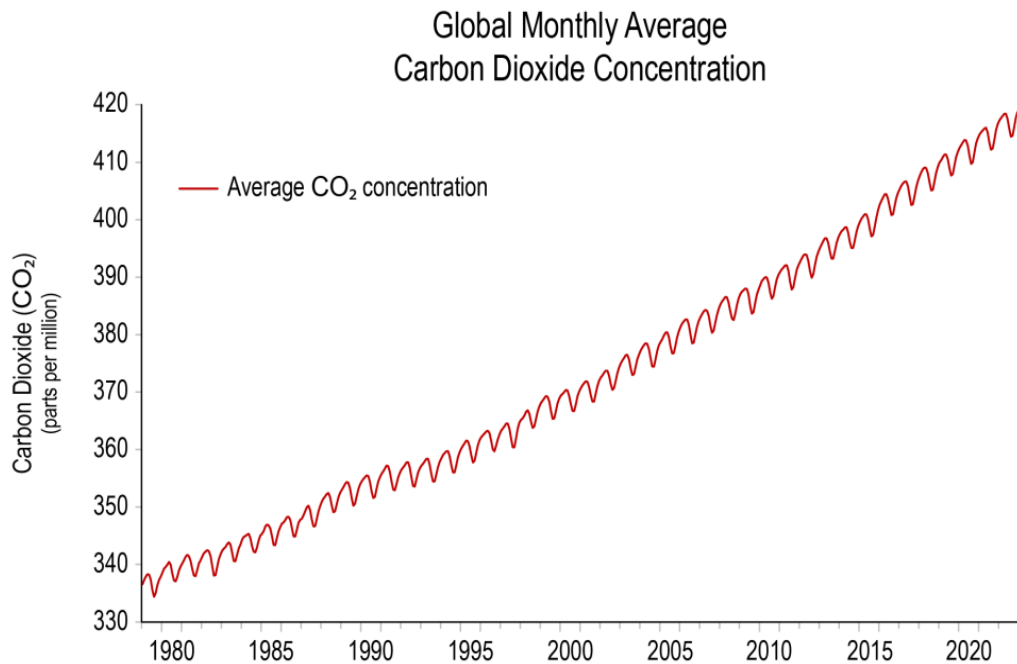
Figure 1.1 Concentration changes of CO_2 over the years.

Developed nations ought to take the lead in combating climate change and its aftereffects [6]. The human factor is the primary cause of the sharp rise in CO_2 concentration. While some CO_2 is released into the sea, which causes ocean acidification, the majority is discharged into the atmosphere, which leads to global warming[7].

Climate change policies are attributed to both CO_2 and non-CO_2 emissions in many countries across the world. Carbon taxes and emissions trading schemes (ETSs) are two examples of climate change policies that are now vital instruments for cutting greenhouse gas (GHG) emissions and slowing global warming. For instance, in a few countries like Mexico, non-CO_2 emissions made up 40–92 percent of all GHG emissions.[8] This implies that the results of climate change policies in different nations may differ significantly based on methods used to assess greenhouse gas emissions and to implement policies [9]. One of the most urgent problems facing the global world is addressing climate change. Climate change is facilitated by

greenhouse gas emissions, particularly carbon dioxide (CO_2). 2018 saw a 2% increase in worldwide CO_2 emissions, which is the highest rate in the previous seven years [10]. 2018 saw a 1-degree Celsius rise in average global temperature surface over the pre-industrial baseline. The four warmest years on record from 2015 to 2018 served as additional evidence of the long-term warming trend. The Intergovernmental Panel on Climate Change (IPCC) states that in order to keep global warming to 1.5 degrees Celsius over pre-manufacturing levels, significant cuts in CO_2 emissions from the energy, urban infrastructure, and industrial sectors must be made [11].

Reducing carbon dioxide releases from industrial processes is crucial in order to mitigate the impact of CO_2 on climate change. The utilization of CCS techniques lowers CO_2 emissions. Nowadays, a lot of carbon capture technologies are becoming available for purchase to lower CO_2. Capturing carbon dioxide from large-scale power plants, industrial operations, and transportation is their main goal. The practice known as Carbon Capture Utilization or Storage (CCUS) allows for the capture of carbon and its subsequent use in the production of useful products.
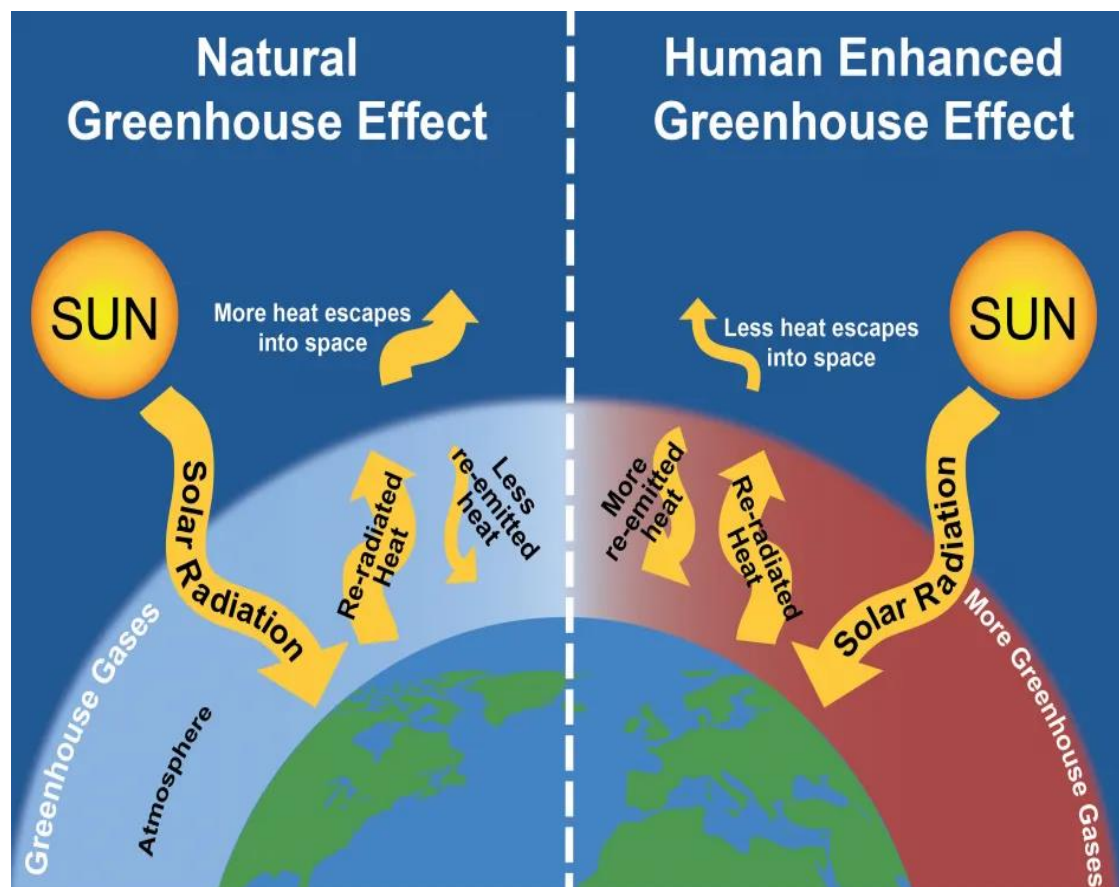
Figure 1.2 Greenhouse effects

3

1.3   Carbon Capture Storage (CCS)

The mitigation of climate change, which is perhaps an insurmountable barrier to our planet, depends heavily on capture and storage.[12] The process of capturing CO_2 is expensive and energy-intensive, and it is made more difficult by the variety of emission sources and their varying amounts, contents, locations, types, and industries or sectors. When UN Secretary General Antonio Guterres declared, "We are in trouble," in December 2018, he did not use hyperbole. We face many challenges as a result of climate change [13].
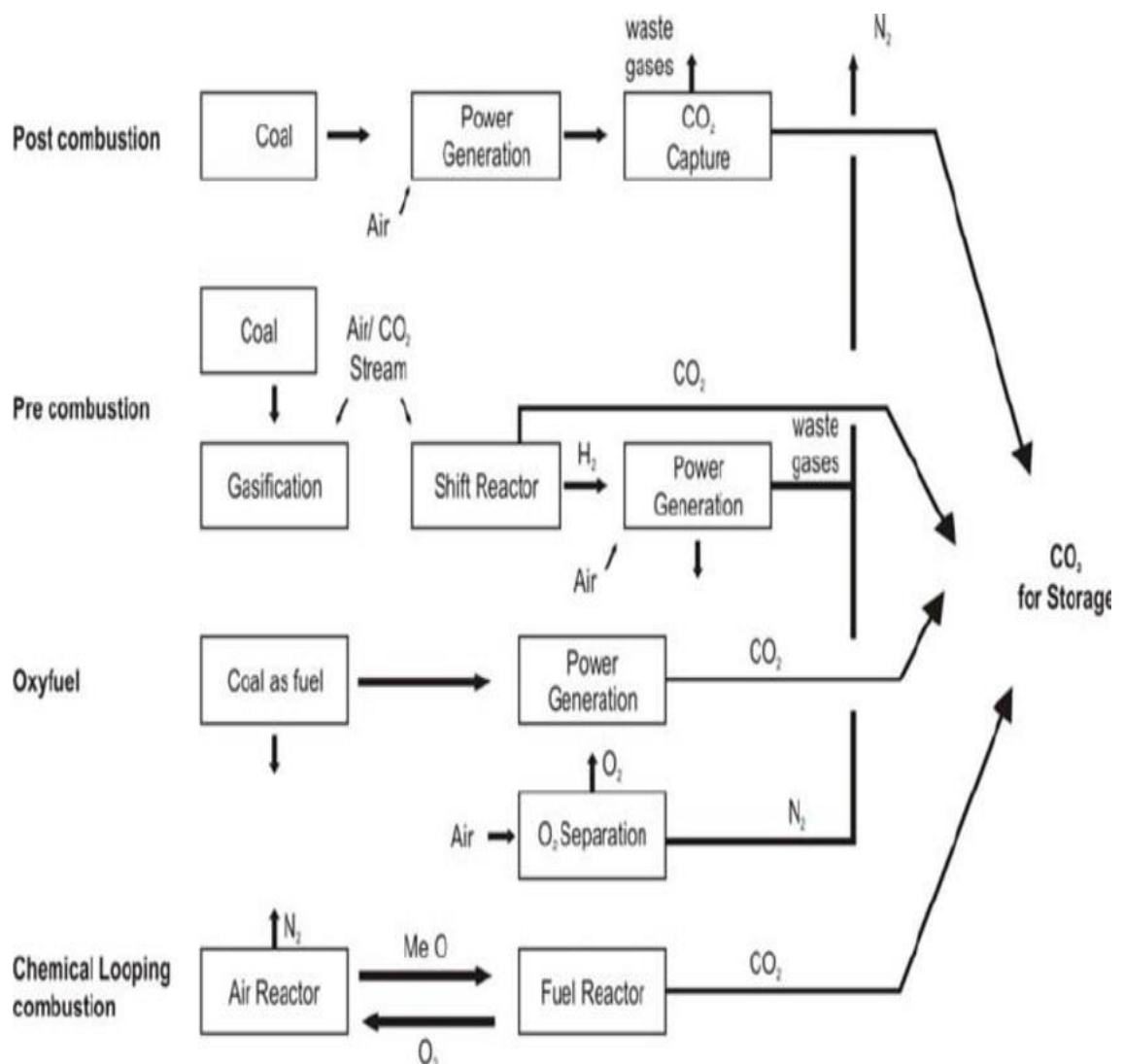
Figure 1.3 CCS techniques

There were just 800 GWh of total energy storage capacity in the world at the end of 2020 [14]. In order to prevent global warming, anthropogenic activity must attain net-zero greenhouse gas emissions by 2050 [15]. The goal of CCS technology is to

4

mitigate carbon dioxide emissions from the energy sector and energy-intensive industries, such as metallurgy, petrochemicals, and cement. CCS may cut CO2 emissions to the environment in modern conventional power plants by 80–90% when added to a plant without it. The introduction of CCS technology involves energy-intensive amine-scrubbing. Examples of second and third generation CCS systems that have been suggested to reduce costs are carbonate looping and chemical looping combustion (IEA, 2012). The industrial sector primarily uses four primary conventional carbon capture storage systems.

Following are the leading conventional technologies,

- Pre-combustion technology
- Post-combustion technology
- Oxy-flame technology
- Chemical Looping technology.

1.4   Pre-Combustion Technology

Pre-combustion technology is one of the most regularly used technologies. Pre-combustion carbon capture method uses an air separation device to extract oxygen from the surrounding air, which reacts with the fuel. The main output of this procedure is called synthesis gas, or syn gas.
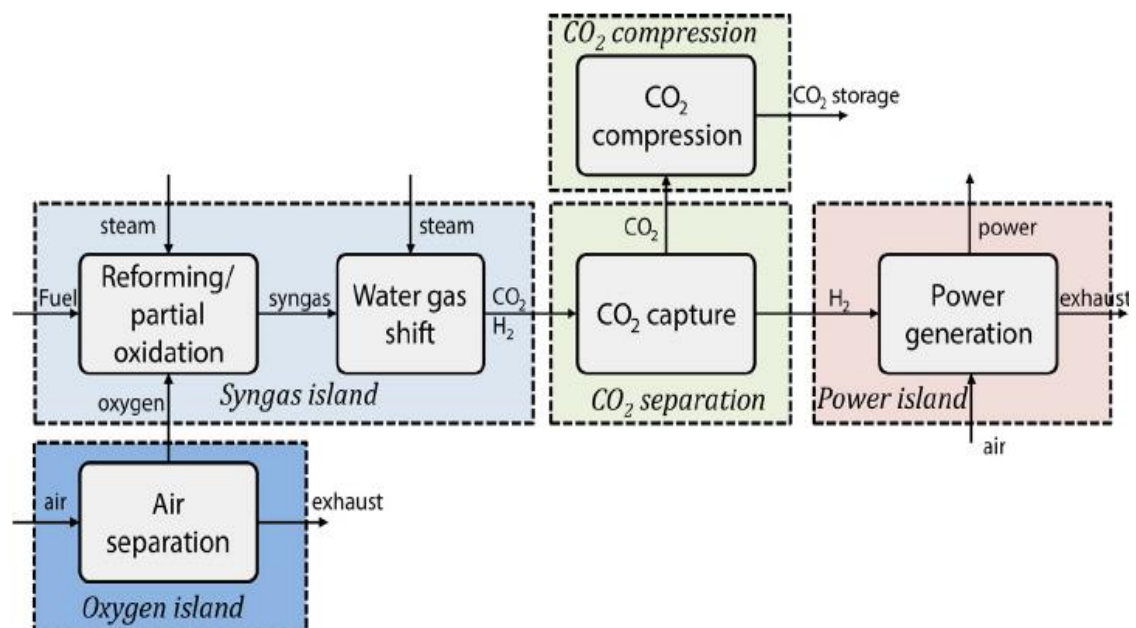
Figure 1.4 Schematic of Pre-Combustion Technology

The syn gas is composed of hydrogen and carbon monoxide. Afterwards, carbon monoxide from the syn gas is converted into CO_2 and H_2 by reacting with steam in a catalytic converter.

The most common name for this reaction is the shift reaction, which involves additional conversion of CO into CO_2. Following that, the CO_2 is removed using chemical and physical procedures, producing fuel gas with a high hydron content. In numerous other chemical reactions, the CO_2 is retained and utilized as a raw ingredient [16]. The pre combustion process schematic is displayed in the figure.

Due to the largest capital investment cost and the amount of labor required to deploy this technology in the industrial sector, it is still not developed enough to be used at the industrial level [17].

1.5   Post-Combustion Technology

This process uses membrane separation, adsorption, and absorption to remove CO_2 from the flue gases following the fossil fuels burning. It is the sole technology capable of retrofitting already-existing plants. CO_2 is extracted from flue gases, which have a high nitrogen (N_2) content, is the most challenging part of this technology. One benefit of post-combustion capture is that it can make use of current combustion systems without requiring significant modifications.
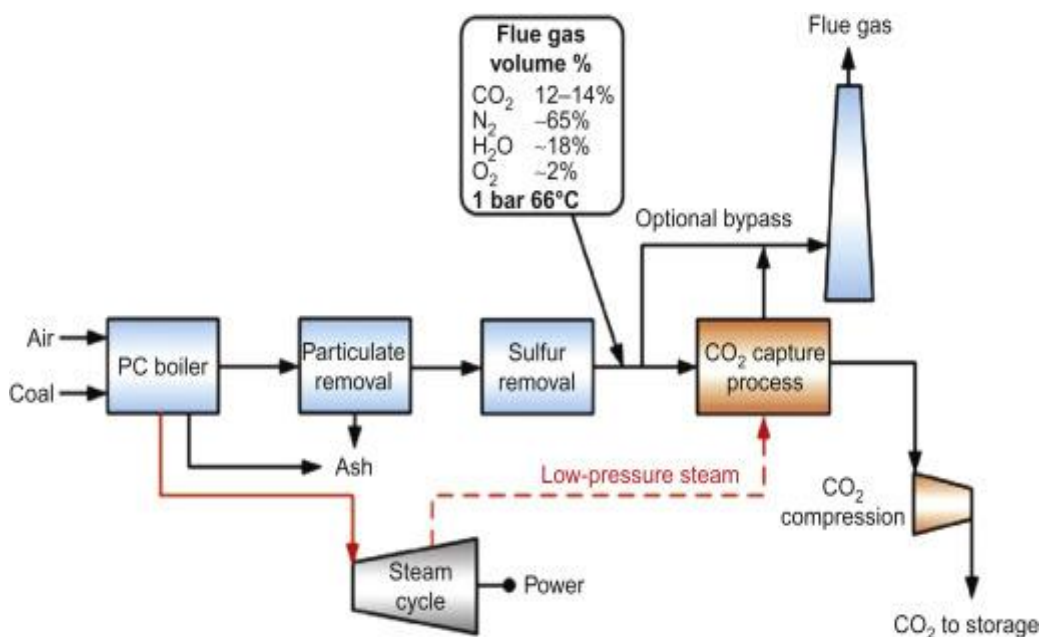
Figure 1.5 Schematic of Post-Combustion Technology

6

1.6 Oxy-Flame Combustion Technology

One of the most advanced methods for extracting CO_2 these days is oxygen-flame carbon capture. Using this process, fossil fuels are burned with seven pure oxygen molecules present rather than air. This can be used to increase the amount of CO_2 in the flue gases, which can subsequently be separated from the other gases. Water and carbon dioxide are included in the flue gasses. Dehydration is one of the methods of separating CO_2, and thermal purification is another. [12]
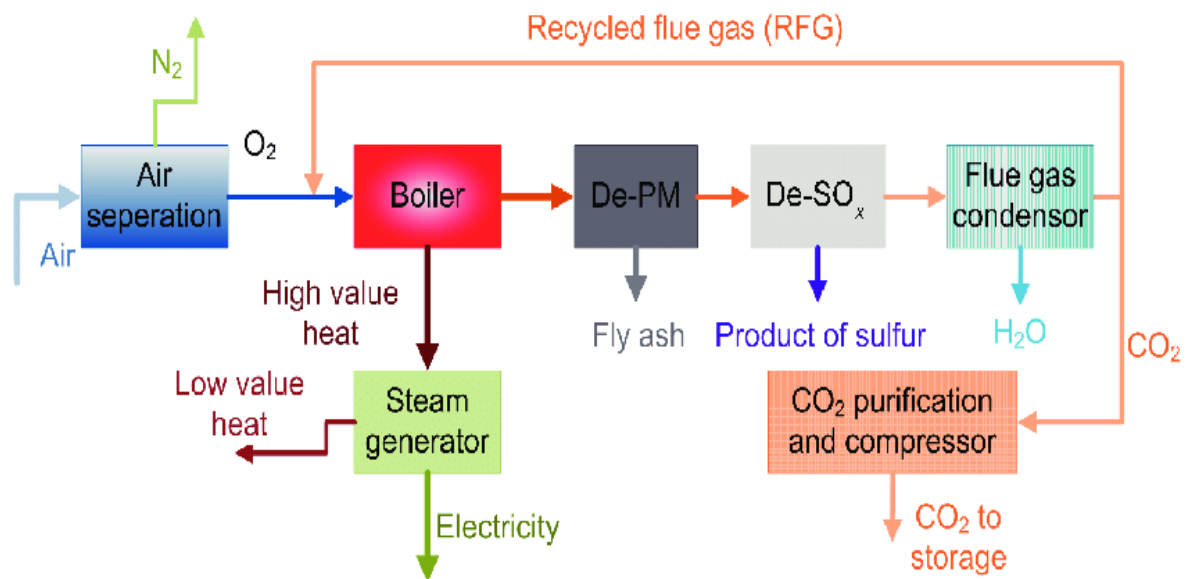
Figure 1.6 Schematic of Oxy Flame Combustion

Oxygen flame technology is preferable to post combustion carbon capture technology also because it does not allow N_2 to be present in the flue gases. Instead, it only contains CO_2 and water, is nitrogen-free, and requires less purification. With no N_2 in the gas stream, these techniques yield concentrated CO_2 and the maximum CO_2 recovery [18].

1.7 Chemical Looping Combustion Technology

The population of world is increasing faster than ever before, and this has led to a sharp rise in the need for energy in developing economies all over the world. The US Energy Information Administration (EIA) estimated that by 2040, the world's energy consumption would have increased by 28% from 2015. Particularly, the energy sector is anticipated to grow at the fastest rate and is responsible for 41% of greenhouse gas emissions linked to the use of fossil fuels [19]. The building up of oxygen from oxygen

carriers to fuel, which allows the oxygen carrier and fuel to come into direct contact, is the basis of the chemical looping process. [20]

The metal oxide (Me_xO_y) is reduced furthur to the metal (Me) or the reduced form of metal Me_xO_{y-1} in the first step, during which the fuel is reduced with the aid of metal oxide and CO_2 and H_2O are also created. Reaction (1) provides the global reduction process that is employed if the fuel fume composition is communicated as $CNH_{2m}O_p$. CO_2 and H_2O are present in the gas that is created during the eighth reaction. Following that, the gas is filtered and any water in it condenses, increasing the amount of CO_2 in the gas. Later, this CO_2 gas stream is prepared for storage and transit. This method's relationship to other carbon dioxide technologies is one of its advantages. This technology's primary advantage is that it eliminates the need for a separate separation unit since it has its own integrated CO_2 separation. Additionally, it saves the additional energy and money needed for the separation unit and the additional air separation unit. Redox reactions provide the basis of the chemical reaction system used in chemical looping technology. The following diagram 1.7 illustrates the generalize mechanism. The oxidation and reduction reactions are both a part of the chemical looping technology. Below are the chemical reactions that took place in the chemical looping technology. Both the metal and the reduced metal oxide are generated in reaction 1. which is subsequently further oxidized in a two-step reaction with air, readying this substance to initiate the new response.
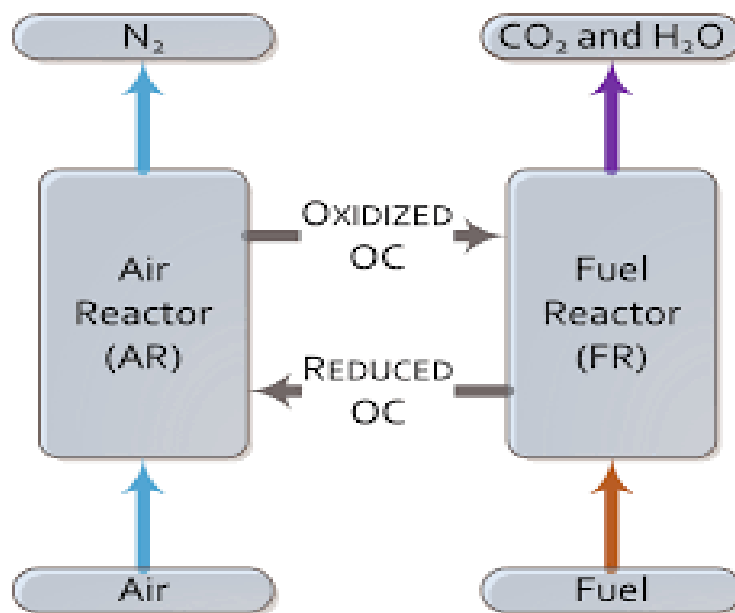
Figure 1.7 Scheme of Chemical Reactions in Chemical Looping Technology[21]

N_2 and the unreacted O_2 are present in the flue gas that is produced as a result of the reaction. Thus, the net chemical reaction consists of two phases, and as a result, the burning enthalpy is comparable to that of conventional combustion, in which process 3 involves burning the fuel in direct contact with oxygen from the air. This process yields a clean stream of CO_2 gas. As a result, the 9 chemical looping technology process produces the same total amount of heat evolution as conventional burning techniques [22]. We can reduce the amount of atmospheric carbon dioxide and create a safe environment for all living things with the aid of all these carbon capture technologies. These technologies are being used by many nations to eliminate carbon dioxide.

1.8 CO_2 Capture by Adsorbents

In the past years, there have been a significant rise in government finance and inspection operations for CO_2 capture, storage, and usage (CSU) due to growing understanding of the link between environmental CO_2 buildup and global warming. When it comes to CO_2 CSU, a variety of different equipment and emerging approaches often make extensive use of solid CO_2-adsorbents. These solid CO_2-adsorbents fall into three groups based on their adsor/desor temperatures as small, medium and high temperature adsorbents.

These adsorbents have three different temperature ranges: below 200 °C, between 200 and 400 °C, and above 400 °C. For every solid CO_2 adsorbent, the combination, interaction mechanism with carbon dioxide, adsorption performance, possible problems, and applications are discussed. The final section covers some unique CO_2-sorption-improved catalytic advances. In addition to summarizing the key areas of research in this field, this study seeks to find any connections that might exist between basic research and practical applications in industry [23]. Numerous absorbent kinds are employed, such as metal organic framework adsorbents, carbon-based adsorbents, zeolite, alkali earth metal, and silica-based adsorbents. Because carbon-based adsorbents are thermally stable, they renew with less energy. The only issues with carbon-based adsorbents are their small pores, poor surface area, and low adsorption capacity. The MOF adsorbents have good structure, pore size, and appropriate adsorbent quality.

Zeolite adsorbents do have some limits, though, in that their adsorption diminishes with temperature.[24] These adsorbents have a very hydrophilic character. 10% of the moisture in the zeolite adsorbents may be inactive. Because MOF exhibits a high rate of adsorption, among other distinct qualities and characteristics of adsorbents, its application as an adsorbent is comparatively broad to that of other adsorbents [25].
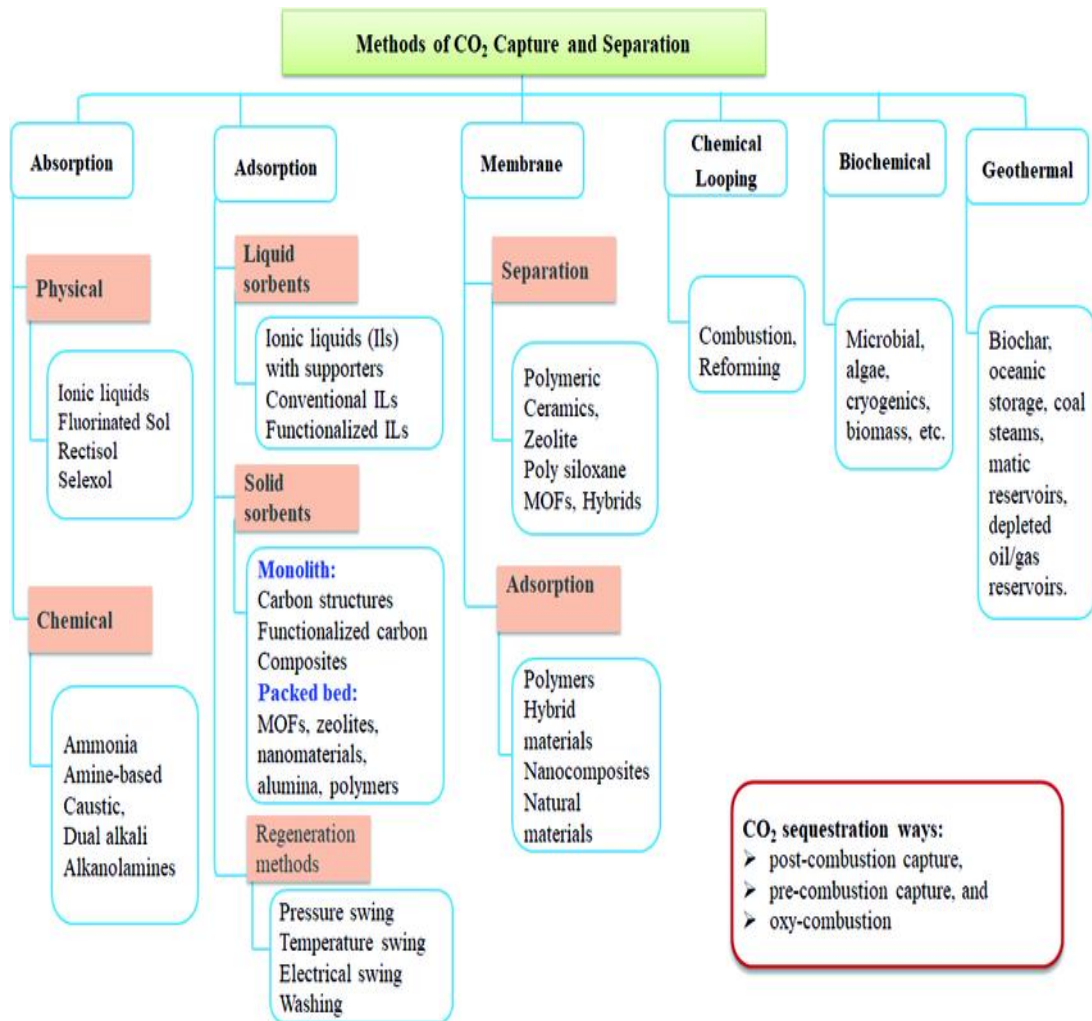
Figure 1.8 Adsorbent used for CO_2 capture

An important consideration in the adsorption of CO_2 is the choice of adsorbent. Prior to selecting an adsorbent, a few factors are considered. The adsorbents' composition, characteristics, and structure are determined by the parameter.

The factors that determine the capturing capacity of the adsorbent, its mechanical and chemical stability, and its high CO_2 selectivity are the adsorption and desorption kinetics, operating conditions, pressure and temperature conditions, the pH of the adsorbents, and the surrounding temperature and moisture [26].

1.9 Metal-Organic Framework (MOF)

Transparent hybrid materials called Metal-Organic Frameworks (MOFs) combine metal ions with organic molecules to create a three-dimensional structure. The material is well-known for its large surfaces and high porosity, and its sections enable a large variety of combinations of inorganic and organic blocks. Millions of different buildings can be constructed using these building bricks. MOFs are significant for a variety of industrial processes because of their distinct qualities, which include their large surface areas and variety of topologies.[27] MOFs can be used for a variety of tasks, such as medicinal administration, adsorption conservation, gas storage and transit, gas separation, and aquatic absorption. MOFs are incredibly delicate and spongy, possess the largest surface area of any known material, and their structure may be customized to fit a range of uses. For instance, the MOF structure can be modified to selectively trap some gases and chemicals while permitting the passage of other substances. MOFs are thus ideally suited to separation processes. The fact that gas storage efficiency has increased is also noteworthy. Because of their large surface area, MOFs may absorb large amounts of gas, increasing their storage capacity [28]. MOF is a promising option for gas adsorption, capture, and storage. Once the gas is stored, it will desorb it, which may then be utilized to produce other materials. Numerous methods can be employed to create highly functionalized MOFs.

Metal ions or clusters   Organic linkers   Metal organic framework (MOF)
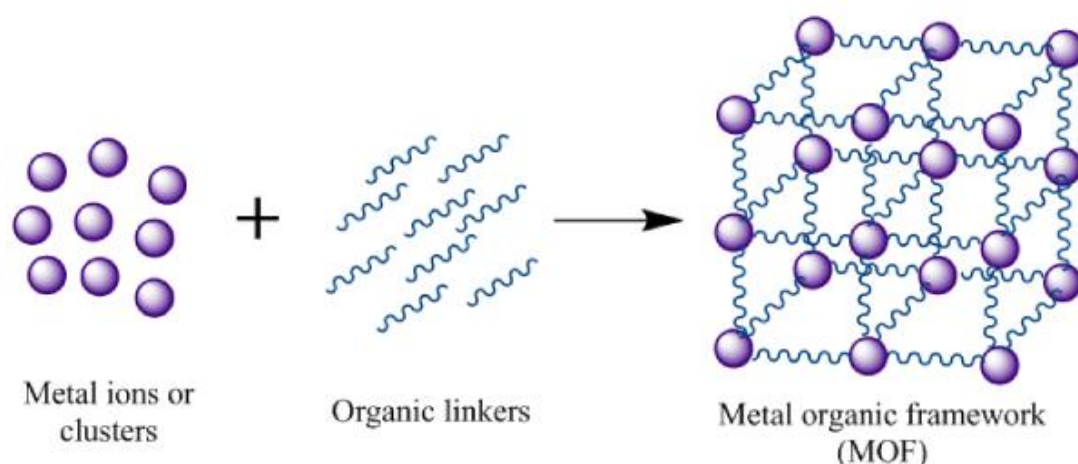
Figure 1.9 MOF structure

The most common technique is solvothermal batch reaction, which also necessitates the use of a solvent like N, N-Dimethylformamide and high temperatures (160–

250°C) and lengthy reaction times [29]. Various mechanisms are employed by MOFs to bind CO_2 within the framework. The two ways via which the MOF functions generally are physisorption and chemisorption. The mechanisms stem from variations in CO_2's adsorption affinity on the surface.[30] In physisorption, there is a minimal chemical contact between the CO_2 molecules and the adsorbent. By using very little energy, this bonding process can be readily reversed. The primary reason for the physisorption mechanism in MOF is the dipole forces of attraction between weak nucleophilic groups and the CO_2 molecule. The MOF and the carbon dioxide molecules have high forces of attraction, even though there is little pressure throughout the chemisorption process. Covalent bonds are formed during chemisorption at low pressures, whereas physisorption produces covalent bonds under high pressures. Molybdenum oxide (MOF) is a promising option for gas adsorption/capturing, storage, and desorption. The gas is then utilized to produce other products [31].

1.10 MOF Selection Criteria

One of the most crucial and significant procedures is choosing the right MOF; this should be done in accordance with the applications that the MOF will be used for. The MOFs that are utilized for CO_2 adsorption need to meet the following requirements.

- The MOF need to have a large surface area and a high adsorption capacity. The MOF's adsorption capability is determined by the pressure/temperature isotherms. [32]
- The MOF must have a high and quick rate of adsorption; this indicates that desorption is occurring at a rate that is superior to that of adsorption.
- The MOF should be highly selective towards CO_2, with adsorption selectivity defined as the ratio of CO_2 to additional gaseous components such as oxygen, methane, nitrogen, and so forth.
- The stability establishes the MOF's lifeline and the interval at which it should be replaced. The strength of the MOF should increase when this element is taken into account.
- The MOF should be inexpensive.
- The MOF is environmentally friendly and has no negative effects.

- Both mechanical and chemical stability should be strong in the MOF [31], [33].

There are numerous screening variables that go into selecting MOFs for CO_2 utilization. These factors include the MOF's selectivity, or how much it is selective for CO_2, ease of synthesis, which is important because it affects cost, the MOF's high affinity for CO_2, which means that more adsorption occurs, the MOF's hydrophobic nature protects it from atmospheric moisture, the morphology, which includes surface area, pore size, and pore volume, is also important, and the most significant aspect of the MOF's screening is its regenerate ability, which should only be used for MOFs with exceptionally good regenerate ability [33].

1.11 Copper MOF

Cu-BTC, or copper (II) benzene-1,3,5-tricarboxylate ($C_{18}H_6Cu_3O_{12}$), is a highly porous metal oxide film (MOF) comprising [$Cu_3(BTC)_2(H_2O)_3$]n with linked [Cu^2 $(O_2CR)^4$] units, where R is an aromatic ring. It is sometimes referred to HKUST-1 [34]. The accessible porosity of the 3D structure exceeds 40% of the solid with a pore diameter of 1 nm. Cu-BTC, which features open metal sites (unsaturated Cu centres) that are assumed to promote the binding of small gas molecules, especially polar ones like water, is one of the most studied MOFs. The actual use of Cu-BTC may be complicated due to the approximately 5-7 vol% of water vapor present in the exhaust gases.[35]
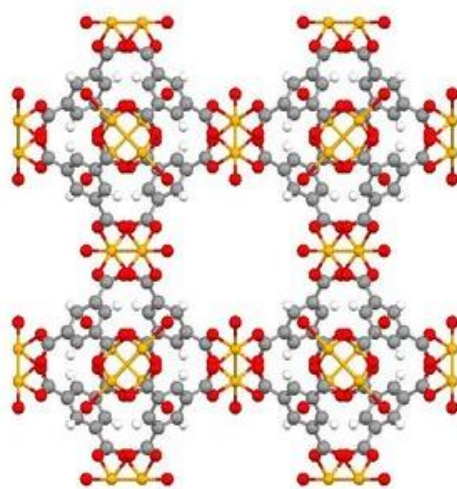
Figure 1.10 Cu-BTC's unit cell crystal structure as seen in the [100] direction. Cu stands for orange, O for red, C for gray, and H for white.

Cu-BTC's high moisture sensitivity is one of its main drawbacks. Several methods have been tried to improve the material's hydrolytic properties, such as coating it with hydrophobic compounds and modifying it by adding hydrophobic functional groups. These methods have been very successful in increasing hydrolytic stability, but they have the drawback of being time-consuming, requiring complex equipment, and having hard conditions of synthesis, which makes feasible application difficult. Cu-BTC has been utilized for the adsorption of several gases (CO, CO_2, CH_4, H_2, O_2, N_2), but other carbon-containing and MOF composites have been researched to enhance its characteristics.

1.12 Adsorption mechanism of Copper MOF

Another strong MOF with open metal sites is [36] CU-BTC ($Cu_3(BTC)_2$, Cu–BTC), whose CO_2 collection capabilities have been extensively studied both under ideal circumstances and following chemical alterations[37], [38]. Cu-BTC, initially reported by Chui et al. [39] is a mixture of dimeric cupric tetracarboxylate units, where water molecules are arranged on the axial locations of the paddlewheel units. It is the result of the synthesis between trimesic acid and cupric nitrate. This material may be visibly observed to transition from turquoise to dark blue[40] upon further activation, mostly by heat treatment under vacuum, which eliminates these water molecules and gives accessible open Cu^{2+} binding sites. This section covers CU-BTC's additional known adsorption sites in addition to the Cu^{2+} open site, regardless of whether they are connected to structural flaws or tiny cages in the substance. Moreover, CU-BTC exhibited the same rotating motion of the MOF-complexed CO_2 that was investigated for MOF-74-Mg. In terms of its moisture stability, PXRD investigations proved the existence of water, which was identified by the reflection intensity of the 311 plane, which is connected to the Cu^{2+} accessible binding site and controls the amount of hydration or the CO_2 loading capacity. The present temperature and moisture both demonstrated the degradation of this MOF, and the mechanism of degradation, which was stated to be begun by water dissociation caused by the H_2O–MOF complex, was ligand displacement.

Bordiga et al. [41] used spectroscopy to examine the CO_2 interaction with the metallic Cu^{2+} centre. They did this by loading 9 mbar of CO_2 at 150 K into a CU-BTC sample

and gradually lowering the equilibrium pressure to 0 as the temperature rose to 300 K. The red shift of CO_2 gas phase frequency from 2348 cm^{-1} to 2334 cm^{-1} at low coverage indicated the Cu^{2+} contact with the carbon dioxide, in contrast to the bare Cu^{2+} cation interaction with CO_2, which exhibits a usual blue shift. Remarkably, because CU-BTC contains around 1% of its native isotope, the interaction with $13CO_2$ was also found. Consequently, it was demonstrated that CU-BTC included two marginally distinct Cu^{2+} adsorption sites, which were mostly linked to (i) Cu^{2+} that was present on the exterior surface and/or associated with structural flaws and (ii) Cu^{2+} that was present in the MOF's interior framework. Accordingly, a XAFS study[42] also showed that CO_2 physisorption takes place when the CO_2 molecule binds to the CU-BTC Cu^{2+} center.
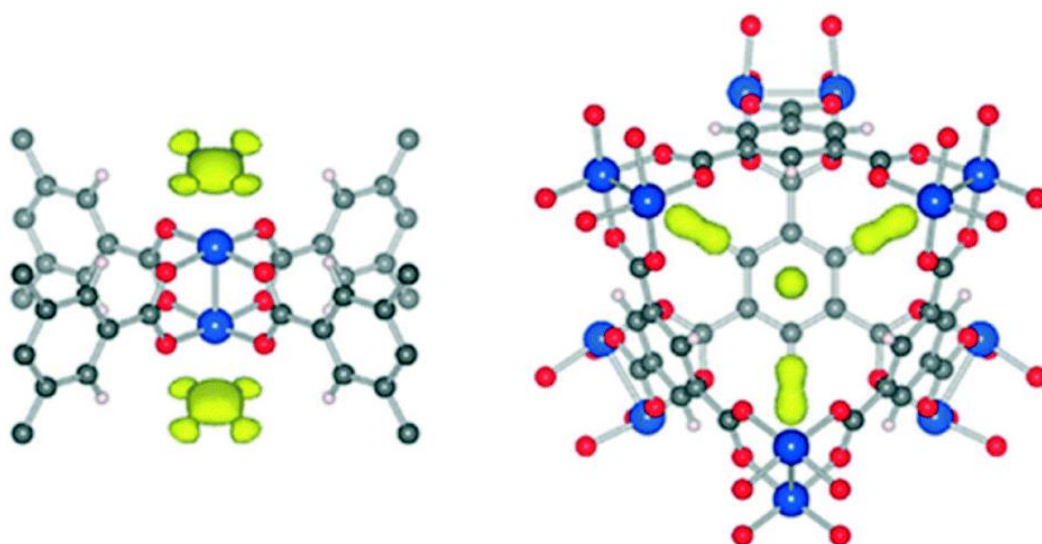
Figure 1.11 Primary adsorption sites and Fourier difference maps of CO_2 adsorption on CU-BTC. The tiny octahedral cage's triangular window opening is located on the right side of the triangle shaped Cu^{2+} site. [43]

Yan et al. [44]used the same methods as they used for MOF-74-Mg (see above) to conduct neutron diffraction tests in addition to theoretical calculations for CU-BTC in order to further investigate the CO_2 interaction with the framework. Analysis of the Fourier difference maps revealed two primary adsorption sites during CU-BTC activation at 150 °C for 24 hours (Fig. 1.11). As anticipated, the strong electrostatic interaction between Cu^{2+} and the quadrupole moment of CO_2 causes the favored adsorption site to be Cu^{2+}, which is initially filled by CO_2 molecules at low loadings (Fig. 1.11, left). A second adsorption site was found when the CO_2 concentration was raised; the CO_2 molecule filled the tiny octahedral cage's window opening (Fig. 1.11,

right). Since the tiny cage allows a single CO_2 molecule to connect with several surfaces, increasing the adsorption potential, the additional adsorption site was attributed to greater van der Waals interactions. Grajciar et al.[43] additionally reported on such numerous adsorption sites through their theoretical and experimental research on CO_2 adsorption over this substance.
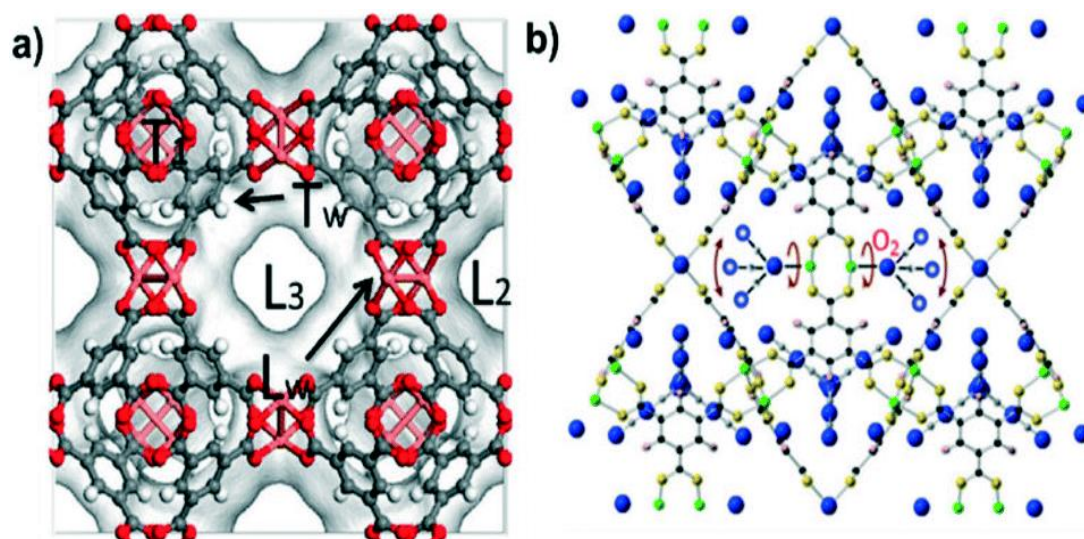
Figure 1.12 a) shows the CU-BTC simulated adsorption sites, which are L_3, L_2, L_1, T_w, and L_w. **b)** Theorized rotation disorder (red arrows) of adsorbed CO_2 molecules on the Cu^{2+} sites (green) (oxygen, blue; carbon, grey). [45]

Gutiérrez-Sevillano et al. [45] proposed five potential adsorption sites in Cu-BTC (Fig. 1-12a), denoted as L_3, L_2, L_1, T_w, and L_w, based on molecular simulations. The bigger core cavities L_2 and L_3 of 9 Å are surrounded by the smaller 5 Å cavity T_1, whereas only the latter has copper sites pointing into the pore. L_w stands for the windows that connect L_3 and L_2, while T_w is the triangular aperture that joins T_1 and L_3. According to their findings, T_1 is the preferred adsorption site for CO_2 in Cu-BTC for all loadings examined, which ranged from 4 to 192 molecules per unit cell. The preferred attraction of CO_2 was also ascribed to its molecular size and quadrupole moment, which resulted in its preferential adsorption in the tiny tetrahedral cage T_1.

Wong-Ng et al. [46] published an in situ PXRD research on CO_2 adsorption on Cu-BTC in 2016 by finding CO_2 molecules inside the framework. This diffraction peak increased as water was removed from the MOF structure and gradually decreased when CO_2 was exposed, as demonstrated by the examination of the 311-reflection intensity fluctuation upon dehydration and more CO_2 adsorption. This demonstrated that the binding sites' empty spaces during dehydration (activation) were later filled

with CO_2 molecules. Furthermore, in the case of an end-on configuration, the lack of a discernible change in electron-density peaks for adsorbed CO_2's "free" oxygen ($Cu^{2+}\cdots O$[double bond, length as m-dash]C[double bond, length as m-dash]O) was ascribed to the rotational motion of CO_2 (Fig. 1.12b), which was reported to maintain an interaction Cu–O–C angle of approximately 110°.

Supronowicz et al. [47] also found a flexible CO_2-framework connection and a comparable Cu–O–C interaction angle. The geometry of CO_2 was almost linear in their investigation of the interaction of tiny gases with an unsaturated Cu^{2+} core of CU-BTC, and the interaction angle of Cu–(O[double bond, length as m-dash]C[double bond, length as m-dash]O) was calculated to be 120°. A detailed analysis of CU-BTC's structural integrity breakdown upon exposure to water was conducted, primarily to comprehend the process of dissociation and to consider the possible uses of this copper-based MOF. Interest in this area is especially crucial for the extraction of CO_2 from the flue gas stream, which is a post-combustion coal-fired power plant that contains up to 5-7 percent water.[48]

Hence, Gul-E-Noor et al. [40] used solid-state NMR spectroscopy to examine the impact of water adsorption on the structure of CU-BTC. The stability of the CU-BTC framework was shown to be unaffected by changes in the ^1H MAS spectrum profile even after 60 days when exposed to modest levels of water (0.5 mol equivalent with respect to the copper atom), provided that the exposure period and water amounts were controlled. Nevertheless, several breakdown mechanisms were postulated based on rising amounts of water (0.75, 1.0, 1.5, 2.0, and 5.0 mol equivalent) because, during a 60-day exposure period, there was no discernible relationship between the water content and the alteration in the spectrum profiles. For example, after reacting with 1.0 mol equivalent of water, the ^1H MAS NMR spectra showed no change in profile over a period of 12 days. In contrast, the sample's ^1H MAS NMR spectrum showed very little change over the course of the experiment, which lasted 60 days, when exposed to 5.0 mol equivalent of water.

The ^{13}C NMR spectra were obtained for the samples containing 2.0 and 1.0 mol of adsorbed water after 12 and 21 days, respectively, in order to further examine the alteration in the chemical surroundings of the framework. Both the aromatic and carboxylate forms of carbon showed signs of an expansion in their respective signal

ranges for the sample treated with 1.0 mol equivalent of water. Narrow resonant frequencies at 180 ppm and 130–140 ppm were also detected. In the absence of the paramagnetic environment of Cu^{2+}, which greatly affects the surrounding electromagnetic properties due to interactions between the unpaired copper electron and its surroundings, they are characteristic of trimesic acid, a free ligand. For the sample containing 2.0 mmol equivalent of water, it seems that most of the carbon chemical shifts were caused by the diamagnetic free ligand. Since the linker and the paramagnetic copper atom did not interact, this shows that the pristine chemical structure was damaged.

Fan's group [49] also looked into the moisture stability of CU-BTC; they analyzed the samples following water sorption experiments with a 90-hour exposure period. When the PXRD patterns of the source material and the CU-BTC were compared at 25°C and 90% relative humidity, it was found that the pristine sample's diffraction pattern was preserved, although there was a noticeable rise in the amorphous background.

At 50 °C and a relative humidity of 70%, the crystalline structure held steady for greater humidity levels; however, when the humidity reached 90%, it completely disintegrated. In a further investigation, [50] the Cu-BTC samples were subjected to water vapour studies at temperatures ranging from 90% relative humidity to 0% using small-angle X-ray scattering differential scanning calorimetry (DSC) and infrared spectroscopy. The sample subjected to water vapour at 25°C showed a drop in crystallinity, and at 50°C there was a complete loss of structural ordering, as validated by SAXS measurements. The scientists argue that the temperature cannot be solely blamed for the collapse of the structure, since the thermal stability of CU-BTC reached temperatures as high as 260°C. They further state that the presence of water is crucial for maintaining long-range order. They discovered the presence of free carboxylate groups by further examining the sample's infrared spectra at 50°C. Additionally, a highly intense peak at 315–345°C which was absent from the other samples was discovered by the DSC analysis. The peak demonstrates how the water coordinates with the metal centre at 50°C in a humid environment, causing the ligands to be displaced from the framework. The pure trimesic acid ligand DSC curve illustrates this association.

Xue et al. used ab initio simulations of molecular dynamics and DFT calculations to look into the first steps of Cu-BTC's hydrolytic process. This helped him understand why the crystal structure breaks down when water is present. The three steps in the suggested mechanism—adsorption of water, movement of the ligands, and release of water which break downs the Cu-BTC framework when water is present. They showed that an acid-base Lewis reaction splits the water first at the Cu^{2+} centre, and the water gives the copper cation its free electron pair. It was found that the stretching of the Cu–O carboxylate bonds is linked to the process of water adsorption, particularly if one water molecule sticks to one side of the Cu–Cu dimer. That being said, this effect could not be seen when there were two water molecules attached to Cu–Cu node cluster opposite sides.

Based on the existence of one, two, or three water molecules, three scenarios for the ligand displacement step were examined. In the case of one or two water molecules, water adsorption occurs first, which is followed by the $Cu–OH_2$ bond shortening and the Cu–O carboxylate link breaking. Even if the linker has one broken bond, the structure will not fall apart. Because CU-BTC is symmetric, at least two ligands' bonds at one side of the dimer would need to be disrupted. Because of the large activation barrier free energy, it would be difficult for the following water dissociation to proceed while attached to the Cu^{2+} centre. Nevertheless, the presence of three or more molecules close to the MOF caused two ligands to completely separate from the metallic centre, likely destroying CU-BTC's crystalline structure. This theoretical analysis is a pertinent contribution to the complete knowledge of this hydrolytic mechanism since it corroborates well with the experimental findings of water exposure and structural collapse.

Álvarez et al. [51] demonstrated the acidic nature of water's reaction to the breakdown of the framework by examining HKUST-1's stability in the presence of ethanol and water. PXRD diffractograms demonstrating its greater stability in ethanol after 9 hours of independent exposure to both solvents demonstrated that its structural crystallinity deteriorated in water. SEM was also used to assess the samples' morphology.

The sample exposed to ethanol maintained the pristine material's double-sided pyramidal structure, but the sample exposed to water mostly included needle-shaped crystals. The theoretical calculations showed a considerable reliance of stability on

the acidity of the solvent's proton. Consequently, as shown by PXRD, this proton exchange promotes the disruption of the carboxylate (linker)–copper connection, resulting in a partial loss of crystallinity. The authors presented that the water-degraded framework diffractogram might have two possible phases: (i) a Cu-BTC coordination polymer one-dimensional chain and (ii) a stacked structure of [Cu_2 OH(BTC)(H_2O)]. However, it was not possible to see a full breakdown of the structure.

1.13 Methods for the Synthesis of MOF

The common method for creating MOFs is liquid phase synthesis, which involves dissolving the metal salts and organic synchronization primitives in a solvent. Alternatively, a solvent is added to a combination of metal salts and organic linkers inside a reaction vial. This synthesis technique remarkably depends on the choice of solvent. depending on many physiochemical characteristics, such as strength, reactivity, stability, and so on. In addition, strategies for solid phase synthesis are also disclosed. In contrast, it is less labor-intensive and speedier, but it has certain disadvantages, such as the difficulty in obtaining single crystals for product structure determination [31].
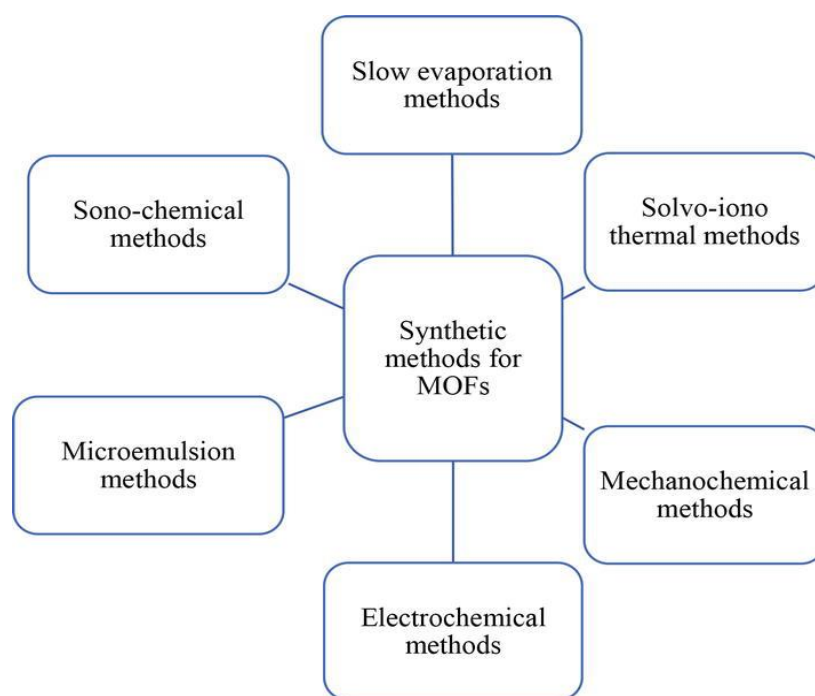
Figure 1.13 Different methods for the Synthesis of MOFs

1.13.1 Solvothermal or Hydrothermal Method

Solvothermal reactions are carried out at pressures higher than the solvent's boiling point in closed reaction vessels. Under the solvothermal approach used in the MOFs synthesis pathway, initial materials undergo some degree of unanticipated and hence unexpected chemical modifications.

It occurs often as a result of the development of nanoscale morphologies that are unattainable by conventional methods. Solvents with high boiling points, mostly organic, have been used in the solvothermal technique. The most often used organic solvents are DMF, methanol, ethanol, and so forth. 15 For reaction temperatures higher than 600°C, Teflon-lined autoclaves are typically utilized [33] [34].

Advantages

This process yields a significant quantity of MOF with a high yield. The MOF made by this method have excellent crystal size. The MOF produced using the solvo/hydrothermal technique has an excellent structure, a large surface area, and small pores. It has certain drawbacks as well, which are covered below.

Disadvantages

The primary disadvantage of this technology is its lengthy completion time. Additionally, due to the high cost of the solvents used in this procedure, it is an expensive method. [35]

1.13.2 Microwave Assisted Method

By using a microwave-assisted technique, MOFs can be synthesized incredibly quickly. This method is used to produce metal oxides at the nanoscale. One to two hours are spent heating a solution in a microwave. It produces nanoscale crystals. This process is known as "microwave-assisted solvothermal synthesis" for the production of MOFs.

The quality of the crystals produced by both solvothermal and microwave aided synthesis is the same, however the microwave assisted synthesis approach requires a substantially shorter reaction time [36]. Thus, by using the right microwave frequency, molecules vibrate, causing collisions and raising kinetic energy, such as temperature

or internal energy of the system. The direct interaction of microwave radiation with solutions is a method of kinetic energy enhancement that uses less energy. High heating rates and uniform heating are the results of this for the entire system [37].

Advantages

This method's benefit is that the crystals are exceptionally large. Another benefit of this approach is that, in comparison to the solve/hydrothermal approach, it is typically the fastest.

Disadvantages

This method's primary drawback is that it yields unsatisfactory ratings. Another drawback of this approach is that scaling it up is challenging [38]. Therefore, one may quickly determine whether or not to employ this strategy by weighing its benefits and drawbacks.

1.13.3 Electrochemical Method

It is possible to produce huge crystals of MOFs in room temperature by varying the pH or solvent for certain uses. Among them is the electrochemical synthesis technique, which offers the most important benefit of a modern synthesis procedure: continuous synthesis of the product without the need for any metal salt. The metal ion enters the electrolyte and organic ligand combination through anodic dissolution [39]. The following section discusses the benefits and drawbacks of this particular technique:

Advantages

The primary benefit of this approach is that, in comparison to other approaches, it is one of the fastest; it takes less than ten minutes to finish the synthesis and provide the appropriate experiment findings.

Disadvantages

This method has the following drawbacks. It produces very low-quality, poorly sized crystals. It has low surface area, low pore size, low pore volume, and extremely poor-quality crystals. It is also the most expensive method because electricity is required for the process, which drives up costs [40].

1.13.4 Sonochemical Method

The sonochemical method involves sound frequencies for the completion of the reaction, and it facilitates crystal formation. In this method at first the reagents are taken in a beaker and then the beaker containing is subjected to the sound waves having high frequencies. After the reaction the crystals are filtered out and then dried in vacuum oven.

Advantages

This expertise's main benefit is that it demands far too little investment and has a very short manufacturing time.

Disadvantages

The primary drawback of this process is its relatively low overall yield, which results in very little product being produced [41].

1.13.5 Spray Drying/Evaporation Method

Unlike the previous methods, this one doesn't involve the use of an outside force. This approach is the easiest to use for creating MOFs. Natural evaporation evaporates the solvent, and crystals are the byproduct of this process. That being said, the drawback of this approach is that it takes a lot of time, and the return is quite little. [52]

Advantages

This approach has very minimal cost and doesn't require any external force. When compared to other approaches, this one is the least expensive. This approach is among the easiest since it doesn't call for any outside procedures.

Disadvantages

This process's drawback is that it requires a lot of time; synthesizing the MOF with this method takes a long period. This method's extremely low yield is its second main drawback [43].

1.13.6 Chemical Flow Method

23

Another sort of approach where no external force is needed to finish the reaction is chemical flow synthesis. With this approach, no external force is used; the reactants are permitted to finish the reaction on their own. The range of average time is two minutes to six days. The needed temperature ranges from 303K to 573K. [53] Two gases or liquids are rapidly delivered into a mixing vessel using flow techniques, and the resultant mixture is then rapidly pushed via a tube. The concentrations of products or reactants can then be determined at various tube locations that correspond to various reaction durations, for instance, using spectroscopic techniques. The benefits of this method outweigh the drawbacks. The benefits and drawbacks of this approach have been covered below.

1.14 Applications of MOF

MOFs can be used for a number of purposes, including separation, magnetic, biological applications, catalysis, and dye degradation. Before creating MOFs, starting materials should be carefully selected to achieve the desired effects. MOFs performs not rely on particular uses; rather, they can be employed in a variety of contexts. For example, MOFs can be utilized as sensors, for gas separation and storage, in the delivery of drugs, and as catalysts in certain chemical processes.

These days, MOFs are crucial for gas separation and storage; in fact, a large number of MOFs are being created specifically for this purpose. Gases are a very useful source for producing energy, so having quality storage tanks is crucial for the efficient storage of gases.

There are plenty of choices available for this use, but some are too costly for everyday use or require multi-stage compressors or high-pressure tanks. As a result, some substitute, dependable, and less expensive storage solutions are required. The most researched and utilized material is MOF, which provides clean transportable energy in addition to acting as a substitute for gas storage and separation [46].

MOFs have several advantages over other porous materials, including high surface area, changeable pore size, variable functionalization, and convenient synthetic methods.
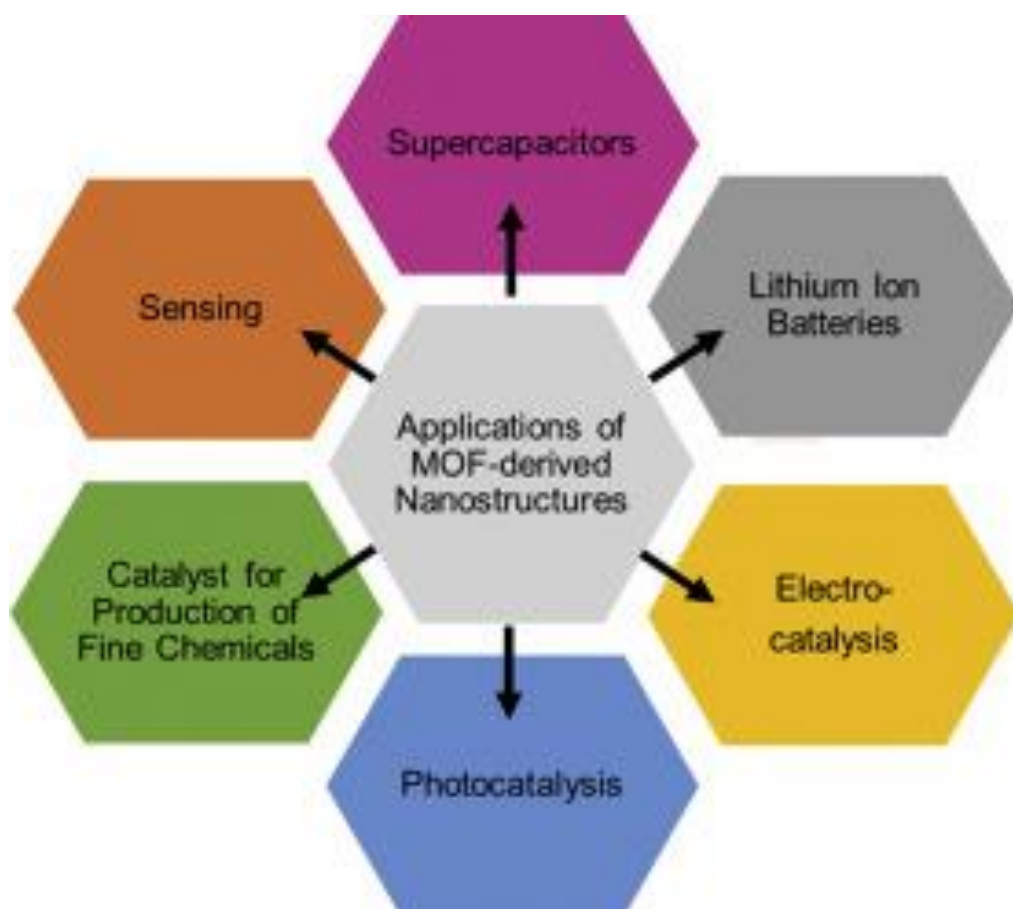
Figure 1.14 A few applications of MOFs [54]

1.14.1 Applications of MOFs in Carbon Dioxide Storage

Zeolites were the material that was traditionally utilized for the adsorptive removal of carbon dioxide. For this aim, highly porous activated carbon was also used with them. Because of its large surface area and polar functional group-lined pores, MOFs are presently thought to be viable adsorbents.

The presence of polar groups in the MOFs structure, such as $-NH_2$ or $-N$, which involve organic heterocyclic residue on the MOFs pores, has been demonstrated to be beneficial for high carbon dioxide uptake when compared to unfunctionalized analogues. By using ethylenediamine in a post-synthesis procedure, the imidazolate framework ZIF-8 is modified to improve its adsorption ability towards CO_2. At 298 K at 25 pressures, the modified ZIF-8 (ED ZIF-8) has nearly double the CO_2 adsorption capacity per surface area of ZIF-8. Its BET surface area has increased by

39 percent. The H_2O intake of the ED-ZIF-8 is substantially lower than that of the ZIF-8. Estimates indicate that at 0.1 and 0.5 bar, the ED-ZIF-8 selectivity for CO_2/N_2 sorption improves dramatically, up to 23.0 and 14.0, respectively, almost twice that of the ZIF-8. [54]

1.14.2 Application of MOFs in Dye removal

In wastewater treatment, adsorption is frequently employed to get rid of some naturally occurring pollutants. Living things are harmful to dyes, and getting rid of them can be challenging. Because they are likewise non-biodegradable, MOF can be utilised in this situation. [55]

1.14.3 MOFs as a Sensor

One of the key components of analytical chemistry is the electrochemical sensor.

The electrochemical sensor can offer us remarkable selectivity and sensitivity when compared to traditional methods like chromatography, inductively connected plasma mass spectrometry (ICP-MS), atomic sorption spectroscopy (ASS), and atomic emission spectroscopy (AES). Nowadays, a variety of MOF-based composites are being developed as effective electrochemical sensors for the chemical, environmental, and biological sciences. The applications of MOFs sensors in analytical chemistry are numerous. The MOFs sensors are also useful for gas sensing, organic compound detection, and heavy metal detection [50].

1.14.4 MOFs for Gas Separation and Storage

Because selective adsorption is dependent on a number of attractions under particular conditions, selective adsorption can be used to separate gases. The main tools used in gas separation are kinetic, quantum sieving effects, when using solid adsorbents, thermodynamic equilibrium and molecular sieving [51]. Since its invention in the late 1990s, a variety of gas separation and storage techniques have been used to create a large number of MOFs. Therefore, it is important to choose your ligands or functionalizing organic groups carefully in order to ensure that MOF functions as intended. For MOF to function properly, a new node is used to include another metal. We refer to this as bimetallic MOF. It possesses the dual characteristics of two metals

coupled to either one or more ligands. Overall, by including more metal nodes in the same framework, the defects in MOF can be enhanced, activity, porosity, and synergistic effects between metals can be increased by integration, and this can improve the intrinsic and transit characteristics of the metals.[56]

1.14.5 MOFs for Drug Delivery

One of the most important uses in both biological and human health care is drug delivery. Because MOFs self-assemble from a metal and organic linker under mild circumstances, they have a variety of uses in the biomedical area. MOF as a medication comparing carrier to other materials, we get the following benefit [53].

By employing amorphous MOFs, the duration of the drug's release can be extended from two to thirty days. It demonstrates that the amorphous structure of MOFs is sufficient to trap the drug inside its cavities to restrict drug delivery and decelerate drug molecule release. [57], [58]
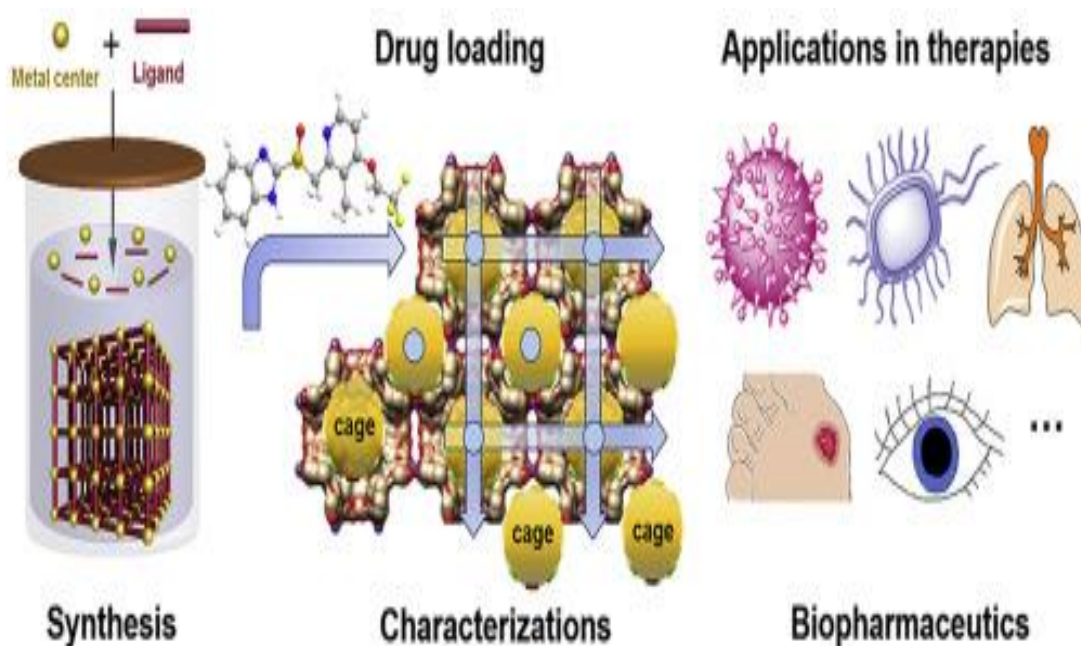
Figure 1.15 MOF as a Drug Delivery carrier

Numerous elements, including pore size, three-dimensional arrangement, and physiochemical properties, influence the drug delivery applications of MOFs and provide drug fitting in MOF cavities with versatility. However, because drug administration via MOFs occurs gradually and under control due to matrix

breakdown, it is more effective than drug delivery through nanocarriers. concurrently causes a burst effect on the drug's release later on. [57], [58]

1.14.6 Applications of MOFs in Hydrogen Storage

The fact that water is the only consequence of burning hydrogen in air and that there are no hazardous byproducts highlights the hydrogen economy. Hydrogen is hard to store at room temperature and atmospheric pressure. Because of its small weight. [59]

The main determinants of hydrogen storage in MOFs are their enormous surface area and several other characteristics. The ability of MOFs to store hydrogen has already been attempted and tested on a sizable number of them—up to over 300. Made from $[Zn_4O]$ clusters, MOF~177 exhibits a gravimetric hydrogen absorption of up to 7.5 weight percent. For MOF-5, a gravimetric hydrogen uptake of 7.1 weight percent was noted. Approximately 3800 m^2 g^{-1} of specific surface area is displayed by this MOF. When compared to other MOFs, this is thought to be extremely high [55].

Because they have a wide surface area, MOFs with open metal sites typically allow higher affinities between hydrogen and metal molecules. Their large surface area is one of the main factors contributing to their significant hydrogen storage capacity. Additionally, by doping the frameworks with metal ions, the MOFs' ability to store hydrogen can be greatly improved.

The most potential alternative energy source to address the issue of fossil fuel usage in the modern era is hydrogen energy. Hydrogen burns with three times the heat of combustion of petrol. Moreover, water is the only result of burning hydrogen. The two main components of hydrogen energy are the generation and storage of hydrogen. MOFs have a significant function not only in hydrogen storage but also in hydrogen generation. MOFs are used in photocatalytic and electrocatalytic production methods to produce hydrogen. Water splitting processes are powered by sun energy through the photocatalytic process. This reaction yields molecules of oxygen and hydrogen. The combination of active catalytic sites with light-harvesting units is made possible by the porous nature of MOFs. To increase photocatalytic activity of MOF, light-absorbing co-catalysts and chromophores , such metallic nanoparticles, can be introduced to their structure.. Another technique for producing hydrogen is the electrochemical conversion of water

into hydrogen molecules. To achieve the appropriate catalytic current densities, the electrocatalyst lowers the reaction's overpotential. For this process, MOF structures with catalytic qualities have drawn interest as electrocatalysts.

In electrochemical settings, the pure MOF structure is unstable and exhibits poor electrical conductivities. MOF structure is mixed with nanostructured materials like metal oxides or porous carbons to make it suitable as an electrocatalyst.

1.14.7 MOF as a Magnetic Material

As was previously mentioned, MOFs serve a variety of functions, and among them is the utilization of magnetic materials. A novel magnetic material has been created using MOF from the past 30 years. Even if a large number of MOFs are ready to be employed as magnetic materials, much effort needs to be done to fully transform them into such materials. [60]

Another name for the MOF is porous coordination polymers. When exposed to outside stimuli, the crystalline network of such a MOF experiences a dynamic shift. These substances are magnetically tunable from birth. The newest class of compounds that combines the functional capabilities of metal with its magnetic character are called magnetic framework composites.

1.14.8 Catalysis Applications

The ability of MOFs to engage in catalysis is one of its most significant characteristics. MOFs' hybrid structure can directly contribute to their catalytic qualities, or it can be enhanced by the addition of unstable yet catalytically active nanoparticles. The uniform dispersion of active sites throughout the framework is made possible by the periodic structure of MOFs, and the accessibility of active sites and the transportation of substrates and products are facilitated by the framework's pores and channels. Moreover, MOFs act as shape-selective catalysts due to their unique pore size and shape. [61]

Numerous researchers have used MOFs as photocatalysts, electrocatalysts, and heterogeneous catalysts. They are mostly employed in well-known organic processes as heterogeneous catalysts. For instance, HKUST-1, which has lewis-acid sites, can be used as an acidic catalyst in cyanosilylation and isomerization processes.

MOFs have the characteristics of semiconductors, which makes them suitable photocatalysts. The degradation of organic pollutants, different organic processes, the creation of hydrogen and oxygen from water splitting, and the reduction of CO_2 all benefit from the photocatalytic capabilities of MOFs. [62]

Because of its large surface area and pore volume, MOFs exhibit strong electrocatalytic capabilities after their weak conductivity is offset by the inclusion of nanomaterials. The oxygen reduction reaction (ORR), hydrogen evolution reaction (HER), oxygen evolution reaction (OER), and carbon dioxide reduction are the primary electrocatalytic uses of MOFs.[63]
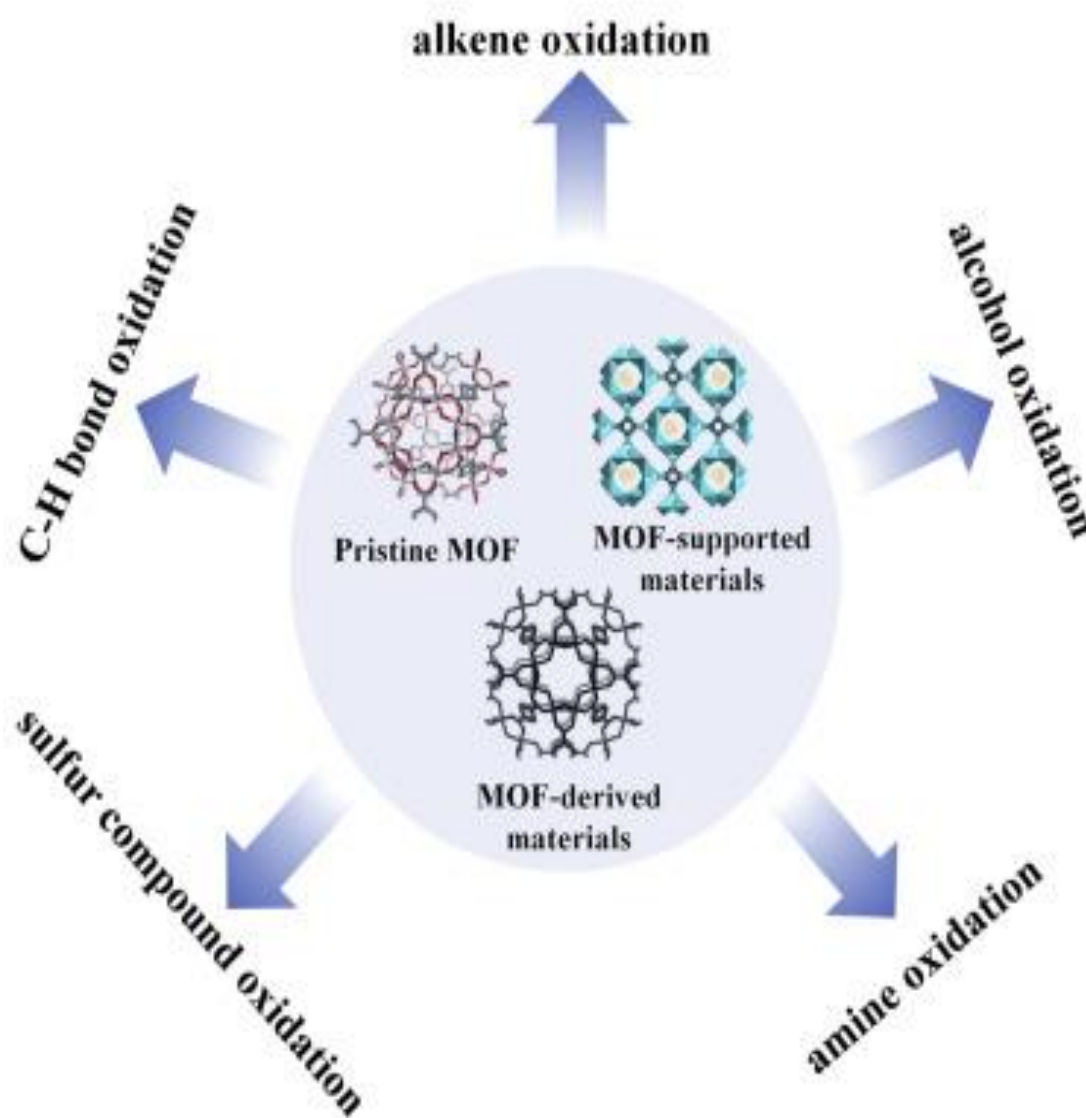
Figure 1.16 Catalysts based on metal-organic frameworks for the selective thermocatalytic oxidation of organic compounds [64]

1.14.9   Waste Water Treatment

Water is without a doubt the most important element in the universe. Numerous wastewater applications that include hazardous chemicals are generated, whether via daily use or industrial processes. Establishing efficient techniques for treating wastewater is therefore crucial. 8MOF structures can be used as a whole membrane system or as membrane fillers in membrane separation. Selective organic and inorganic component separation from water is made possible by their adjustable porosity structure. Every MOF structure employed in wastewater treatment is water-stable. There are two groups into which these MOFs can be separated. Hard acids and hard bases combine in the first group, whilst soft acids and soft bases combine in the second category to create strong bonds inside the MOF structure. Hard acid metal ions, such as Al^{3+}, Fe^{3+}, Cr^{3+}, and Zr^{4+}., are included in the first group. The UiO series and the MIL series are examples of this kind of water-stable MOF. [65]
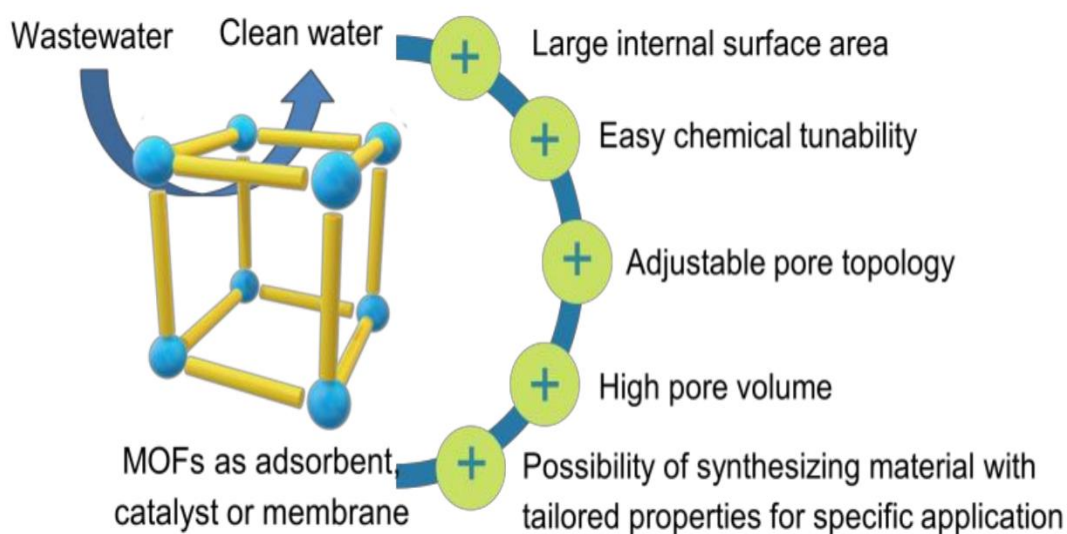
Figure 1.17 An example of the benefits of using MOFs as a membrane, catalyst, or adsorbent for the treatment of wastewater. [59]

Azolate ligands with soft base, such as tetrazolates, pyrazolates, imidazolates and trizolates as well as soft acid metal ions, such Zn^{2+}, Cu^{2+}, Ni^{2+}, Mn^{2+}, and Ag^+, are included in the second group. ZIFs fall within this group; they are made up of imidazolium linkage and Zn^{2+}. Because of their superior compatibility, customisable structure, high selectivity and permeability, and possibility for recycling after their lifetime, water-stable MOFs perform admirably in wastewater cleanup.

Although pure MOF films are suited for the physically and chemically challenging conditions of industrial applications and have strong thermal and chemical durability, their future application is limited by their expensive cost, complex manufacturing method, and processing challenges. Further research is necessary to fully understand the mechanism of film development, and the films' quality and thermoelectric qualities must be enhanced.[66]

1.14.10 Mixed Matrix Membranes

Mixed matrix membranes (MMMs) with a MOF as filler and a polymer matrix have several benefits over pure MOF membranes, including reduced costs, ease of manufacturing, superior mechanical strength, improved selectivity, and greater permeability. MMMs also have significant commercial application prospects.

A metal organic framework (MOF) known as HKUST-1 (Hong Kong University of Science and Technology $Cu_3(BTC)_2$ [67], [68] is made up of triangular 1,3,5-benzenetricarboxylate organic linkers and copper metal sites. It has a cubic, paddle-wheel shape. These water molecules can be eliminated following an activation step, leaving the coordination site at the metal atoms vacant. Therefore HKUST-1 has a high capacity for gas adsorption. The HKUST-1 structure (M = Mo, Zn, Fe, Cr) may be created using a range of metal cations, and the discovery of M2(dobdc) implies that metals are a significant factor to take into account when adjusting material attributes.

For metal ions having exposed coordination sites, adsorption is influenced by the metal coordination site charge density. [69] MOF-74 (M_2(DOT)) is another well-researched family of MOFs with exposed metal cation sites. Its highly dense unsaturated coordinate metal sites contributes to its strong CO_2 adsorption capabilities at 296 K and 1 bar. In tests, Mg-MOF-74 effectively separates CO_2 (20%) from CH_4 (80%), demonstrating favorable performance from both a thermodynamic and kinetic perspective. The metal-organic framework's maximum low-pressure volumetric and gravimetric adsorption capacity for carbon dioxide is really represented by the value of Mg2 (dobdc). This demonstrates the enormous potential of metalorganic framework materials for gas separation applications. [66]

CHAPTER 2   LITERATURE REVIEW

(Bahmanzadegan et al., 2023). The goal of this work is to maximize the CO_2 adsorption capacity of Cu-BTC, which is made from kaolin, by using structural alterations obtained via impregnation with diethanolamine (DEA) and tetraethylenepentamine (TEPA). Using a test apparatus, the modified Cu-BTCs' adsorption capability was evaluated at various pressures, temperatures, and amine concentrations. We find that the optimal working conditions for the DEA adsorbent are 25.270 °C, 8.870 bar of pressure, and 11.112 weight percent of amine, and that its ideal adsorption capacity is 579.468 mg/g. [70]

(Hedayati et al., 2023). The work aimed to explore different CO_2 adsorbents for temperature-pressure swing adsorption-based post-combustion capture of CO_2. Activated carbon (AC), clinoptilolite, three synthetic Cu-BTCs and a metal organic framework (MOF-MIL-53) are among these adsorbents. Adsorbents were tested with several gas mixes that mimicked a combustion exit stream (O_2/CO /N_2/CO_2) to assess their performance and adsorption capacity of CO_2 throughout subsequent adsorption–desorption cycles at various circumstances (1–6 bar and 120–180°C). Excellent adsorption capacity of 4.3 mmol CO_2/g Cu-BTC and highly stable performance across multiple cycles were demonstrated by the Cu-BTC. [71]

(Cavallo et al., 2023). Both naturally occurring Clinoptilolite (Clino) and Cu-BTC, were studied separately or following an ion-exchange method, and their CO_2 adsorption performances were compared to evaluate their potential use as solid adsorbents for Carbon Capture and Storage (CCS). While natural clino has intriguing CO_2 adsorption performances at medium-high temperatures (it is the most performant material at 423 K), Cu-BTCs have superior CO_2 adsorption capacities at lower temperatures. [72]

(Cavenati et al., 2004). This study examined the adsorption of nitrogen and carbon dioxide on samples of Cu-BTC and activated carbon. Cu-BTC was found to be more appropriate for carbon dioxide separation due to its higher heat of adsorption and greater selectivity for carbon dioxide over nitrogen. Keeping in mind a few Cu-BTC limitations, such as its hydrophilic nature, which will maintain its adsorption capacity. [73]

(Loiseau et al., 2006) This study shows that at room temperature, metal-organic frameworks (MOFs) effectively store CO_2. Gravimetric CO_2 isotherms are provided up to 42 bar for MOF-505, MOF-2, $Cu_3(BTC)_2$ and MOF-177. With the exception of those based on $Zn_4O(O_2C)_6$ clusters, all MOFs exhibit Type I isotherms; the latter have a sigmoidal isotherm that is step-characterized. Varying pressures during isotherm stages are caused by increased pore size, which suggests gas separations. The CO_2 attraction is increased by the amine functionality in IRMOF-3 pores. A material's surface area determines its capabilities. With a capacity of 33.5 mmol/g, MOF-177 (320 cm^3(STP)/cm^3, 147 weight percent) is the porous material with the largest CO_2 capacity. [74]

(Demessence et al., 2009a) According to the report, metal-organic frameworks porous hybrid substance composed of metal ions and organic bridges—have demonstrated considerable promise for a number of applications. Changes to pore properties and topologies of metal-organic frameworks are simple because to the large variety of building components available. It is still difficult to create frameworks that are suited to certain applications, even with extensive research. In this study, a large surface area metal-organic framework called NU-100 was constructed and precisely described by the use of computer modeling. A material that matched the calculated structure was produced by experimental synthesis. At 6,143 $m^2\,g^{-1}$ the material's BET surface area was high. Furthermore, sorption studies demonstrated the material's capacity to store carbon dioxide (2,315 mg g^{-1}) and hydrogen (164 mg g^{-1}), both of which are crucial for clean energy and mitigating climate change. These results agree with modeling expectations. [75]

(Sumida et al., 2010) A novel aluminum trimesate, Al MOF, was synthesized hydrothermally at 210 degrees Celsius for a duration of 24 hours, as stated in the study. Trimesic acid was dissolved in water during the production. Hexagonal crystals are grown for single-crystal XRD using tetraethyl orthosilicate (TEOS), hydrofluoric acid (HF), and trimethyl BTC. The three-dimensional structure of MIL-96 is composed of infinite chains of $AlO_4(OH)_2$ and $AlO_2(OH)_4$ octahedra with solitary trinuclear mu-oxo-bridged aluminum clusters. The 18-membered rings in this honeycomb lattice pattern are used. Trimesate species join the two aluminum groups to form wavy chains of aluminum octahedra. These chains are joined in a flawless cis-cis-trans

arrangement by mu-hydroxo linkages. Three types of cages are used in the 3D fabrication of MIL-96. Free water molecules are present in two holes at coordinates 0 0 0 and 2/3 1/3 1/4, with estimated capacities of 417 and 635A, respectively. The crystal structure is consistent with the elemental, thermal, and solid-state NMR characterisation. Four aluminum crystallographic sites are identified and analyzed using the 27Al 3QMAS technique. This chemical can absorb 1.95 mmol.g^{-1} CH_4 and 4.4 mmol g^{-1} CO_2 at room temperature at 10 bar pressure. Additionally, at 77 K and 3 bar of pressure, it adsorbs hydrogen with a weight percentage of 1.91%. [76]

(Demessence et al., 2009b) Using Cu-BTC in DMF at 100 °C, the study demonstrates that CuCl2·2H$_2$O interacts to produce the MOF. The structure resembling sodalite is comprised of square clusters $[Cu_4Cl]^{4+}$ connected by $BTTri^{3-}$, where each cluster has a DMF ligand facing a sizable pore. The structure exhibits remarkable thermal stability reaching 270°C. The framework was fully desolated at 180 °C to yield MOF. As indicated before, these sites were connected to ethylenediamine molecules to form 1-en, which has terminal alkylamine groups. Grafting lowers BET surface area from 1771 to 346 m^2/g, according to the N_2 adsorption isotherms. The complete and reversible absorption of 1.2 weight percent (wt%) at 1.2 bar is demonstrated by the hydrogen (H_2) adsorption data of substance 1 at 77 Kelvin (K). The carbon dioxide (CO_2) isotherm at 195 K absorbs 90% of the energy at 1 bar. [75]

(Sumida et al., 2010) Using high-throughput instrumentation, the study discovered that $FeCl_2$ interacts with H$_3$BTT·2HCl in a DMF/DMSO combination under a variety of circumstances to form Fe MOF. This compound forms an anionic 3,8-net structure consisting of square $[Fe_4Cl]^{7+}$ units connected by triangular BTT bridging ligands inside a porous framework. Mössbauer spectroscopy performed on a DMF-solvated material revealed that the high-spin Fe^{2+} ions that make up the framework have distinct local environments. The compound becomes microporous after being submerged in methanol and heated at 135 °C for 24 hours under decreased pressure. This process removes the majority of the solvent. Fe-BTT contains exposed Fe^{2+} coordination sites and a surface area of 2010 m^2 g^{-1} BET. Data on hydrogen adsorption at 77 K reveal a sharp rise in isotherm. The initial isosteric adsorption heat is 11.9 kJ mol1 at 100 bar and 298 K, which yields 1.1 wt% and 8.4 g L1 storage capacity. The

position with the strongest bond was found to be 2.17(5) Å from the Fe^{2+} cation in the framework. [76]

(Li et al., 2013) This study discovered that it is challenging to regulate the production of porous materials with already designed pore characteristics for specific uses, even with tremendous effort. Modern porous metal-organic materials, like frameworks and polyhedra, are readily fabricated and controlled to control their properties. This makes it possible to precisely customize their functionality through the creation of their molecular architectures. This study introduces and validates a carefully engineered cavity, dubbed a "single-molecule trap," that can collect CO_2 molecules through theoretical and experimental methods. Without forming chemical bonds, a single-molecule trap can enhance CO_2-host interactions, indicating that CO_2 could be captured by it. As molecular single-molecule traps for selectively adsorbing CO_2 over N_2 and CH_4, metal-organic polyhedra are investigated. When pre-made traps are included into MOF with good mass transfer, the selective adsorption of CO_2 is preserved.[77]

(Mallick et al., 2010) Based on these findings, Mg-MOF-1 [Mg(3,5-PDC)(H_2O), a rare Mg-based MOF, was created by solvothermal synthesis using DMF. A helical structure is formed by water molecules, achiral 3,5-pyridine dicarboxylates, and magnesium ions. As a result, parallel hexagonal tubes form a three-dimensional framework. The 0D counterpart [Mg(2,4-PDC)($H_2O)_3$] was examined structurally to demonstrate how slight modifications to the ligand design impact the structure's transition from 0D to 3D. The first chiral hexagonal magnesium metal-organic framework (Mg-MOF) derived from a non-chiral organic building block is described in this article. Magnesium (Mg) metal sites absorb hydrogen (H_2) preferentially at 0.8 weight percent at 77 Kelvin. Additionally, at 298 Kelvin, they absorb 0.7 millimoles per gram of CO_2, surpassing the rate of nitrogen adsorption at 1 atmosphere. The paper uses ab initio quantum chemistry to compute the adsorption energy and positions of hydrogen molecules.[78]

(Caskey et al., 2008) In this work, four microporous coordination polymers (MCPs) with various metal compositions but the same structure are shown. It is demonstrated that these MCPs can absorb CO_2 with exceptional efficiency at room temperature and low pressure. These specifications are only relevant to the capture of flue gas released

by power plants that burn coal. Among all the magnesium MOF that have been previously characterized, the material presented in this study is magnesium based and has the largest surface area. Furthermore, as demonstrated by its high heat of adsorption, this material shows an incredibly strong affinity to CO_2. According to this work, physisorptive materials can achieve capacities and affinities comparable to those of amine sorbents, but at far lower regeneration energy costs. [79]

(Duan et. al., 2018) In light of the increasing emissions of CO_2, especially from power plants, the authors stress the need for materials with an efficient ability to remove CO_2 after burning (CO_2/N_2 = 15/85). Under ambient circumstances (298 K, 1 atm), our Cu(II) MOF (FJI-H14) demonstrates remarkable base and acid stability and strong CO_2 absorption (171 cm^3 /cm^3), indicating its potential as a post-combustion CO_2 adsorbent. It's possible for several active sites to work together to control catalytic activity and boost CO_2 adsorption. [52]

(Kim et al., 2013) The researchers created MIL-125, a Ti MOF structure, and NH_2-MIL-125, its amine-functionalized counterpart, by heating it with a microwave and using solvothermal techniques. XRD, EA, TGA, SEM, UV-visible spectroscopy, and nitrogen adsorption-desorption studies were used to describe the materials. While NH_2-MIL-125 was stable in both water and heptane, MIL-125 was unstable in both. Adsorption of water vapor on NH_2-MIL-125 verified its hydrophilicity. NH_2-MIL-125 demonstrated a modest CO_2 adsorption capacity of 136 mg g^{-1} at 298 K. Its selectivity over N_2, however, exceeded 27:1. Furthermore, the heat of adsorption of NH_2-MIL-125 was lower compared to MIL-125. The adsorbent was perfectly regenerated by NH_2-MIL-125 following four cycles of CO_2 adsorption and desorption. This helium-flow process lasted for 550 minutes at 298 K. The catalytic characteristics of the materials were evaluated using the epichlorohydrin cycloaddition and the dibenzothiophene oxidative desulfurization.[80]

(Si et al., 2011) The amine-functionalized microporous MOF CAU-1 was constructed with a home-made technique and activated, as stated in the study. It exhibits significant selectivity toward N_2 and adsorption of CO_2. The CO_2 uptake capacity reaches 7.2 mmol g^{-1} at 1 atm pressure and 273 K. N_2 uptake was 0.37 and CH4 uptake was 1.34 mmol g^{-1} at 1 atm and 273 K. At 273 K, the CO_2 selectivity to N_2 was 101:1. In addition, at 77 Kelvin and 1 and 30 atmospheres, respectively, CAU-1 can absorb

2.0 and 4.0 weight percent hydrogen. CAU-1 was subjected to methanol adsorption testing using a quartz crystal microbalance. This MOF structure could function as a sensitive methanol sensor in direct methanol fuel cells.[81]

(An et al., 2010) The structure and synthesis of bio-MOF-11 are described in detail in this study. Pyrimidine and adeninate amino groups embellish the framework. A study was carried out to ascertain the porosity of this substance and to evaluate its capacity to absorb CO_2 and H_2. With a heat of adsorption of about 45 kJ/mol, Bio-MOF-11 shows a notable CO_2 adsorption capacity. Additionally, at 273 K, it has higher CO_2 adsorption of about 6 mmol/g. Furthermore, it displays excellent selectivity for CO_2 over N_2 at 273 K (ratio: 81:1) and 298 K (ratio: 75:1). [82]

(Qin et al., 2012) ZMOF is a new kind of metal-organic framework that resembles zeolites and has a sodalite topology. IFMC-1 was synthesized using L (4,5-di(1H-tetrazol-5-yl)-2H-1,2,3-triazole), an N-rich aromatic ligand devoid of an NH_2 group. This substance preferentially and effectively absorbs CO_2 over N_2. It also does a good job of delivering medications. [83]

(Maity et al., 2018) We created a highly porous, thermally stable, interpenetrated Cu-II MOF that has the ability to function as a heterogeneous catalyst. A metal cluster (Cu24) with a cuboctahedron shape serves as the secondary building unit (SBU) of the Cu II-MOF. These massive cluster-containing nets have a remarkable capacity to store H_2 (313 cm^3 /g at 1 bar and 77 K) and trap CO_2 (159 cm^3/g at 1 bar and 273 K) because of their twofold interpenetration, which results in a high density of open metal sites. [84]

(Lin et al., 2012) The MOF MIL-88A is produced when $CuCl_2 \cdot 2H_2O$ reacts with H_3BTTri in DMF at 100 °C. The framework's sodalite-type structure is made up of BTTri3-linked $[Cu_4Cl]^{7+}$ square clusters, where each Cu II center has a terminal DMF ligand pointing inside a sizable pore. The framework has remarkable chemical stability in acidic media, boiling water, and air, in addition to its strong thermal stability up to 270 °C. After the guest solvent and attached DMF molecules were exchanged for methanol to yield 1-MeOH, the framework was completely dissolved at 180 °C to produce $H_3[(Cu_4Cl)_3(BTTri)_8]$, which had exposed Cu II sites on its surface. Ethylediamine molecules were grafted onto these sites in accordance with a previously described process to produce 1-en, which has terminal alkylamine groups.

The alkylamine modified framework 1-en shows superior CO_2/N_2 selectivity at all observed pressures and greater CO_2 uptake at 298 K and pressures up to around 0.1 bar when compared to 1. The strongest documented chemisorption interaction for a MOF to date, this interaction suggests the possible use of frameworks with alkylamine attached flue gas streams. [85]

(Yan et al., 2017) Carbon dioxide sorption isotherms were measured on Cu-BTC functionalized graphite oxide (GO) additive at three near-ambient temperatures in the pressure ranging to 1.5 bar. They are thought to be significant factors affecting how materials for CO_2 collecting are actually used in the real world. The results indicate a significant increase in the CO_2 adsorbent capacity of the composites when compared to the original Cu-BTC MOF. Of all the samples that were assessed, the combination of Cu-BTC and functionalized graphite oxide with the highest content of N (MOF/GO-U3) is the one that performs the best. On its surface, 13.41 mmol/g of CO_2 were adsorbed at ambient temperature and 1.5 bar. It was shown that CO_2 was more selective than CH4 at adsorption. The selectivity for carbon dioxide sorption over nitrogen are determined by the MOF phase properties. The composite materials exhibit a high measure of surface homogeneity and a comparatively lower heat of carbon dioxide adsorption, allowing for complete regeneration and efficient use of energy in multicycle adsorption. [59]

(Yu et al., 2017) The goal of this study was to increase the capacity for CO_2 capture using a volumetric approach (CO_2 adsorption capacity in cm^3 per cm^3 sorbent), which is essential for CO_2 capture applications in real-world settings. In order to do this, the benefits of metal–organic frameworks (MOFs) ($Cu_3(BTC)_2$) will be included into the structural characteristics of hierarchical porous carbon monoliths (HCM) in order to optimize them. In the monolithic HCM matrix, $Cu_3(BTC)_2$ was generated in situ, and further impregnation and crystallization processes resulted in the formation of HCM-$Cu_3(BTC)_2$ composites. On a volumetric basis, the resultant HCM-$Cu_3(BTC)_2$ composites show significant CO_2 uptake of 22.7 $cm^3.cm^{-3}$. They preserve the monolith shape and shows quite unique hybrid structural characteristics of $Cu_3(BTC)_2$ and HCM. This number is about twice as high as the initial adoption of HCM. It is possible to simply release CO_2 by pressing an argon flow. [60]

CHAPTER 3   EXPERIMENTATION

This section covers the experimental work that was done in lab and includes a variety of appropriate synthesis techniques that were used to synthesize the desired product. The synthesis methods needed to create the intended MOF are covered in this section. The preparation of Cu-BTC and its amine modifications will be described in this section.

3.1   Synthesis of Cu-BTC

According to Liu et al. [20], the hydrothermal process used to create the Cu-BTC MOFs was a modification of earlier research by Rowsell and Yaghi [21]. After dissolving 1.50 g of 1,3,5-benzenetricarboxylic acid in 45 mL of a 1:1 mixture of DMF and ethanol and 3.11 g of copper(II)nitrate trihydrate in 22.5 mL of deionized water, two solutions were combined and agitated for 10 minutes at room temperature. They were then put into a 100 mL Teflon-lined stainless-steel autoclave and cooked for 10 hours at 373 K. After filtration, the blue microcrystals that were produced were separated and repeatedly cleaned with methanol. The resulting materials were employed in additional studies after being vacuum-dried for an entire night at 333 K. [86]

Table 3.1 Materials used in Synthesis of Cu-BTC

Sr. No.	Chemical	Molecular Weight	Quantity
1	Benzene Tricarboxylic Acid	210.14 g/mol	1.5 g
2	Ethanol	46.068 g/mol	22.5 ml
3	Dimethylformamide	73.09 g/mol	22.5 ml
4	Copper Nitrate Trihydrate	241.60 g/mol	3.11 g
5	DI Water	1802 g/mol	22.5 ml

Furthermore, copper MOF is functionalized with three different amines. The introduced organic amines included HMTA, melamine and DPA and products were named HMTA-Cu-BTC, Mel-Cu-BTC and DPA-Cu-BTC.

3.2   Synthesis of HMTA-Cu-BTC

An illustration of hydrothermal method for the synthesis of HMTA-Cu-BTC is given here. $Cu(NO_3)_2 \cdot 6H_2O$ (1 mmol, 296mg), trimesic acid (1 mmol, 166 mg), and an equimolar ratio of 1:1:1, 140 mg of HMTA (1 mmol) was added to in 10 mL DMF using a 100 mL beaker to create HMTA-Cu-BTC. After 30 minutes of ultrasonication at 25 °C, the contents were moved to a 23 mL Teflon vial in a steel Parr tank. To produce greenish-blue crystals, the Parr jar was sealed and heated for 24 hours at 110 °C in an oven. Decanting the reaction mixture resulted in three rounds of washing it with 5mL DMF and then three times with 5mL THF. Blue crystals resulted from this. Prior to additional examination, the sample was activated for 12 hours at 130 °C in a vacuum oven. [87]

Table 3.2 Materials used in Synthesis of HMTA-Cu-BTC

Sr. No.	Chemical	Molecular Weight	Quantity
1	Hexamethylenetetramine	140.189 g/mol	140 mg
2	Copper Nitrate Trihydrate	241.60 g/mol	296 mg
3	Terephthalic Acid	166.13 g/mol	22.5 ml
4	Dimethylformamide	73.09 g/mol	10 ml

3.3   Synthesis of Mel-Cu-BTC

An illustration of hydrothermal method for the synthesis of Mel-Cu-BTC is given here. $Cu(NO_3)_2 \cdot 6H_2O$ (1 mmol, 296mg), trimesic acid (1 mmol, 166 mg) and in an equimolar ratio of 1:1:1, 126 mg of melamine (1 mmol) was added to in 10 mL DMF using a 100 mL beaker to create Mel-Cu-BTC. After 30 minutes of ultrasonication at 25 °C, the contents were moved to a 23 mL Teflon vial in a steel Parr tank. To produce greenish-blue crystals, the Parr jar was sealed and heated for 24 hours at 110 °C in an oven. Decanting the reaction mixture resulted in three rounds of washing it with 5mL DMF and then three times with 5mL THF. Blue crystals resulted from this. Prior to additional examination, the sample was activated for 12 hours at 130 °C in a vacuum oven. [87]

Table 3.3 Materials used in Synthesis of Mel- Cu-BTC

Sr. No.	Chemical	Molecular Weight	Quantity
1	Melamine	126.12 g/mol	126 mg
2	Copper Nitrate Trihydrate	241.60 g/mol	296 mg
3	Terephthalic Acid	166.13 g/mol	22.5 ml
4	Dimethylformamide	73.09 g/mol	10 ml

3.4   Synthesis of DPA-Cu-BTC

An illustration of hydrothermal method for the synthesis of DPA-Cu-BDC is given here $Cu(NO_3)_2 \cdot 6H_2O$ (1 mmol, 296mg), trimesic acid (1 mmol, 166 mg) and diphenylamine (169 mg, 1 mmol) were dissolved in 10 mL DMF in a 50 mL beaker in equimolar ratios (1:1:1) to create DPA-Cu-BTC.   After 30 minutes of ultrasonication at 25 °C, the contents were moved to a 23 mL Teflon vial in a steel Parr tank. To produce greenish-blue crystals, the Parr jar was sealed and heated for 24 hours at 110 °C in an oven. Decanting the reaction mixture resulted in three rounds of washing it with 5mL DMF and then three times with 5mL THF. Blue crystals resulted from this. Prior to additional examination, the sample was activated for 12 hours at 130 °C in a vacuum oven.[87]

Table 3.4 Materials used in Synthesis of DPA-Cu-BTC

Sr. No.	Chemical	Molecular Weight	Quantity
1	Diphenylamine	169.23 g/mol	169 mg
2	Copper Nitrate Trihydrate	241.60 g/mol	296 mg
3	Terephthalic Acid	166.13 g/mol	22.5 ml
4	Dimethylformamide	73.09 g/mol	10 ml

CHAPTER 4   CHARACTERIZATION TECHNIQUES

4.1   Instrumentation and measurements

The JEOL JSM-6490A (Tokyo, Japan) SEM was used to examine the morphological investigations of the materials. Using X-ray diffraction (XRD) on Siemens D5005 STOE & Cie GmbH (Darmstadt, Germany) at an angle (2θ) between 10o and 80o, the structural data was examined. Utilizing dried powder samples and potassium bromide pellets, the PerkinElmer SpectrumTM100 spectrophotometer was used to investigate the FTIR analysis.

4.2   Scanning Electron Microscopy (SEM)

4.2.1   Overview

SEM, or scanning electron microscopy, creates high-resolution images by employing a raster scan pattern to apply a high-energy electron beam to a sample's surface., is the most widely used method for characterizing materials. The image that is produced when the electrons interact with the sample's surface provides details about the sample, including its chemical composition and surface topography.

4.2.2   Working Principle:

In order to produce SEM images, electrons must be produced in an electron cannon. Typically, this is done by heating a thin tungsten filament in the shape of a V to produce electron emissions; this is known as a thermionic cathode. An anode is the target of the electrons that are produced. A voltage differential is applied between the anode and the thermionic cathode, with the anode being linked to a high voltage source's positive pole and the cathode to its negative pole. The accelerating voltage, which ranges from 0.2 to 40 keV, is the voltage differential that determines the electron energy and wavelength in the beam. [88]

The electrons (referred to as incident primary electrons) are accelerated by the strong electric field between the anode and the cathode to strike the sample. This causes a variety of emissions to be released from the sample's surface, including augur

electrons, secondary electrons with energy less than 50 eV, backscattered electrons with kinetic energies almost equal to those of the incident beam between 50 eV, and characteristic x-rays produced by the de-excitation of atoms by releasing the excess energy. Specific to the element from which it was produced, X-ray energy can be used to determine the sample chemical composition. [89]
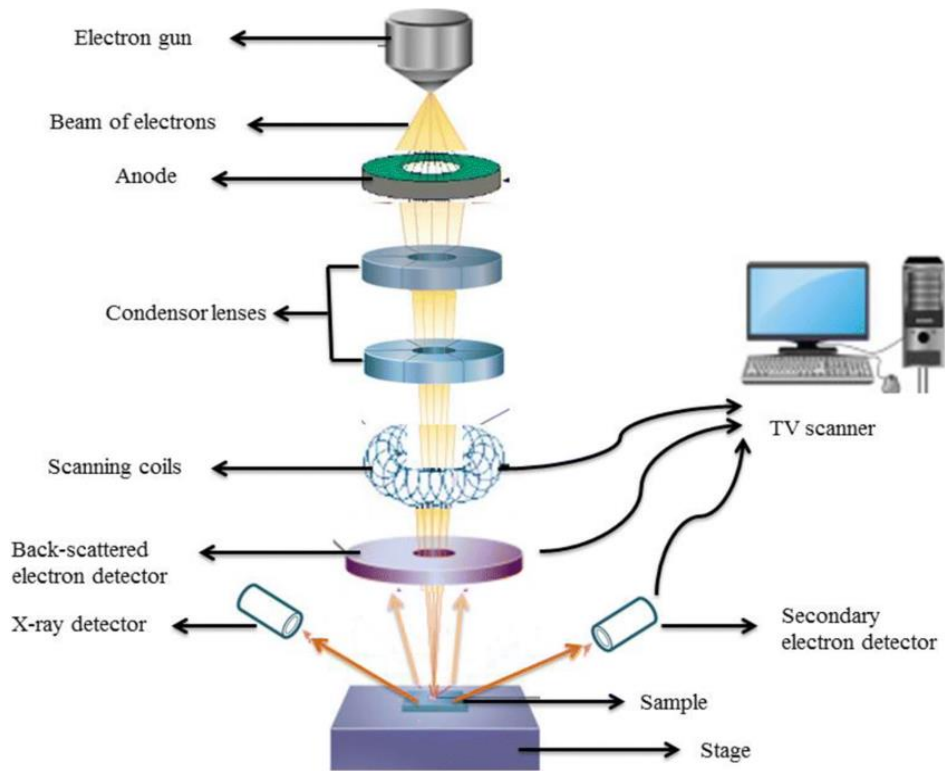
Figure 4.1 Schematic diagram of SEM [90]

Because they are able to display the sample's morphology and topography, secondary electrons are useful in SEM imaging. Once the incident primary electrons hit a sample's surface, the surface's electrons start to move. These loose electrons are known as secondary electrons, and a secondary electron detector (SE detector) connected to a positively biased grid may gather them. The signals produced by the SE detector can then be amplified, decoded, and combined to create an image. [91], [92]

4.2.3   Sample Preparation

Because the sample must be conductive, which may be accomplished by coating the sample with gold using a sputter coater, preparing the sample for SEM analysis is rather simple.

4.3 X-Ray Diffraction (XRD)

4.3.1 Overview

A potent non-destructive method for characterizing materials using x-ray radiation is X-ray diffraction. X-rays are electromagnetic radiations that resemble light identically, but they have a much shorter wavelength—roughly 1Å—and a high energy. The discovery that crystalline materials function as three-dimensional diffraction gratings at x-ray wavelengths comparable to the interplanar spacing in a crystal lattice was made in 1912 by German physicist Max von Laue and colleagues. [93]

The structural characteristics of the material's existing crystalline phases are determined using X-ray diffraction (XRD). It's also employed in the assessment of microstructure examination of the average particle size, sample purity, unit cell dimensions, film thickness, and polycrystalline and amorphous material properties.

4.3.2 Working Principle:

The sample to be analyzed is exposed to a beam of X-rays. Just like a physicist, it's fascinating to observe how many materials consist of tiny crystals with atoms arranged in a precise pattern, where each atom has a nucleus and electrons swirling around it. When x-rays interact with an atom, the electrons start to oscillate due to the influence of the incoming x-rays. As a result, they emit secondary x-rays with the same energy as the incident x-rays. When x-rays interact with each other, the emission can experience either constructive or destructive interference. When the waves are in sync, the signal gets a boost, resulting in constructive interference. [94] On the other hand, when the waves are out of sync, the signal gets wiped out, leading to destructive interference.

Just as a physicist would explain, the atoms in a crystal are arranged in a repeating pattern, creating distinct planes that are evenly spaced apart. When atomic planes are exposed to an x-ray beam, the evenly distributed atoms cause x-rays to scatter. When certain angles are just right, the scattered waves come together in a way that greatly amplifies the emitted signals. This phenomenon is commonly referred to as

diffraction. The detector captures the diffracted x-rays and presents the data in the form of a graph.
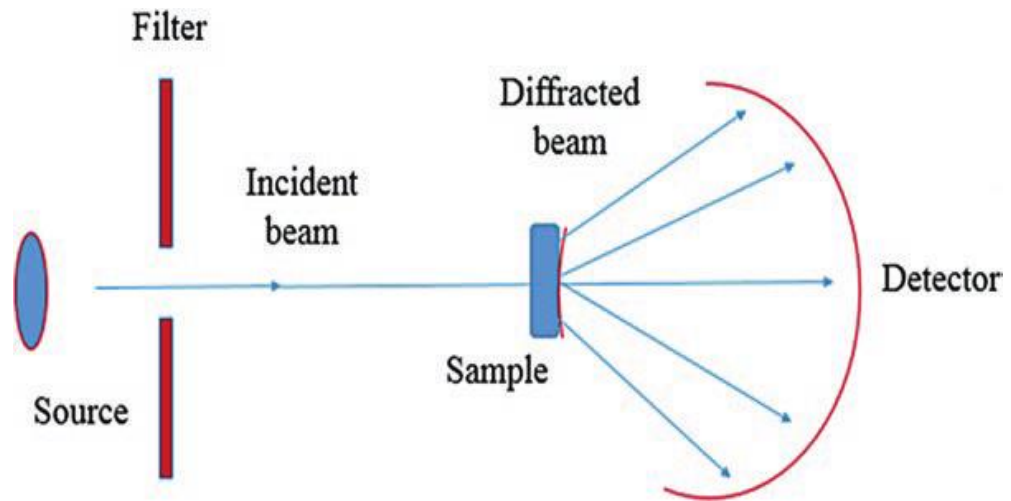
Figure 4.2 Schematic representation of X-ray diffraction
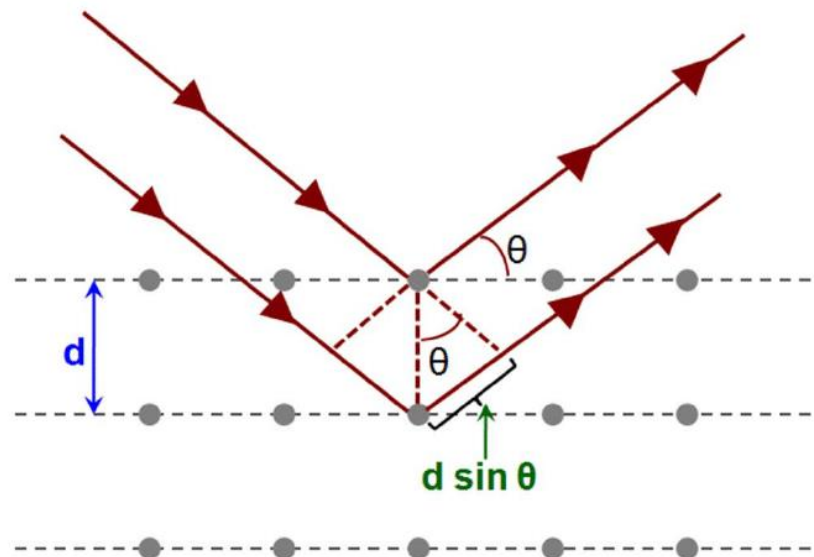
Figure 4.3 Schematic representation of a Bragg's law

The x-rays diffracted from crystal is described by the equation known as Bragg's law: [95], [96]

$$n\lambda = 2d\sin\theta$$

In this context, n represents the order of reflection, λ represents the wavelength, d represents the interplanar spacing of the crystal lattice planes that is responsible for a specific diffracted beam, and θ represents the angle between the incident beam and lattice planes.

4.4 Fourier Transform Infra-Red (FT-IR) Spectroscopy

4.4.1 Overview:

Understanding the interaction between infrared radiation and matter is crucial in the field of infrared spectroscopy. With a wavelength longer than visible light, infrared radiation is a type of electromagnetic radiation. FTIR is a highly popular method in the field of vibrational spectroscopy for determining the functional groups and chemical bonds present. This particular type of infrared spectroscopy utilizes the Using the Fourier transform approach, one may concurrently acquire an infrared spectrum across a large range of wavenumbers. It different from the dispersive method, where signals are collected to create a spectrum at each wavenumber individually. Currently, the dispersive method has been largely replaced by FTIR due to its significantly higher signal-to-noise ratio.

IR radiation is generated by a light source and aimed at the sample, causing the sample to absorb certain amounts of the passing light while reflecting the rest. The remaining light is transmitted, carrying the molecular information, and collected by a detector to generate an electronic signal. [97], [98]

4.4.2 Working Principle:

The Michelson interferometer plays a crucial role in the Fourier transform infrared spectrometer. As shown in Figure 4.4, the IR beam emitted by the source passes through the interferometer and is directed towards a beam splitter for measurement. The beam is split and directed towards a stationary mirror and a mirror in motion. Following that, the beam is combined once again and aimed towards the material being studied. All the wavelengths' spectral information is acquired simultaneously. By manipulating the optical path lengths, the light interference between the two split beams is generated. Both split beams have the same optical pathways. There is no path change since the moving mirror is positioned the same distance from the beam splitter as the fixed mirror. By moving the mirror away from the beam-splitter, a shift in the optical path difference (δ) can be achieved. [98], [99] The two beams will create alternating patterns of destructive and constructive interference, resulting in a

continuous variation of the δ value. Then completely destructive interference occurs. The value of δ changes when the moving mirror's location changes.

Constructive interference occurs when;

$$\delta = n\lambda,$$

whereas when

$$\delta = (1/2+n)\,\lambda$$
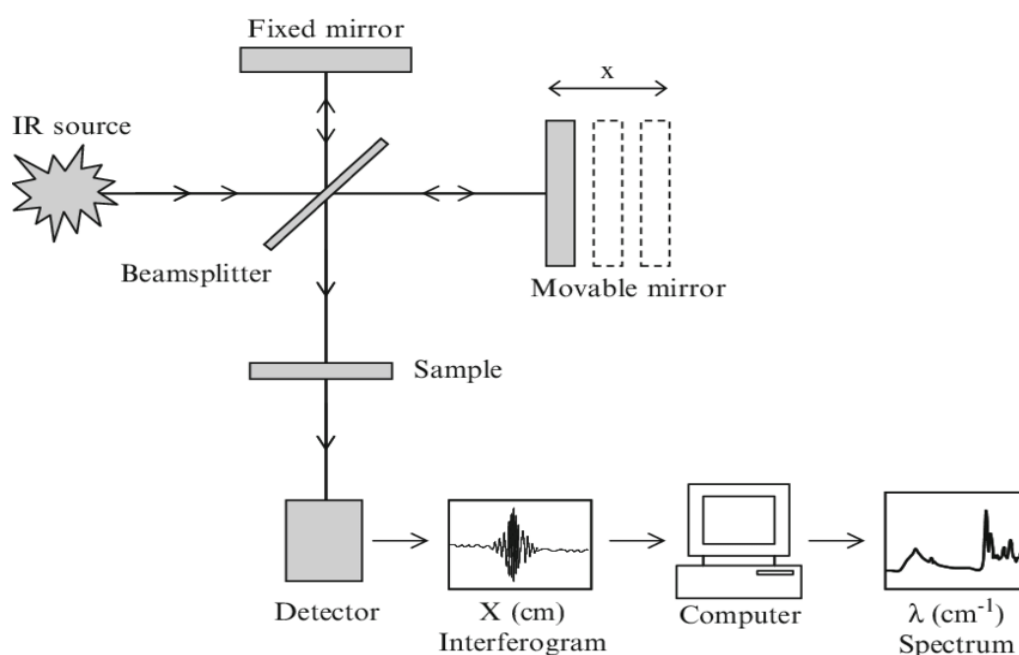
Figure 4.4 Illustration of working of FTIR spectroscopy

An interferogram is a graph that shows the intensity of light interference as it varies with the optical path difference. To analyze the infrared spectrum, we need to perform a Fourier transformation on the interferogram, which is a graph of light intensity plotted against wavenumber. The FTIR detector receives interferogram signals and then sends them to a sample or reflects them from a sample. The detector's interferogram does not capture an infrared spectrum. Using the fast Fourier transform (FFT) algorithm, a computer equipped with FTIR technology is able to generate the infrared spectrum.

The FTIR spectrum can be likened to a chemical fingerprint. It has the ability to identify and confirm both familiar and unfamiliar samples, while also providing insights into new ones. Especially valuable in the chemical and manufacturing sectors, as well as in research and development. [99]

CHAPTER 5   RESULTS AND DISSCUSIONS

5.1   Characterization Techniques

Among the spectroscopies are X-ray diffraction (XRD), scanning electron microscopy (SEM), BET analysis, particle size analyzer, and Fourier transform infrared (FTIR). With the help of these characterization techniques, we examined our samples in order to gain a better knowledge of their traits, composition, and morphology. The XRD and SEM techniques were used to study the formation and shape of the samples; the FTIR technique was used to identify the functional groups and types of bonds present in our specimens.

For the CO_2 adsorption analysis, different pressure conditions were employed. Every sample has undergone CO_2 analysis. Below are the specific findings from the CO_2 capture research and the methodologies used to characterize each sample.

5.1.1   Equipment

The JEOL JSM-6490A (Tokyo, Japan) SEM was used to examine the morphological investigations of the materials. Using X-ray diffraction (XRD) on Seimens D5005 STOE & Cie GmbH (Darmstadt, Germany) at an angle (2θ) between 10o and 80o, the structural data was examined.

Utilizing dried powder samples and potassium bromide pellets, the PerkinElmer SpectrumTM100 spectrophotometer was used to investigate the Fourier Transform Infra-Red analysis.

5.2   Fourier Transform Infra-Red (FT-IR) Spectroscopy

The different functional groups and bond types present in the samples are shown by the FTIR analysis results. Before doing an FTIR analysis, we pellet our samples. We placed pallets inside the FTIR. The outcome of the FTIR analysis is a spectrogram.

This displays a graph with wave-number in cm^{-1} and transmittance in percentage between 4000 and 400 cm^{-1}. Figure 5.1 displays the FTIR spectrum of Cu-BTC and its amine modifications.
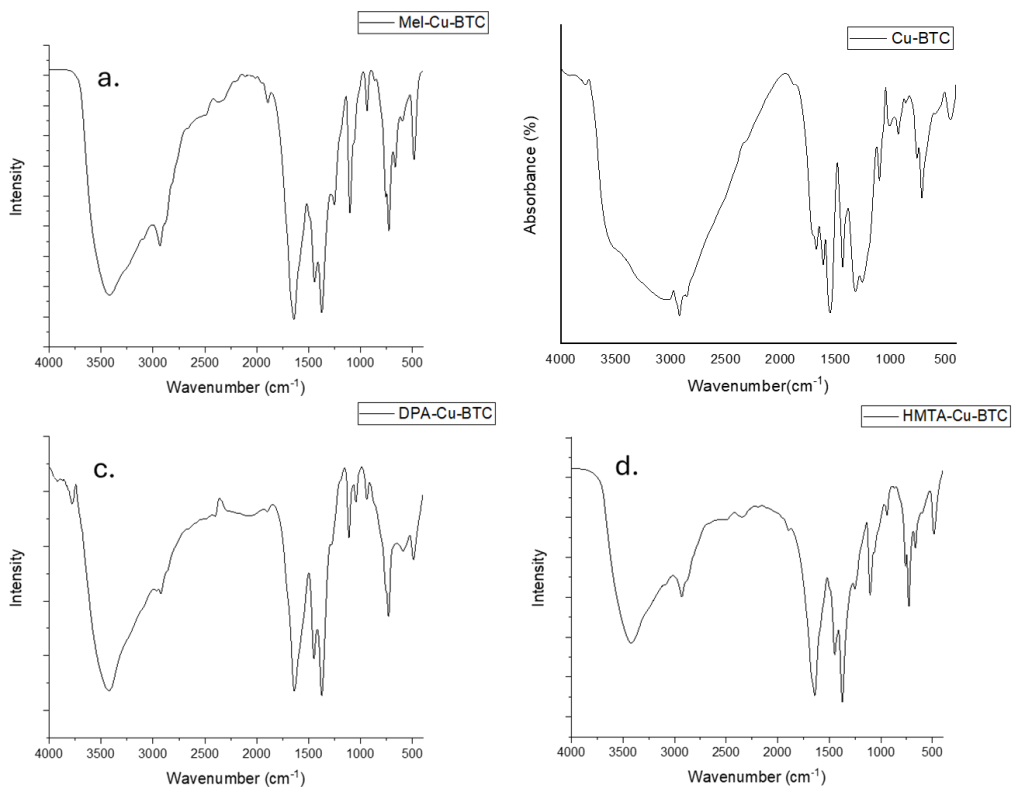
Figure 5.1 FTIR spectrum of (a). Mel-Cu-BTC, (b) Cu-BTC (c)DPA-Cu-BTC and (d) HMTA-Cu-BTC
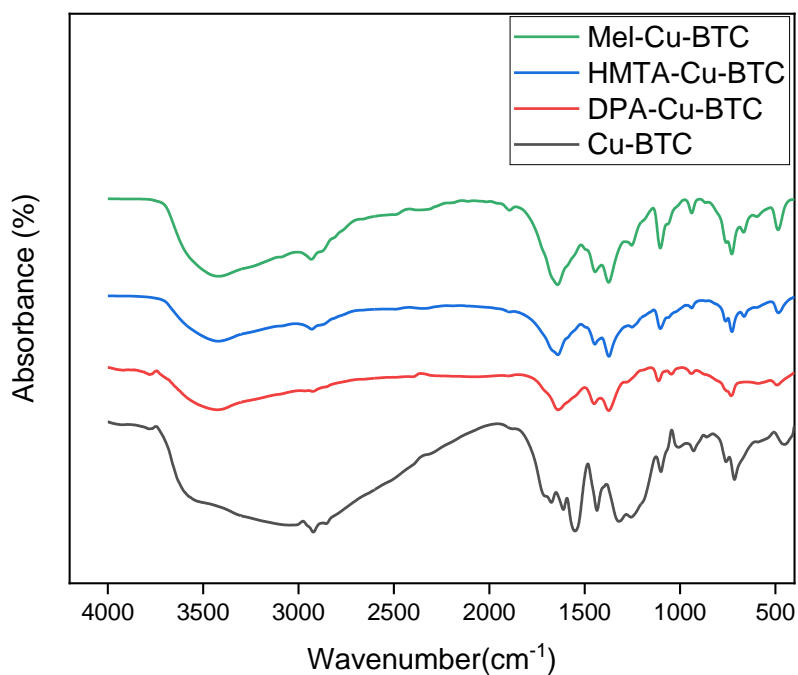
Figure 5.2 Comparison of FTIR spectrum of Cu-BTC and amine modifications.

Similar IR adsorption peaks are shown in figure 5.2 for the Cu-BTC and amine-modified samples, demonstrating how little the addition of amine alters the chemical structure. The attachment of Cu to the benzene ring of BTC is responsible for the peaks at 729 and 760 cm^{-1}. The C-O-Cu bonds' stretching causes the bands at 940 and 1110 cm-1 to show up. The asymmetric and symmetric vibrations of carboxylate groups are responsible for the bands at 1368, 1452, and 1640 cm^{-1}. A wide band at 3000–3600 cm^{-1} corresponds to the OH group's stretching vibrations, which show the existence of adsorbed water. [100], [101], [102]

5.3   X-Ray Diffraction

The crystalline adsorbent was subjected to XRD analysis in order to identify its phase and determine its composition within the 2θ range of 0° to 60°. XRD analysis was used to confirm the nature, planar structure, materials, and functionality.
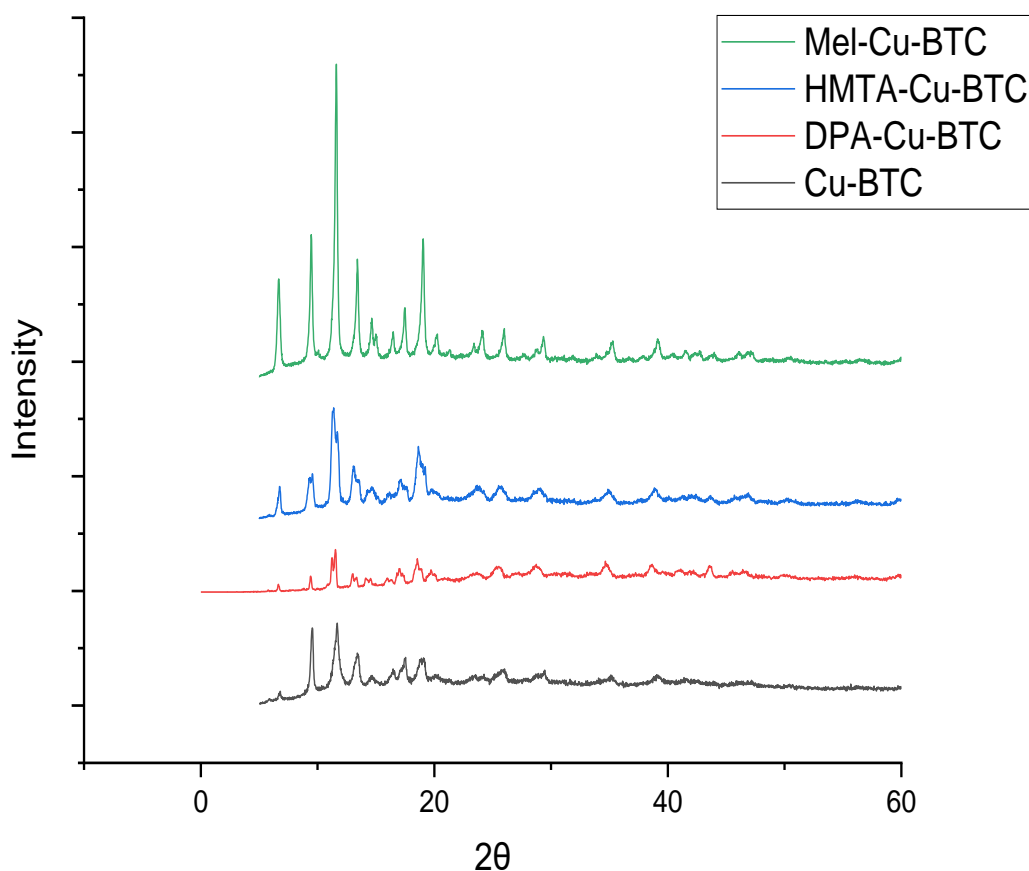
Figure 5.3 XRD analysis of Cu-BTC
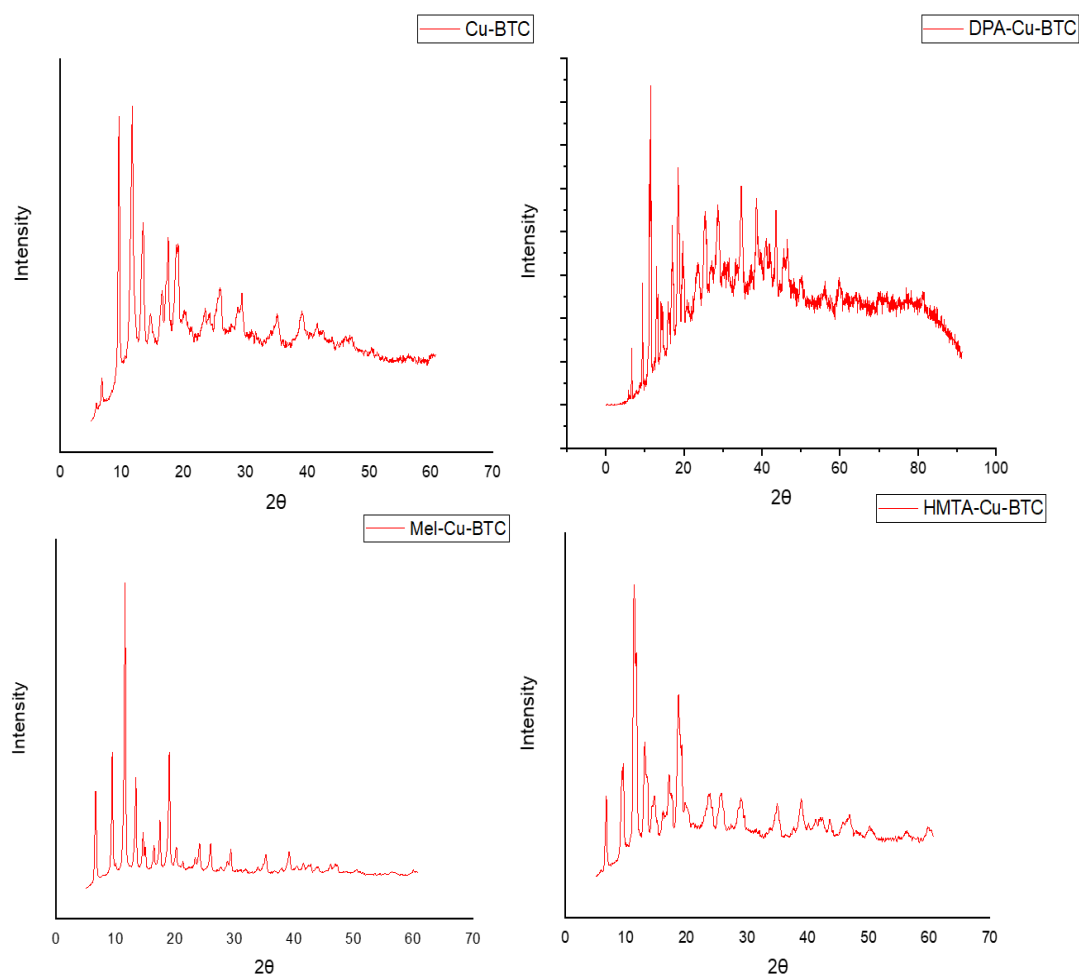
Figure 5.4 XRD analysis of Cu-BTC, DPA- Cu-BTC, Mel- Cu-BTC and HMTA- Cu-BTC

The first step in determining the purity and type of MOF is usually XRD. The crystal phase of the produced samples was identified by XRD examination. robust peaks that are in line with previously published research, such as the peaks at $2\theta = 9.6°$, $11.6°$, $13.4°$, $16.5°$, $17.5°$, and $19.0°$. The hkl values of (2 0 0), (2 2 0), (2 2 2), (4 0 0), (4 2 2), (3 3 3) and (4 4 0) correspond to these peaks. The effective synthesis of Cu-BTC was mentioned here. Following the addition of amines, the locations of the peaks were quite similar to those of the parent Cu-BTC, but the intensities varied, indicating a shift in the crystal sizes or a breakdown in the structure of the amine-modified MOFs.[100], [101], [102] As per Su et al. [61] parent Cu-BTC has distinctive peaks at $2\theta = 6.9°$, $9.5°$, $11.6°$, $13.4°$, $17.5°$, and $19.0°$, these peaks can be seen in figure 5.4 as well.

5.4 Scanning Electron Microscopy (SEM)

SEM, or scanning electron microscopy, is used to analyze materials' morphology and structure. Prior to being examined under a SEM, the samples are dried under vacuum. The dry samples are then covered in gold and supported by the sputter coater to stop material charging. SEM pictures were obtained at various magnifications of 0.5μm, 1μm, and 5μm to get a comprehensive analysis of the crystal structure and morphology of MOF and its amine modifications.

Copper MOF and its amine modifications were given SEM descriptions; the morphology of each sample is covered below. The SEM photos display a wide range of distinct structures; some of the images do not display perfect geometry.

5.4.1 SEM analysis of Cu-BTC

Figure 5.5 shows multiple resolution SEM images of the crystals.
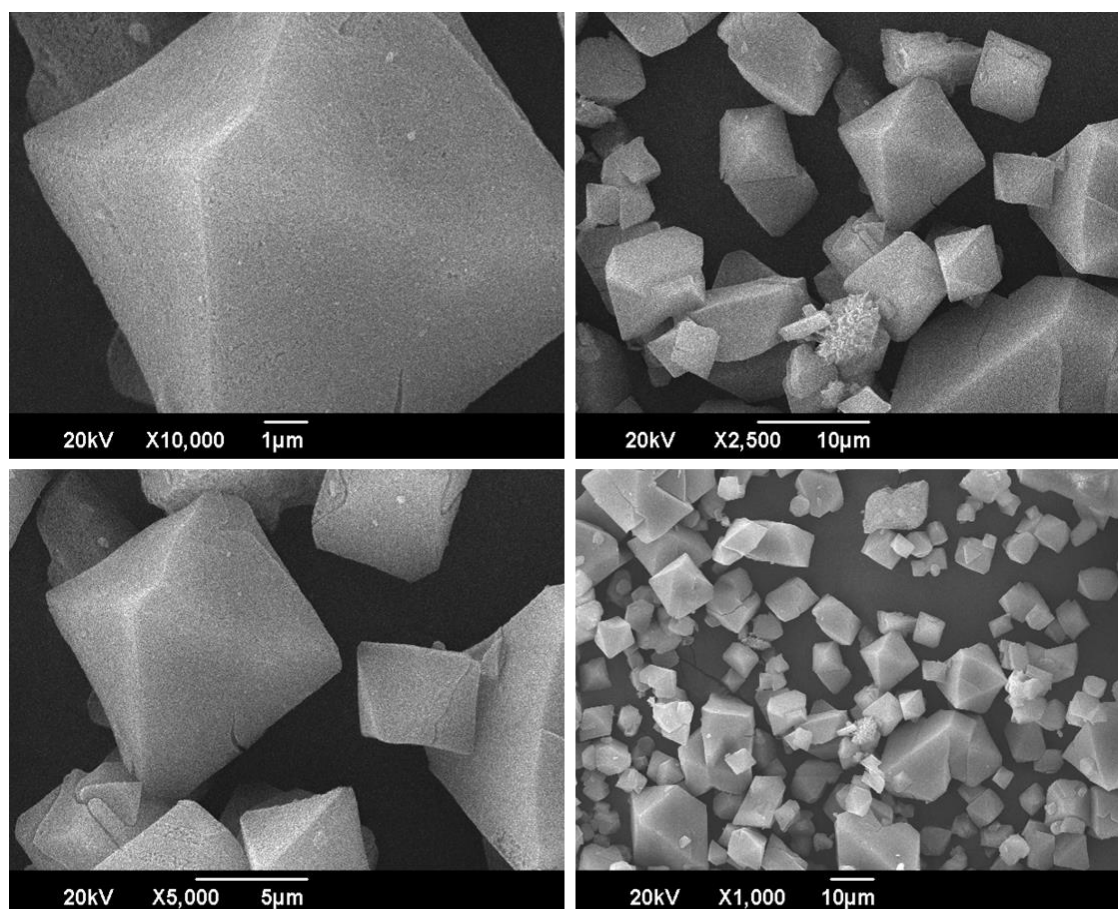
Figure 5.5 SEM images of Cu-BTC

These images further illustrate the structure of Cu-BTC. The MOF depicts a structure of octahedral or pyramid type shape which is already stated in the literature[100], [101], [102]. The synthesized MOF shows the characteristics octahedral structure while the crystal size of the MOF is not uniform. The high-resolution image of the MOF also shows the porous structure of the crystal, which is the major cause of the adsorption.

5.4.2 SEM analysis of DPA-Cu-BTC

Figure 5.6 represents the multiple resolution SEM images to illustrate the structure of DPA-Cu-BTC. The MOF depicts a structure of crystals with irregular shape. The synthesized MOF shows the characteristics octahedral structure while the crystal size of the MOF is not uniform. The high-resolution image of the MOF also shows the

porous structure of the crystal, which is the major cause of the adsorption. The size of the crystals reduced majorly compared to Cu-BTC, which is also depicted in the XRD peaks reduction.
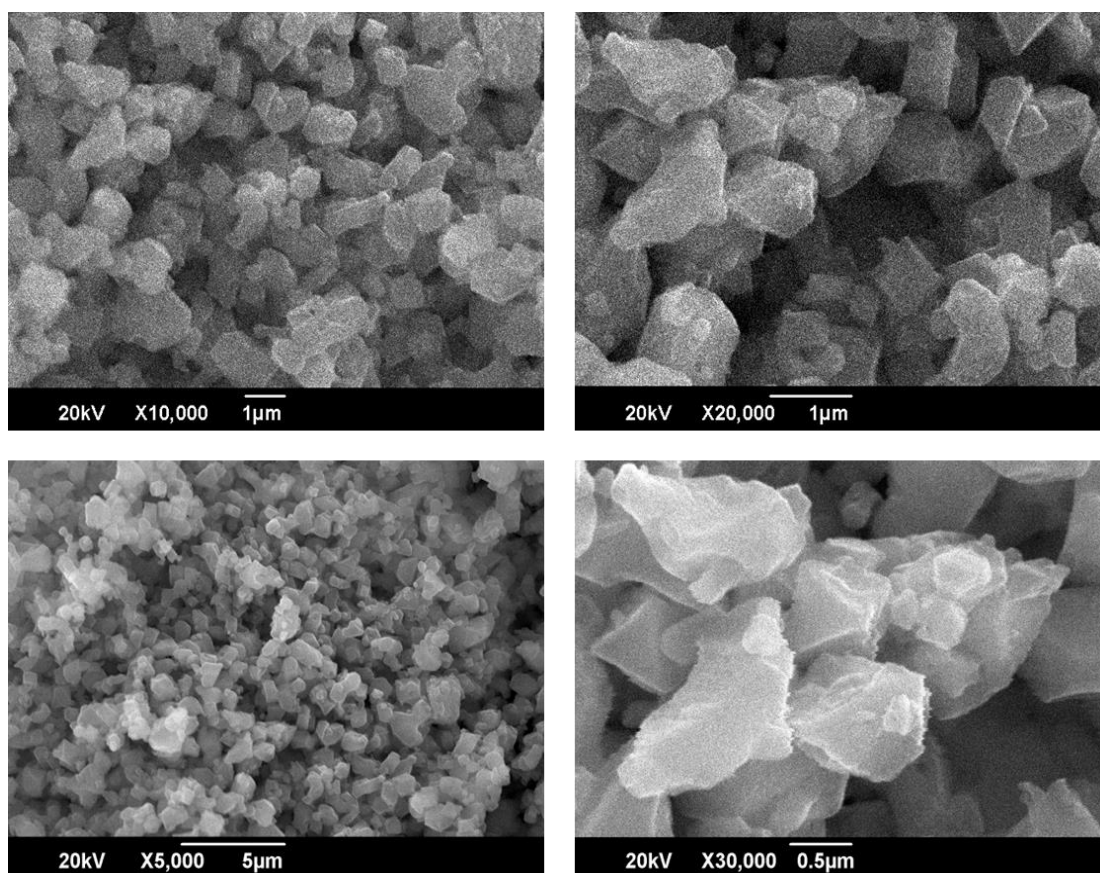
Figure 5.6 SEM images of DPA-Cu-BTC

54

5.4.3 SEM analysis of HMTA-Cu-BTC

Figure 5.7 represents the multiple resolution SEM images to illustrate the structure of HMTA-Cu-BTC. The MOF depicts a structure of crystals with irregular shape. The synthesized MOF shows the characteristics octahedral structure while the crystal size of the MOF is not uniform.

The high-resolution image of the MOF also shows the porous structure of the crystal, which is the major cause of the adsorption. The size of the crystals reduced majorly compared to Cu-BTC.
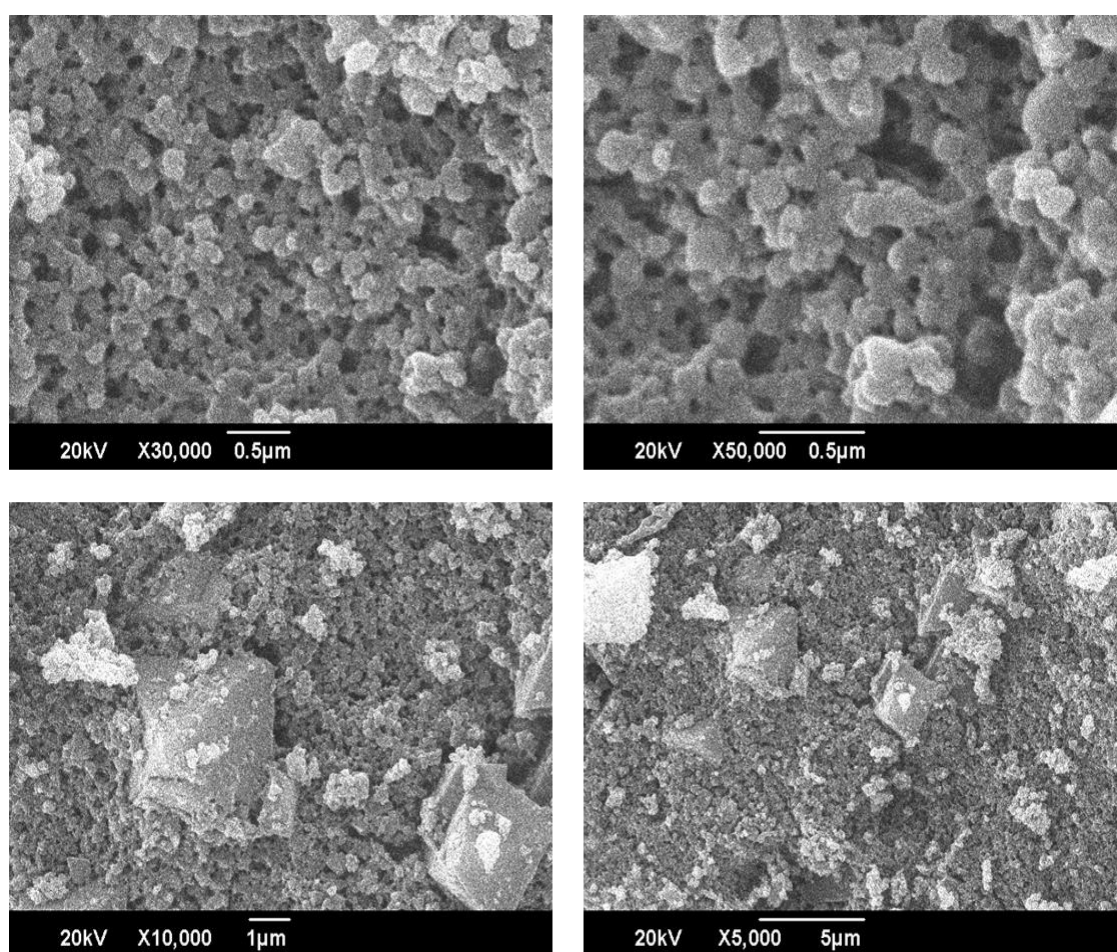
Figure 5.7 SEM images of HMTA-Cu-BTC

5.4.4 SEM analysis of Mel-Cu-BTC

Figure 5.8 represents the multiple resolution SEM images to illustrate the structure of Mel-Cu-BTC. The MOF depicts a structure of crystals with irregular shape. The

synthesized MOF shows the characteristics octahedral structure while the crystal size of the MOF is not uniform.

The high-resolution image of the MOF also shows the porous structure of the crystal, which is the major cause of the adsorption. The size of the crystals reduced majorly compared to Cu-BTC.
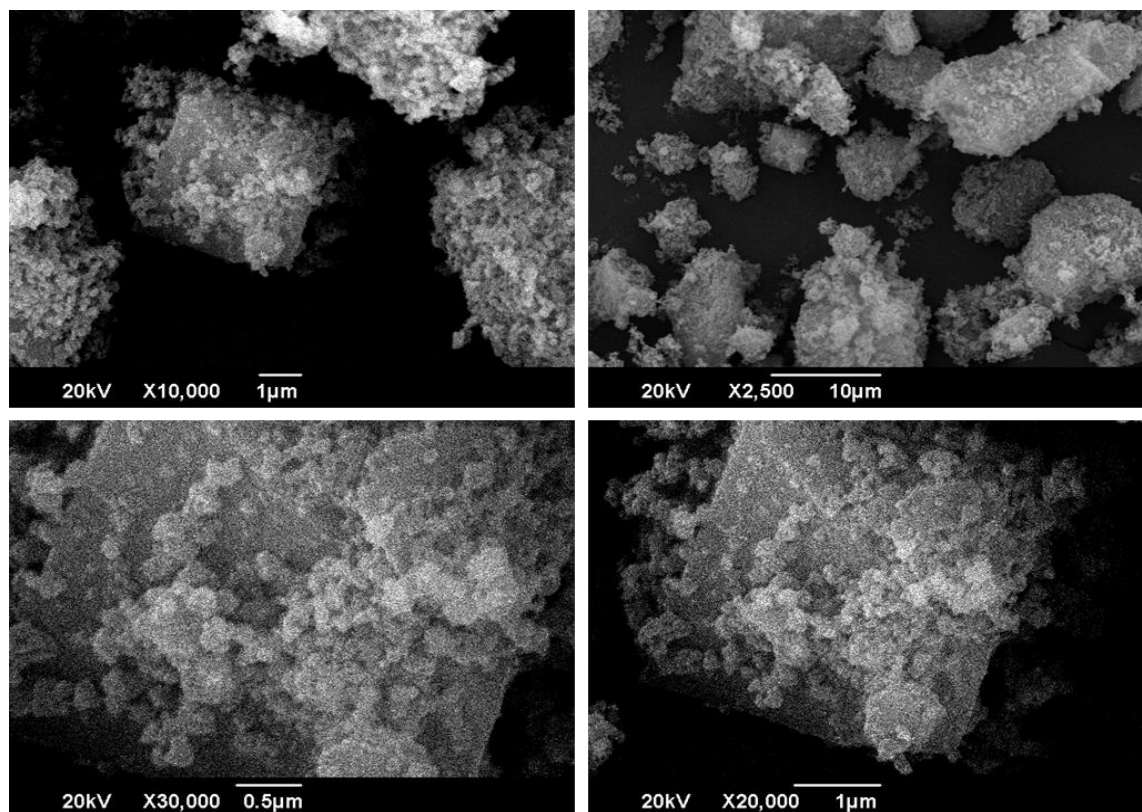
Figure 5.8 SEM images of Mel-Cu-BTC

5.5 Energy Dispersive X-ray

Using EDX, the element analysis is ascertained. SEM is used to perform EDX; however, the material must first be dried. To prevent the components from charging, the sample was coated with gold using a coater after it had dried. Subsequently, the sample was placed inside the SEM, and images were captured. The SEM picture was then sent from the SEM to the EDX program, where you could designate the region of the image for elemental analysis. The elemental analysis of the Cu-BTC metal organic framework and its amine modifications is displayed in the following table 5-1 by the weight percentage. Elemental analysis of Cu-BTC reveals the presence of carbon, oxygen, and copper and amine modified MOF have peaks for nitrogen as well.
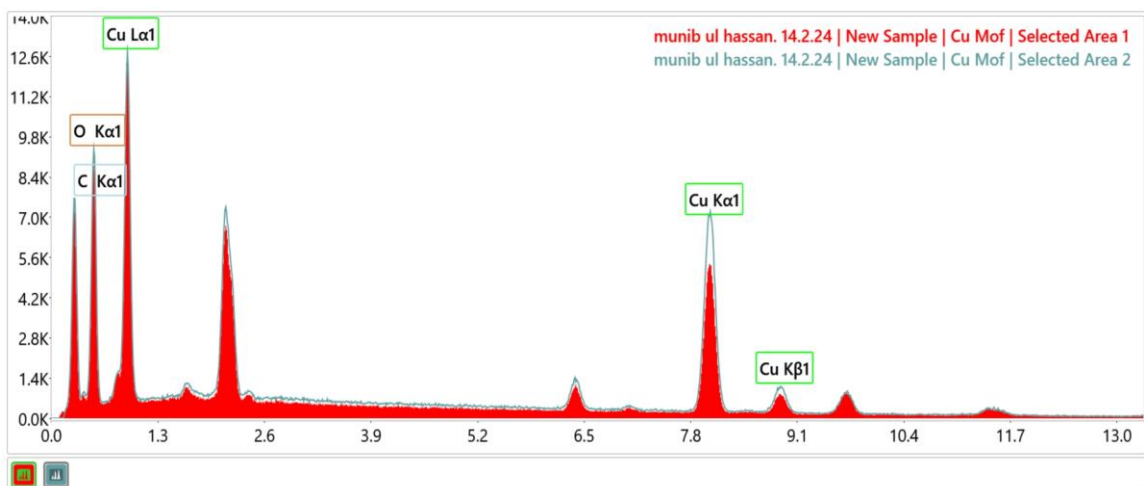
Figure 5.9 EDX of Cu-BTC
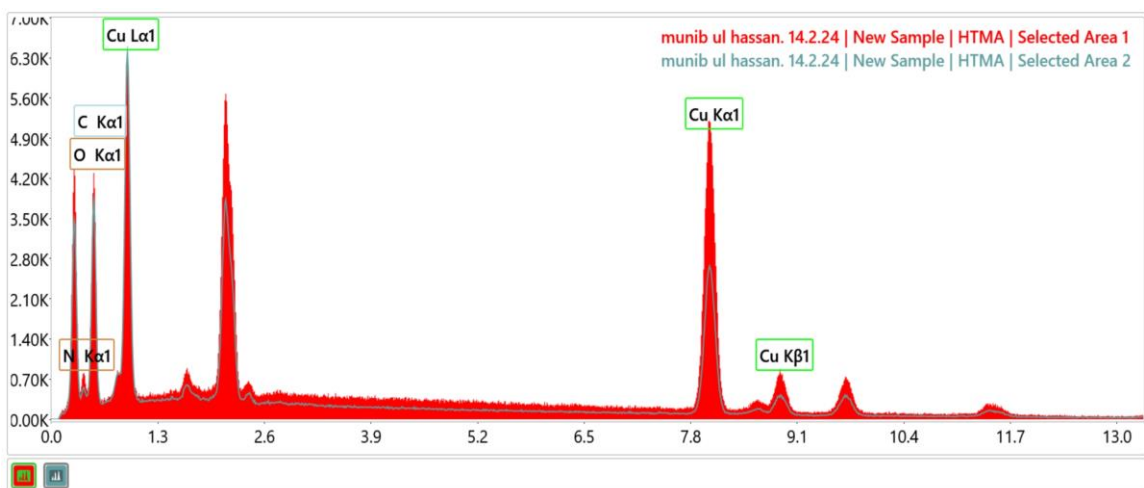
Figure 5.10 EDX of HMTA-Cu-BTC
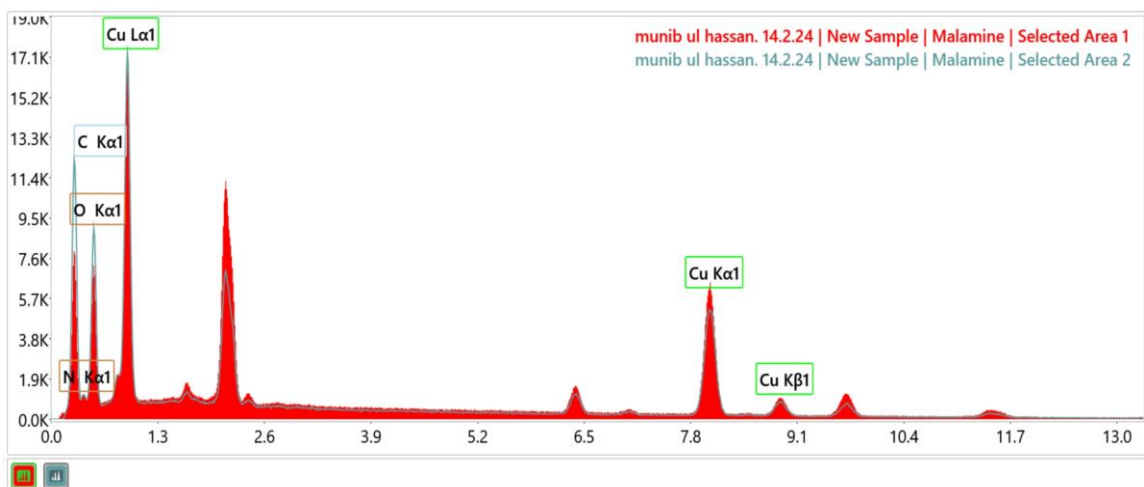
Figure 5.11 EDX of Mel-Cu-BTC
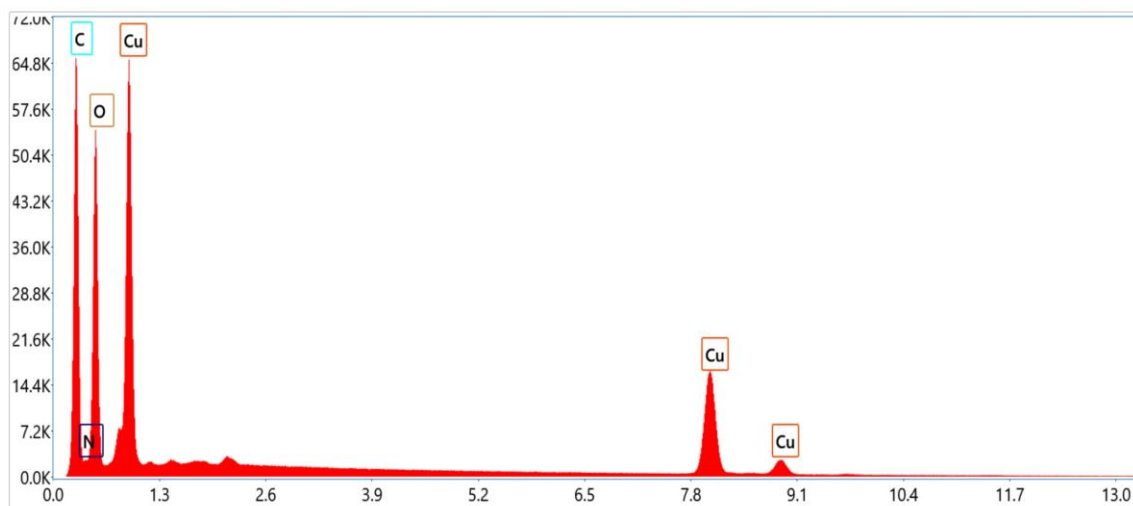
Figure 5.12 EDX of DPA-Cu-BTC

Table 5.1 Elemental composition of the samples (Wt%)

Elements	Cu-BTC	Mel-Cu-BTC	HMTA-Cu-BTC	DPA-Cu-BTC
Copper	26.3	28.0	35.2	12.8
Carbon	48.7	48.5	43.5	55.5
Oxygen	25.0	18.9	16.3	28.7
Nitrogen	0	4.7	5.0	3.0

5.6 Adsorption/desorption data

The MOF was delivered straight into the system as a powder. In order to remove all guest molecules and moisture content from the samples, they were heated to 100 degrees Celsius in a vacuum oven for a whole day. The materials were degassed for 10 hours at a high temperature of 150 °C under vacuum in order to prepare them for the CO_2 adsorption research analysis experiment. The 298 K temperature and 0–15 bar pressure range were used for the adsorption studies. After analyzing and importing the generated adsorption isotherms into Origin, graphs could be created.

The procedure for filling the sample is as follows. Using an analytical balance, determine the sample's weight initially. Once the weight of the sample required for

testing has been determined, take the measured sample and make sure all necessary accessories are ready before filling samples. These accessories include a funnel, sample cell, screw rod, screwdriver, filling blocks, and filter foam.

Measure the sample cell when it is empty. Take the funnel, place it inside the sample cell, and then add samples. The sample cell weight is obtained by measuring the sample cell weight once more after it has been filled. By subtracting the empty cell weight from the sample cell weight, we can determine the sample's weight. Next, insert one screw rod into the sample cell. To screw the rod, use the screwdriver. Prior to filling the last block, fill in the filter foam and a few filling blocks after screwing. Fill in the final filling block at the very end. Keep the filling block inside the sample cell.

5.6.1 Adsorption Comparison

The findings of every sample we generated are displayed in the table 5.2, and it is clear from there that the sample with DPA-Cu-BTC has the maximum CO_2 adsorption capability when compared to all other samples.

Table 5.2 Comparison of adsorption capacity at 15bar

Sr. No.	MOF	Adsorption Quantity(mmol/g)
1	Cu-BTC	1.980
2	Mel-Cu-BTC	1.195
3	HMTA-Cu-BTC	1.032
4	DPA-Cu-BTC	2.518

5.6.2 Adsorption and Desorption Curves of Cu-BTC

The Cu-BTC adsorption/desorption data is shown in the table 5.3. Both the adsorption and the desorption isotherms increase in a downward and upward direction, respectively. The adsorption analysis takes place between 0 and 15 bar of pressure at 50 °C.

The graph, which displays the adsorption and desorption curves, is drawn between the CO_2 pressure (bar) and the CO_2 quantity adsorbed or desorbed (mmol/g). For the CO_2 analysis, a 0.5g sample of Cu-BTC is utilized.

Table 5.3 Adsorption and desorption data of Cu-BTC

Absolute Pressure (Bar)	Cumu. Absorbance (mmol/g.STP)	Absolute Pressure (Bar)	Cumu. Desorbance (mmol/g.STP)
15.24048	1.980574	15.24048	1.980574
13.509396	1.921263	13.253026	1.911646
12.059843	1.855726	12.193118	1.858744
10.528608	1.770427	10.471393	1.766817
9.133054	1.673726	9.022771	1.663437
7.517223	1.537151	7.632376	1.54206
6.26859	1.401549	6.085615	1.37021
4.55846	1.169356	4.60092	1.163483
2.758703	0.828592	3.132234	0.878971
1.427586	0.478222	2.058649	0.611893
0.838545	0.296094	1.393025	0.415188
0.481202	0.175413	0.962074	0.272229

Adsorption increases significantly when pressure rises from 0 to 3 bars at first; it then rises as pressure rises from 3 to 5 bars, and it stabilizes at pressure rises from 5 to 8 bars; finally, there is a significant increase in adsorption as pressure rises from 8 to 11 bars and the adsorption also increases from 1.4 to 1.7 mmol/g. Adsorption increases constantly between 11 and 13 bars of pressure, and it increases continuously in a linear trend starting at 11 bars of pressure and there is lesser increase in adsorption depicting

saturation; at the moment when the pressure hits 15 bar, the adsorption is 2.0 mmol/g. At 15 bar of pressure, Cu-BTC MOF adsorbs at a rate of 1.98 mmol/g. The Cu-BTC adsorption isotherms are shown in figure 5.13.
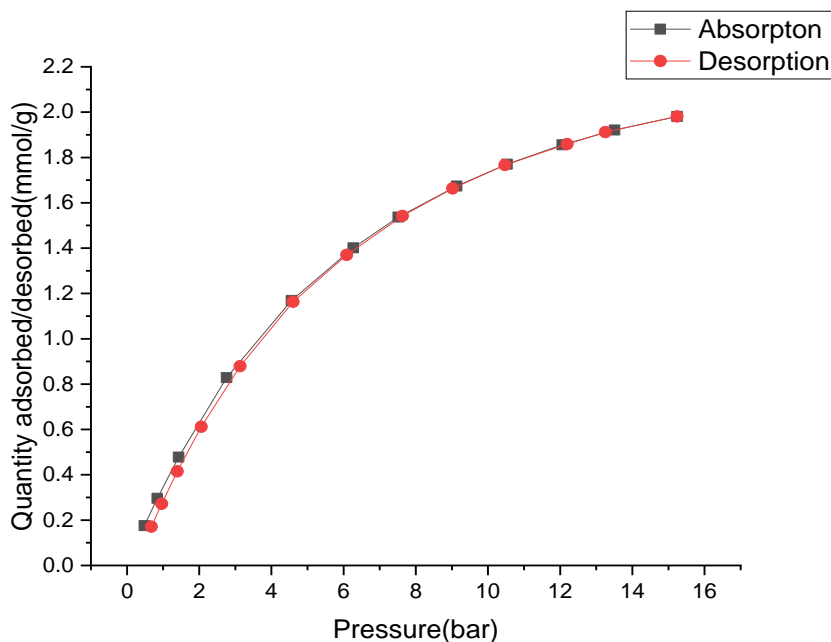
Figure 5.13 Adsorption and desorption isotherm of Cu-BTC

According to the desorption pattern, depressurization happens when the pressure begins to drop from 15 bar, and in Cu-BTC MOF, there is a linear trend; as the pressure begins to drop from 15 bar, desorption begins, and it continues to grow. Desorption somewhat increases in the pressure range of 12 to 8 bar.

The desorption line roughly corresponds to the trend of the adsorption line. A less quantity of CO_2 is desorbed as the pressure drops from 8 bar, and finally, the desorption ceases at 0.5 bar. Desorption was found to be 100%, leaving 0.1 mmol/g behind.

5.6.3   Adsorption and Desorption Curves of Mel-Cu-BTC

The adsorption/desorption data of the Mel-Cu-BTC MOF are shown in the table 5.4. The desorption isotherm increases in a downward direction, whereas the adsorption isotherm increases in an ascending direction. The pressure range for the adsorption analysis is 0–15 bar, and it takes place at 50 °C. The graph displays the adsorption and desorption curves and is plotted between the CO_2 pressure (bar) and the CO_2 amount

61

adsorbed or desorbed (mmol/g). For the CO_2 adsorption study analysis, a 1g sample of Mel-Cu-BTC MOF is used.

There is a small amount of CO_2 being adsorbed at the beginning of the adsorption as the pressure starts to increase from 0 to 5 bar. As the pressure increases, the adsorption almost becomes persistent; it is very minor in the pressure range from 5.8 bar so it becomes constant; there is negligible change in the adsorption. The adsorption increases when the pressure climbs over 8 bar. The adsorption is constantly rising when the pressure is between 8 and 15 bar. Adsorption increases between pressures of 12 and 15 bar, and when adsorption grows within this pressure range, there is a notable and abrupt increase in adsorption. This sample's CO_2 at 15 bar is 1.195989 mmol/g. Comparing the adsorption to the Mel-Cu-BTC MOF, it decreases. The adsorption/desorption isotherms of the Mel-Cu-BTC MOF are shown in figure 5.14.

Table 5.4 Adsorption and desorption data of Mel-Cu-BTC

Absolute Pressure (Bar)	Cumu. Absorbance (mmol/g.STP)	Absolute Pressure (Bar)	Cumu. Absorbance (mmol/g.STP)
15.155194	1.195989	15.155194	1.195989
13.489261	1.148709	13.341927	1.14775
12.072042	1.099988	12.068707	1.108773
10.579095	1.014978	10.469229	1.04523
8.898091	0.936655	9.093777	0.983141
7.687971	0.872322	7.538165	0.90199
6.103533	0.776915	6.027506	0.808157
4.567718	0.671583	4.568933	0.707467
2.880264	0.514677	3.077416	0.563173
1.470012	0.327868	1.867732	0.409716
0.859678	0.221422	1.179013	0.288903
0.521612	0.148031	0.772743	0.200147

Figure 5.14 Adsorption and desorption isotherm of Mel-Cu-BTC

The depressurization commences as the pressure starts to drop from 15 bar, according to the desorption curve. The desorption curves exhibit a similar pattern to the adsorption curves. Within the same procedure, a considerable amount of CO_2 is desorbed as the pressure drops from 15 to 11 bar. Desorption takes place when the additional pressure drops from 11 to 6 bar, as seen by the shift in the curve. However, as the pressure drops even lower, the curve becomes linear, and at 0.3 bar, the line becomes straight. The desorption ceases at 0.3 bar, with a total of 1.19 mmol/g of desorption. This indicates nearly 100% desorption.

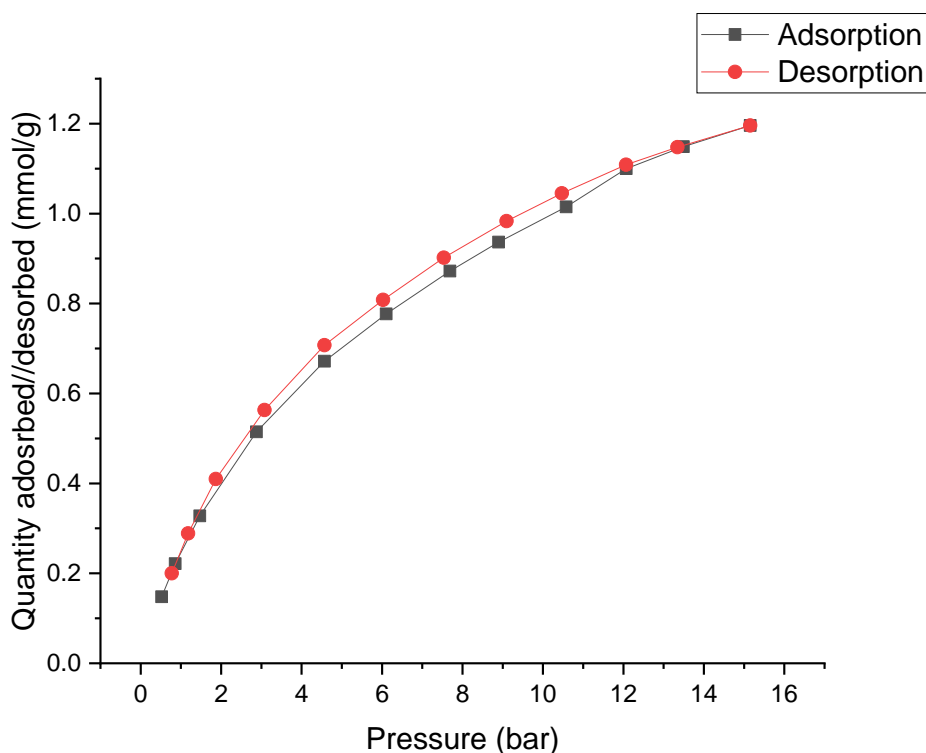### 5.6.4   *Adsorption and Desorption Curves of HMTA-Cu-BTC*

The adsorption and desorption data of the HMTA-Cu-BTC MOF are shown in the table 5.5. The desorption isotherm increases in a descending direction whereas the adsorption isotherm grows upward. The adsorption analysis takes place between 0 and 15 bar of pressure at 50 °C. The graph displays the adsorption and desorption curves, and it is positioned between the CO_2 pressure (bar) and the CO_2 amount that has been adsorbed or desorbed (mmol/g). The HMTA-Cu-BTC MOF composite, weighing 1.0

g, is the sample utilized for the CO_2 adsorption investigation. It can be seen in the graph, adsorption begins when the pressure starts to build from 0 to 7 bar at the beginning of the process. Adsorption rises together with the pressure, from 7 to 11 bar, and the line becomes linear as a result of the continuous increase in adsorption. The amount of CO_2 that is adsorbed increases from 0.75 mmol/g to 0.98 mmol/g when pressure climbs from 8 to 14 bar, although relatively little of the gas has been adsorbed. Adsorption increases even further at pressures between 14 and 15 bar, when a significant amount of CO_2 has been adsorbed. At 15 pressure, this sample's CO_2 adsorption is 1.03 mmol/g. When compared to the Cu-BTC sample, the adsorption of this sample rises and yields a much lower result at a pressure of 15 bar.

Table 5.5 Adsorption and desorption data of HMTA-Cu-BTC

Absolute Pressure(Bar)	Cumu. Absorbance (mmol/g.STP)	Absolute Pressure(Bar)	Cumu. Absorbance (mmol/g.STP)
15.161959	1.032718	15.161959	1.032718
13.361527	0.985684	13.348845	0.988974
12.103476	0.938603	12.067715	0.94504
10.502004	0.882505	10.456343	0.888054
9.013084	0.826949	9.077514	0.828091
7.584887	0.753397	7.522251	0.749794
6.126575	0.675841	6.065441	0.668074
4.56185	0.577597	4.554223	0.571349
2.941939	0.444895	3.086055	0.447337
1.472122	0.287336	1.843652	0.314968
0.87231	0.201444	1.143463	0.214897
0.525867	0.137375	0.731548	0.142017

The MOF's ability to absorb the additional CO_2 is demonstrated by the adsorption isotherm's rising trend. The adsorption/desorption isotherms of the HMTA-Cu-BTC MOF are shown in figure 5.15.

Depressurization happens when the pressure starts to drop from 15 bar, according to the desorption pattern. The desorption isotherm at this range lies on the adsorption isotherm. When the pressure further decreases from 11-8 bar, the desorption isotherm almost straightens, and very little CO_2 has been desorbed during this pressure range. Desorption occurs as pressures decrease from 15-11 bar and a very enormous amount of CO_2 has been desorbed. The remaining CO_2 has desorbed as the pressure drops from 4 to 0.5 bar. The desorption was found to be 1.03 mmol/g and to halt at 0.5 bar of pressure.

Figure 5.15 Adsorption and desorption isotherm of HMTA-Cu-BTC

5.6.5 Adsorption and Desorption Curves of DPA-Cu-BTC

The adsorption/desorption isotherms of the DPA-Cu-BTC MOF are shown in the figure 5.16. Both the desorption and the adsorption isotherms increase in a downward

and upward direction, respectively. The adsorption analysis takes place between 0 and 15 bar of pressure at 45 °C. The graph displays the adsorption and desorption curves and is located between the CO_2 pressure (bar) and the CO_2 amount adsorbed or desorbed (mmol/g). To analyze the CO_2 adsorption investigation, a 1.0g sample of DPA-Cu-BTC MOF is employed.

Adsorption begins as soon as the pressure rises from 0 to 2 bar, and we can observe an almost continuous linear increase in the amount of CO_2 that has been adsorbed. A little bit more CO_2 has been adsorbed when the pressure climbs from 2 to 8 bar. Once more, we see a constant linear adsorption as the pressure climbs from 8 to 11 bar, but significantly less adsorption occurs as the pressure rises from 11 to 14 bar. When the pressure is increased to 15 bar, the highest amount of adsorption is 2.51 mmol/g. The MOF has a CO_2 adsorption of 2.51 mmol/g at 15 bar. At a pressure of 15 bar, the adsorption of this sample yields a much higher result than that of the preceding sample.

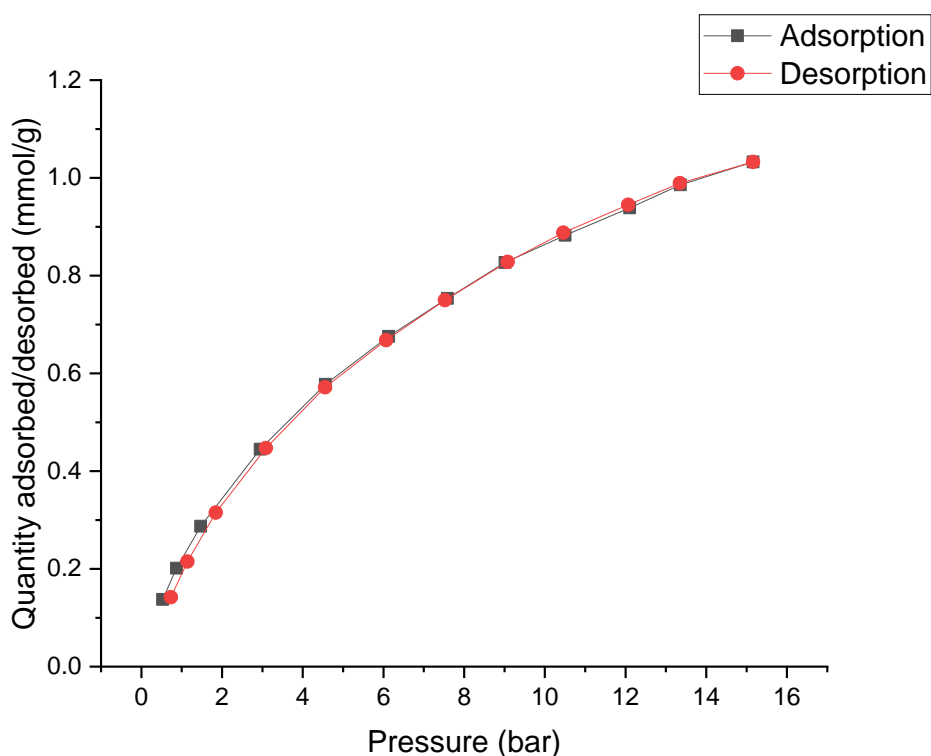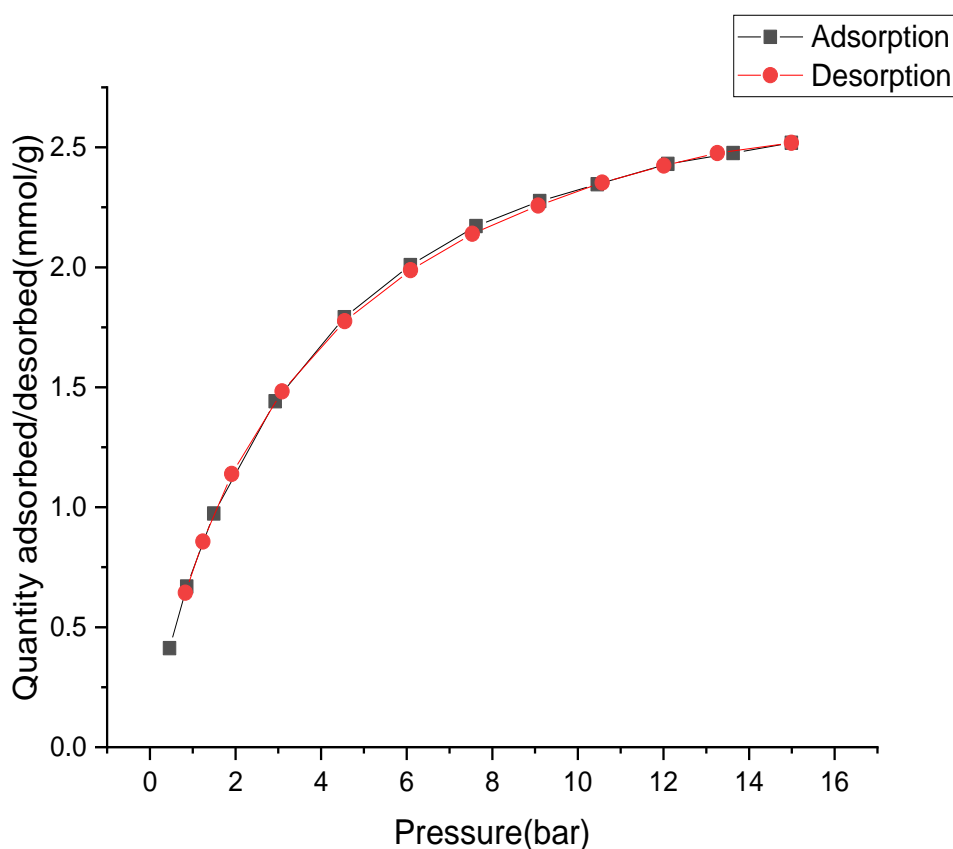**Figure 5.16** Adsorption and desorption isotherm of DPA-Cu-BTC

Table 5.6 Adsorption and desorption data of DPA-Cu-BTC

Absolute Pressure (Bar)	Cumu. Absorbance (mmol/g.STP)	Absolute Pressure (Bar)	Cumu. Absorbance (mmol/g.STP)
14.989441	2.518493	14.989441	2.518493
13.26096	2.476201	13.628278	2.475924
12.007197	2.423768	12.102561	2.430594
10.570344	2.35308	10.452715	2.345991
9.070951	2.256944	9.109664	2.275783
7.533494	2.139905	7.622041	2.171569
6.092569	1.987972	6.088256	2.009281
4.552568	1.775569	4.546359	1.792209
3.089006	1.482797	2.926901	1.4415
1.913131	1.138462	1.494748	0.973722
1.23742	0.857069	0.863744	0.66956
0.830056	0.643387	0.460634	0.412179

Depressurization happens when the pressure starts to drop from 15 bar, according to the desorption pattern. Desorption happens quite linearly as the pressure drops from 15 to 13 bar, and a sizable quantity of CO_2 desorbed in this pressure range. It is evident that the desorption behavior changes when the pressure drops from 13 to 10 bar.

The desorption behavior gets increasingly fascinating as the pressure drops farther from 10-1 bar and eventually stops at 0.1 bar. The tendency of the desorption isotherms is identical to the adsorption isotherms. 2.51 mmol/g of carbon dioxide were desorbed in total, with the remaining carbon dioxide remaining behind after the process ends at 0.1 bar of pressure. The graph below illustrates a number of patterns, but when we compare this sample to the rest of the sample examined before, the adsorption value is greater, indicating that this sample has adsorbed a higher quantity of CO_2.

CHAPTER 6   CONCLUSIONS AND RECOMMANDATION

This thesis focused on the synthesis, characterization, and adsorption and desorption studies of Copper MOF and its amine modifications using melamine, diphenyl and hexamethylenetetramine (HMTA). MOFs offer broad surface area, particular pore sizes, affordability, and molecular sieving capability make them suitable for a variety of uses. Fossil fuels and other energy sources with substantial CO_2 emissions are major contributors to global climate change. Carbon carbon can help reduce these emissions. For the application of carbon capture, the Cu-BTC and its amine modifications were prepared using hydrothermal processing. The samples were analyzed using FTIR, SEM, and XRD among other identification techniques. The functional groups present in our samples are all extensively identified by the FTIR research. The 2D framework and sheets of MOFs are clearly visible in the SEM pictures. Physical characteristics including particle orientation, crystal structure, and phase composition are examined using X-ray diffraction (XRD). For verification, the XRD, SEM and FTIR results were accurately compared with already published research.

The particle size was seen to have a wide range in SEM images for MOFs. The EDX showed the presence of copper (Cu), oxygen(O), nitrogen (N) and carbon only. A high-pressure sorption analyzer was used to test the carbon dioxide adsorption capacity of metal organic framework. The MOFs generally showed good carbon dioxide adsorption capability. At 1.980 mmol/g, the Cu-BTC exhibited a high adsorption capability. The highest adsorption capacity was obtained, however, when diphenylamine was used to modify the MOF. At a pressure of 15bar, the DPA-modified copper MOF exhibited an adsorption capacity of 2.518 mmol/g. However, the other two amine-modified MOFs had a reduced adsorption capacity. Melamine and HMTA modified MOF showed 1.195 and 1.032 mmol/g of adsorption, respectively. Because there were more collisions in each case, the adsorption of carbon dioxide increased as pressure rose. The overall pattern has a sharp gradient at first, which gradually becomes less steep until a uniform state is attained, signifying saturation.

6.1   Future recommendations

Testing the Cu-BTC MOF carbon dioxide adsorption capacity at various temperatures while keeping the pressure constant is advised, these results can then be verified by Langmuir model. Future efforts to guarantee the stability over the long term are advised of MOFs in high-pressure, humid conditions, with particular emphasis to how mechanical stress affects MOFs. The Cu-BTC and its modifications may be employed for the adsorption of various gases such as ammonia, methane, and nitrogen. The CO_2 adsorption capacity of MOFs can be explored by manufacturing membranes from the MOFs that can be made with a suitable polymer.

REFERENCES

[1] D. J. Hofmann, J. H. Butler, and P. P. Tans, "A new look at atmospheric carbon dioxide," *Atmos Environ*, vol. 43, no. 12, pp. 2084–2086, 2009.

[2] Z. Zhang, S. Xian, Q. Xia, H. Wang, Z. Li, and J. Li, "Enhancement of CO_2 adsorption and CO_2/N_2 selectivity on ZIF-8 via postsynthetic modification," *AIChE Journal*, vol. 59, no. 6, pp. 2195–2206, 2013.

[3] D. Aaron and C. Tsouris, "Separation of CO_2 from flue gas: a review," *Sep Sci Technol*, vol. 40, no. 1–3, pp. 321–348, 2005.

[4] M. R. Raupach *et al.*, "Global and regional drivers of accelerating CO_2 emissions," *Proceedings of the National Academy of Sciences*, vol. 104, no. 24, pp. 10288–10293, 2007.

[5] K. M. K. Yu, I. Curcic, J. Gabriel, and S. C. E. Tsang, "Recent advances in CO_2 capture and utilization," *ChemSusChem: Chemistry & Sustainability Energy & Materials*, vol. 1, no. 11, pp. 893–899, 2008.

[6] G. Petrecca, "Energy Conversion and Management," *Cham, Switzerland*, pp. 101–103, 2014.

[7] F. N. Tubiello, M. Salvatore, S. Rossi, A. Ferrara, N. Fitton, and P. Smith, "The FAOSTAT database of greenhouse gas emissions from agriculture," *Environmental Research Letters*, vol. 8, no. 1, p. 015009, 2013.

[8] P. C. Jain, "Greenhouse effect and climate change: scientific basis and overview," *Renew Energy*, vol. 3, no. 4, pp. 403–420, 1993,

[9] D. Nong, P. Simshauser, and D. B. Nguyen, "Greenhouse gas emissions vs CO_2 emissions: Comparative analysis of a global carbon tax," *Appl Energy*, vol. 298, p. 117223, 2021.

[10] M. N. Dudin, E. E. Frolova, O. V. Protopopova, O. Mamedov, and S. V. Odintsov, "Study of innovative technologies in the energy industry: nontraditional and renewable energy sources," *Entrepreneurship and Sustainability Issues*, vol. 6, no. 4, p. 1704, 2019.

[11] M. A. Clark *et al.*, "Global food system emissions could preclude achieving the 1.5 and 2C climate change targets," *Science (1979)*, vol. 370, no. 6517, pp. 705–708, 2020.

[12] M. N. Dods, E. J. Kim, J. R. Long, and S. C. Weston, "Deep CCS: Moving Beyond 90% Carbon Dioxide Capture," *Environ Sci Technol*, vol. 55, no. 13, pp. 8524–8534, Jul. 2021.

[13] J. J. Higgins and A. Novels, "Quoted in Congressional Report Dec 5, 2018".

[14] E. S. G. Challenge, "Energy storage market report," *US Department of Energy: Washington, DC, USA*, 2020.

[15] H. Waisman, H. De Coninck, and J. Rogelj, "Key technological enablers for ambitious climate goals: insights from the IPCC special report on global warming of 1.5 C," *Environmental Research Letters*, vol. 14, no. 11, p. 111001, 2019.

[16] I. Sreedhar, R. Aniruddha, and S. Malik, "Carbon capture using amine modified porous carbons derived from starch (Starbons®)," *SN Appl Sci*, vol. 1, no. 5, p. 463, 2019.

[17] S. G. Subraveti *et al.*, "Cycle design and optimization of pressure swing adsorption cycles for pre-combustion CO_2 capture," *Appl Energy*, vol. 254, p. 113624, 2019.

[18] P. Linga, R. Kumar, and P. Englezos, "The clathrate hydrate process for post and pre-combustion capture of carbon dioxide," *J Hazard Mater*, vol. 149, no. 3, pp. 625–629, 2007.

[19] E. Agbor, A. O. Oyedun, X. Zhang, and A. Kumar, "Integrated techno-economic and environmental assessments of sixty scenarios for co-firing biomass with coal and natural gas," *Appl Energy*, vol. 169, pp. 433–449, 2016.

[20] H. J. Herzog, "The economics of CO_2 capture," *Greenhouse Gas Control Technologies, Elsevier Science*, pp. 101–106, 1999.

[21] A. I. Osman, M. Hefny, M. I. A. Abdel Maksoud, A. M. Elgarahy, and D. W. Rooney, "Recent advances in carbon capture storage and utilisation technologies: a review," *Environ Chem Lett*, vol. 19, no. 2, pp. 797–849, 2021.

[22] E. S. Rubin, H. Mantripragada, A. Marks, P. Versteeg, and J. Kitchin, "The outlook for improved carbon capture technology," *Prog Energy Combust Sci*, vol. 38, no. 5, pp. 630–671, 2012.

[23] Q. Wang, J. Luo, Z. Zhong, and A. Borgna, "CO_2 capture by solid adsorbents and their applications: current status and new trends," *Energy Environ Sci*, vol. 4, no. 1, pp. 42–55, 2011.

[24] R. M. Barrer, "Zeolites and clay minerals as sorbents and molecular sieves," *(No Title)*, 1978.

[25] A. I. Skoulidas, D. S. Sholl, and J. K. Johnson, "Adsorption and diffusion of carbon dioxide and nitrogen through single-walled carbon nanotube membranes," *J Chem Phys*, vol. 124, no. 5, 2006.

[26] S. Choi, J. H. Drese, and C. W. Jones, "Adsorbent materials for carbon dioxide capture from large anthropogenic point sources," *ChemSusChem: Chemistry & Sustainability Energy & Materials*, vol. 2, no. 9, pp. 796–854, 2009.

[27] I. Hinkov, F. Lamari, P. Langlois, M. Dicko, C. Chilev, and I. Pentchev, "Carbon dioxide capture by adsorption," *Journal of Chemical Technology and Metallurgy (JCTM)*, vol. 51, no. 6, pp. 609–626, 2016.

[28] O. Shekhah, J. Liu, R. A. Fischer, and C. Wöll, "MOF thin films: existing and future applications," *Chem Soc Rev*, vol. 40, no. 2, pp. 1081–1106, 2011.

[29] J. Liu, P. K. Thallapally, B. P. McGrail, D. R. Brown, and J. Liu, "Progress in adsorption-based CO_2 capture by metal–organic frameworks," *Chem Soc Rev*, vol. 41, no. 6, pp. 2308–2322, 2012.

[30] R. Thiruvenkatachari, S. Su, H. An, and X. X. Yu, "Post combustion CO_2 capture by carbon fibre monolithic adsorbents," *Prog Energy Combust Sci*, vol. 35, no. 5, pp. 438–455, 2009.

[31] A. Thomas *et al.*, "Graphitic carbon nitride materials: variation of structure and morphology and their use as metal-free catalysts," *J Mater Chem*, vol. 18, no. 41, pp. 4893–4908, 2008.

[32] S. Choi, J. H. Drese, and C. W. Jones, "Adsorbent materials for carbon dioxide capture from large anthropogenic point sources," *ChemSusChem: Chemistry & Sustainability Energy & Materials*, vol. 2, no. 9, pp. 796–854, 2009.

[33] H.-S. Zhai, L. Cao, and X.-H. Xia, "Synthesis of graphitic carbon nitride through pyrolysis of melamine and its electrocatalysis for oxygen reduction reaction," *Chinese Chemical Letters*, vol. 24, no. 2, pp. 103–106, 2013.

[34] Z. Zhang, T. N. G. Borhani, and M. H. El-Naas, "Chapter 4.5 - Carbon Capture," in *Exergetic, Energetic and Environmental Dimensions*, I. Dincer, C. O. Colpan, and O. Kizilkan, Eds., Academic Press, 2018, pp. 997–1016.

[35] Z. Zhang *et al.*, "Recent advances in carbon dioxide utilization," *Renewable and Sustainable Energy Reviews*, vol. 125, p. 109799, 2020.

[36] E. Haldoupis *et al.*, "Ab initio derived force fields for predicting CO_2 adsorption and accessibility of metal sites in the metal–organic frameworks M-MOF-74 (M= Mn, Co, Ni, Cu)," *The Journal of Physical Chemistry C*, vol. 119, no. 28, pp. 16058–16071, 2015.

[37] J. Yu, L.-H. Xie, J.-R. Li, Y. Ma, J. M. Seminario, and P. B. Balbuena, "CO_2 capture and separations using MOFs: computational and experimental studies," *Chem Rev*, vol. 117, no. 14, pp. 9674–9754, 2017.

[38] K. Sumida and D. L. Rogow, "J. a. Mason, TM McDonald, ED Bloch, ZR Herm, T.-H. Bae and JR Long," *Chem. Rev*, vol. 112, pp. 724–781, 2012.

[39] S. S.-Y. Chui, S. M.-F. Lo, J. P. H. Charmant, A. G. Orpen, and I. D. Williams, "A chemically functionalizable nanoporous material [$Cu_3(TMA)_2(H_2O)_3$] n," *Science (1979)*, vol. 283, no. 5405, pp. 1148–1150, 1999.

[40] F. Gul-E-Noor, B. Jee, A. Pöppl, M. Hartmann, D. Himsl, and M. Bertmer, "Effects of varying water adsorption on a $Cu_3(BTC)_2$ metal–organic framework (MOF) as studied by ^{1}H and ^{13}C solid-state NMR spectroscopy," *Physical Chemistry Chemical Physics*, vol. 13, no. 17, pp. 7783–7788, 2011.

[41] S. Bordiga *et al.*, "Adsorption properties of HKUST-1 toward hydrogen and other small molecules monitored by IR," *Physical Chemistry Chemical Physics*, vol. 9, no. 21, pp. 2676–2685, 2007.

[42] M. Du, L. Li, M. Li, and R. Si, "Adsorption mechanism on metal organic frameworks of Cu-BTC, Fe-BTC and ZIF-8 for CO_2 capture investigated by X-ray absorption fine structure," *RSC Adv*, vol. 6, no. 67, pp. 62705–62716, 2016.

[43] L. Grajciar, A. D. Wiersum, P. L. Llewellyn, J.-S. Chang, and P. Nachtigall, "Understanding CO_2 adsorption in CuBTC MOF: comparing combined DFT–ab initio calculations with microcalorimetry experiments," *The Journal of Physical Chemistry C*, vol. 115, no. 36, pp. 17925–17933, 2011.

[44] Y. Yan *et al.*, "Modulating the packing of [Cu 24 (isophthalate) 24] cuboctahedra in a triazole-containing metal–organic polyhedral framework," *Chem Sci*, vol. 4, no. 4, pp. 1731–1736, 2013.

[45] J. J. Gutiérrez-Sevillano, J. M. Vicent-Luna, D. Dubbeldam, and S. Calero, "Molecular mechanisms for adsorption in Cu-BTC metal organic framework," *The Journal of Physical Chemistry C*, vol. 117, no. 21, pp. 11357–11366, 2013.

[46] W. Wong-Ng, I. Levin, J. A. Kaduk, L. Espinal, and H. Wu, "CO_2 capture and positional disorder in $Cu_3(1,3,5-benzenetricarboxylate)_2$: An in situ laboratory X-ray powder diffraction study," *J Alloys Compd*, vol. 656, pp. 200–205, 2016.

[47] B. Supronowicz, A. Mavrandonakis, and T. Heine, "Interaction of small gases with the unsaturated metal centers of the HKUST-1 metal organic framework," *The Journal of Physical Chemistry C*, vol. 117, no. 28, pp. 14570–14578, 2013.

[48] E. J. Granite and H. W. Pennline, "Photochemical removal of mercury from flue gas," *Ind Eng Chem Res*, vol. 41, no. 22, pp. 5470–5476, 2002.

[49] N. Al-Janabi, "Hill P. Torrente-Murciano L. Garforth A. Gorgojo P. Siperstein F. Fan X," *Chem. Eng. J*, vol. 281, pp. 669–677, 2015.

[50] N. Al-Janabi, A. Alfutimie, F. R. Siperstein, and X. Fan, "Underlying mechanism of the hydrothermal instability of $Cu_3(BTC)_2$ metal-organic framework," *Front Chem Sci Eng*, vol. 10, pp. 103–107, 2016.

[51] J. R. Álvarez *et al.*, "Structure stability of HKUST-1 towards water and ethanol and their effect on its CO_2 capture properties," *Dalton Transactions*, vol. 46, no. 28, pp. 9192–9200, 2017.

[52] L. Garzon-Tovar, M. Cano-Sarabia, A. Carné-Sánchez, C. Carbonell, I. Imaz, and D. Maspoch, "A spray-drying continuous-flow method for simultaneous synthesis and shaping of microspherical high nuclearity MOF beads," *React Chem Eng*, vol. 1, no. 5, pp. 533–539, 2016.

[53] M. Yaseen *et al.*, "Diversity and recent progressive trend in MOFs-based photo-electrocatalysts for selective CO_2 reduction," *Ceram Int*, vol. 48, no. 22, pp. 32677–32695, 2022.

[54] M. H. Yap, K. L. Fow, and G. Z. Chen, "Synthesis and applications of MOF-derived porous nanostructures," *Green Energy & Environment*, vol. 2, no. 3, pp. 218–245, 2017.

[55] S. Sağlam, F. N. Türk, and H. Arslanoğlu, "Use and applications of metal-organic frameworks (MOF) in dye adsorption," *J Environ Chem Eng*, p. 110568, 2023.

[56] H. Li *et al.*, "Porous metal-organic frameworks for gas storage and separation: Status and challenges," *EnergyChem*, vol. 1, no. 1, p. 100006, 2019.

[57] X. Cao, H. Li, J. Yi, F. Zhao, and Y. Hao, "Recent advances for water-stable metal-organic frameworks (MOFs)," in *Journal of Physics: Conference Series*, IOP Publishing, 2023, p. 062029.

[58] A. R. Godwin, *The synthesis and conjugation chemistry of polymeric precursors for medicine*. University of London, University College London (United Kingdom), 2001.

[59] A. Wibowo *et al.*, "Recent improvement strategies on metal-organic frameworks as adsorbent, catalyst, and membrane for wastewater treatment," *Molecules*, vol. 26, no. 17, p. 5261, 2021.

[60] L.-J. Han, F.-Y. Ge, G.-H. Sun, X.-J. Gao, and H.-G. Zheng, "Effective adsorption of Congo red by a MOF-based magnetic material," *Dalton Transactions*, vol. 48, no. 14, pp. 4650–4656, 2019.

[61] D. H. Hong, H. S. Shim, J. Ha, and H. R. Moon, "MOF-on-MOF architectures: applications in separation, catalysis, and sensing," *Bull Korean Chem Soc*, vol. 42, no. 7, pp. 956–969, 2021.

[62] V. I. Isaeva and L. M. Kustov, "The application of metal-organic frameworks in catalysis," *Petroleum Chemistry*, vol. 50, pp. 167–180, 2010.

[63] J. Liu, L. Chen, H. Cui, J. Zhang, L. Zhang, and C.-Y. Su, "Applications of metal–organic frameworks in heterogeneous supramolecular catalysis," *Chem Soc Rev*, vol. 43, no. 16, pp. 6011–6061, 2014.

[64] Z. Wu, Y. Li, C. Zhang, X. Huang, B. Peng, and G. Wang, "Recent advances in metal-organic-framework-based catalysts for thermocatalytic selective oxidation of organic substances," *Chem Catalysis*, vol. 2, no. 5, pp. 1009–1045, 2022.

[65] F. Ahmadijokani *et al.*, "COF and MOF hybrids: advanced materials for wastewater treatment," *Adv Funct Mater*, p. 2305527, 2023.

[66] W. Chai, Y. Shen, J. Wang, and G. Zhang, "Applications of Metal-Organic Framework Materials," in *Journal of Physics: Conference Series*, IOP Publishing, 2022, p. 012014.

[67] S. Ketrat, T. Maihom, S. Wannakao, M. Probst, S. Nokbin, and J. Limtrakul, "Coordinatively unsaturated metal–organic frameworks $M_3(btc)_2$ (M= Cr, Fe, Co, Ni, Cu, and Zn) catalyzing the oxidation of CO by N_2O: Insight from DFT calculations," *Inorg Chem*, vol. 56, no. 22, pp. 14005–14012, 2017.

[68] R.-B. Lin, S. Xiang, W. Zhou, and B. Chen, "Microporous metal-organic framework materials for gas separation," *Chem*, vol. 6, no. 2, pp. 337–363, 2020.

[69] H. A. Ozen and B. Ozturk, "Gas separation characteristic of mixed matrix membrane prepared by MOF-5 including different metals," *Sep Purif Technol*, vol. 211, pp. 514–521, 2019.

[70] F. Bahmanzadegan, M. A. Pordsari, and A. Ghaemi, "Improving the efficiency of 4A-zeolite synthesized from kaolin by amine functionalization for CO_2 capture," *Sci Rep*, vol. 13, no. 1, p. 12533, 2023.

[71]   A. Hedayati, B. A. Delica, S. Perez-Gil, and S. Prieto-Fernandez, "Evaluation of high-performance adsorbents for separation of CO_2 from industrial effluent gases," *Greenhouse Gases: Science and Technology*, vol. 13, no. 2, pp. 216–226, 2023.

[72]   M. Cavallo, M. Dosa, N. G. Porcaro, F. Bonino, M. Piumetti, and V. Crocellà, "Shaped natural and synthetic zeolites for CO_2 capture in a wide temperature range," *Journal of CO2 Utilization*, vol. 67, p. 102335, 2023.

[73]   S. Cavenati, C. A. Grande, and A. E. Rodrigues, "Adsorption equilibrium of methane, carbon dioxide, and nitrogen on Cu-BTC at high pressures," *J Chem Eng Data*, vol. 49, no. 4, pp. 1095–1101, 2004.

[74]   T. Loiseau *et al.*, "MIL-96, a porous aluminum trimesate 3D structure constructed from a hexagonal network of 18-membered rings and μ 3-oxo-centered trinuclear units," *J Am Chem Soc*, vol. 128, no. 31, pp. 10223–10230, 2006.

[75]   A. Demessence, D. M. D'Alessandro, M. L. Foo, and J. R. Long, "Strong CO_2 binding in a water-stable, triazolate-bridged metal− organic framework functionalized with ethylenediamine," *J Am Chem Soc*, vol. 131, no. 25, pp. 8784–8786, 2009.

[76]   K. Sumida *et al.*, "Hydrogen storage and carbon dioxide capture in an iron-based sodalite-type metal–organic framework (Fe-BTT) discovered via high-throughput methods," *Chem Sci*, vol. 1, no. 2, pp. 184–191, 2010.

[77]   J.-R. Li *et al.*, "Porous materials with pre-designed single-molecule traps for CO2 selective adsorption," *Nat Commun*, vol. 4, no. 1, p. 1538, 2013.

[78]   A. Mallick, S. Saha, P. Pachfule, S. Roy, and R. Banerjee, "Selective CO_2 and H_2 adsorption in a chiral magnesium-based metal organic framework (Mg-MOF) with open metal sites," *J Mater Chem*, vol. 20, no. 41, pp. 9073–9080, 2010.

[79]   S. R. Caskey, A. G. Wong-Foy, and A. J. Matzger, "Dramatic tuning of carbon dioxide uptake via metal substitution in a coordination polymer with cylindrical pores," *J Am Chem Soc*, vol. 130, no. 33, pp. 10870–10871, 2008.

[80] S.-N. Kim, J. Kim, H.-Y. Kim, H.-Y. Cho, and W.-S. Ahn, "Adsorption/catalytic properties of MIL-125 and NH$_2$-MIL-125," *Catal Today*, vol. 204, pp. 85–93, 2013.

[81] X. Si *et al.*, "High and selective CO$_2$ uptake, H$_2$ storage and methanol sensing on the amine-decorated 12-connected MOF CAU-1," *Energy Environ Sci*, vol. 4, no. 11, pp. 4522–4527, 2011.

[82] J. An, S. J. Geib, and N. L. Rosi, "High and Selective CO$_2$ Uptake in a Cobalt Adeninate Metal−Organic Framework Exhibiting Pyrimidine- and Amino-Decorated Pores," *J Am Chem Soc*, vol. 132, no. 1, pp. 38–39, Jan. 2012.

[83] J.-S. Qin *et al.*, "N-rich zeolite-like metal–organic framework with sodalite topology: high CO$_2$ uptake, selective gas adsorption and efficient drug delivery," *Chem Sci*, vol. 3, no. 6, pp. 2114–2118, 2012.

[84] K. Maity, C. K. Karan, and K. Biradha, "Porous Metal-Organic Polyhedral Framework containing Cuboctahedron Cages as SBUs with High Affinity for H$_2$ and CO$_2$ Sorption: A Heterogeneous Catalyst for Chemical Fixation of CO$_2$," *Chemistry–A European Journal*, vol. 24, no. 43, pp. 10988–10993, 2018.

[85] A. Demessence, D. M. D'Alessandro, M. L. Foo, and J. R. Long, "Strong CO$_2$ Binding in a Water-Stable, Triazolate-Bridged Metal−Organic Framework Functionalized with Ethylenediamine," *J Am Chem Soc*, vol. 131, no. 25, pp. 8784–8786, Jul. 2009.

[86] S. Lin *et al.*, "Adsorption behavior of metal–organic frameworks for methylene blue from aqueous solution," *Microporous and Mesoporous Materials*, vol. 193, pp. 27–34, 2014.

[87] A. Asghar, N. Iqbal, T. Noor, M. Ali, and T. L. Easun, "Efficient one-pot synthesis of a hexamethylenetetramine-doped Cu-BDC metal-organic framework with enhanced CO$_2$ adsorption," *Nanomaterials*, vol. 9, no. 8, p. 1063, 2019.

[88] B. J. Inkson, "Scanning electron microscopy (SEM) and transmission electron microscopy (TEM) for materials characterization," in *Materials*

characterization using nondestructive evaluation (NDE) methods, Elsevier, 2016, pp. 17–43.

[89] C. Blanthorne, L. A. Jones-Farmer, and E. D. Almer, "Why you should consider SEM: A guide to getting started," in *Advances in accounting behavioral research*, vol. 9, Emerald Group Publishing Limited, 2006, pp. 179–207.

[90] A. Mohammed and A. Abdullah, "Scanning electron microscopy (SEM): A review," in *Proceedings of the 2018 International Conference on Hydraulics and Pneumatics—HERVEX, Băile Govora, Romania*, 2018, pp. 7–9.

[91] G. Alberti and G. Nuzzaci, "1.6. 5 SEM and TEM techniques," in *World Crop Pests*, vol. 6, Elsevier, 1996, pp. 399–410.

[92] W. Zhou, R. Apkarian, Z. L. Wang, and D. Joy, "Fundamentals of scanning electron microscopy (SEM)," *Scanning microscopy for nanotechnology: techniques and applications*, pp. 1–40, 2007.

[93] R. Sharma, D. P. Bisen, U. Shukla, and B. G. Sharma, "X-ray diffraction: a powerful method of characterizing nanomaterials," *Recent Res Sci Technol*, vol. 4, no. 8, pp. 77–79, 2012.

[94] J. Epp, "X-ray diffraction (XRD) techniques for materials characterization," in *Materials characterization using nondestructive evaluation (NDE) methods*, Elsevier, 2016, pp. 81–124.

[95] B. E. Warren, "X-ray diffraction methods," *J Appl Phys*, vol. 12, no. 5, pp. 375–384, 1941.

[96] H. Khan, A. S. Yerramilli, A. D'Oliveira, T. L. Alford, D. C. Boffito, and G. S. Patience, "Experimental methods in chemical engineering: X-ray diffraction spectroscopy—XRD," *Can J Chem Eng*, vol. 98, no. 6, pp. 1255–1266, 2020.

[97] S. A. Khan, S. B. Khan, L. U. Khan, A. Farooq, K. Akhtar, and A. M. Asiri, "Fourier transform infrared spectroscopy: fundamentals and application in functional groups and nanomaterials characterization," *Handbook of materials characterization*, pp. 317–344, 2018.

[98] C. Berthomieu and R. Hienerwadel, "Fourier transform infrared (FTIR) spectroscopy," *Photosynth Res*, vol. 101, pp. 157–170, 2009.

[99] M. N. Dole, P. A. Patel, S. D. Sawant, and P. S. Shedpure, "Advance applications of Fourier transform infrared spectroscopy," *Int. J. Pharm. Sci. Rev. Res*, vol. 7, no. 2, pp. 159–166, 2011.

[100] S. Lin *et al.*, "Adsorption behavior of metal–organic frameworks for methylene blue from aqueous solution," *Microporous and mesoporous materials*, vol. 193, pp. 27–34, 2014.

[101] Z. Su *et al.*, "In-situ preparation of Cu-BTC modified with organic amines for H_2S removal under ambient conditions," *Resources Chemicals and Materials*, vol. 2, no. 2, pp. 143–150, 2023.

[102] C. Duan, F. Li, S. Luo, J. Xiao, L. Li, and H. Xi, "Facile synthesis of hierarchical porous metal-organic frameworks with enhanced catalytic activity," *Chemical Engineering Journal*, vol. 334, pp. 1477–1483, 2018.